Dissertation

submitted to the

Combined Faculties of the Natural Sciences and Mathematics

of the Ruperto-Carola-University of Heidelberg. Germany

for the degree of

Doctor of Natural Sciences

Put forward by

Philipp, Herwig

born in: Mannheim

Oral examination: 29.04.15

Coulomb Explosion Imaging studies of fundamental molecular structure

Referees: Prof. Dr. Andreas Wolf

Prof. Dr. Selim Jochim

Fundamentale Molekülstrukturen abgebildet mittels Coulomb Explosion Imaging

Bindungslängenverteilungen und Geometrien von Molekülen können mittels folieninduziertem Coulomb explosion imaging präzise bestimmt werden. In dieser Arbeit werden zwei fundamentale Fragestellungen beantwortet, die die metastabilen Zustände von H_2^- und D_2^- und auch das komplexere Kationenradikal $C_2OH_2D_2^+$ von Trans-2,3-dideuterooxiran betreffen. Die Messungen an dem durch seine starke Rotation gestreckten D_2^- wurden mit einer nicht lokalen Resonanztheorie verglichen, deren Vorhersagen in einer früheren Photofragmentationsmessung angezweifelt wurden. Unsere Messungen zeigen eine gute Übereinstimmung mit den berechneten Wellenfunktionen für Zustände mit den Rotationsquantenzahlen $J = 37$ und $J = 38$ und auch die Photofragmentationsdaten bestätigen, wenn ein bisher vernachlässigter Fragmentationskanal bei deren Analyse berücksichtigt wird. In der Studie des Trans-2,3-dideuterooxiran wurde, das erste Mal überhaupt, die Händigkeit einer enantiomerenreinen Molekülprobe durch direktes Abbilden bestimmt, wobei eine statistischen Signifikanz von 5σ erreicht wurde. Die Strukturen chiraler Moleküle zeigen unterschiedliche chemischen Eigenschaften, während außer der optischen Aktivität ihre physikalischen Eigenschaften gleich sind. Die verwendete enantiomerenreine Probe des deuterierten Oxirans war mit dem stereochemischen Referenzstandard verknüpft, wodurch die Beziehung zwischen Eigenschaften und Struktur der chiralen Moleküle, die 1894 zufällig von Fischer gewählt wurde, erstmalig in der Gasphase bestätigt werden konnte.

Coulomb Explosion Imaging studies of fundamental molecular structure

Foil-induced Coulomb explosion imaging is an accurate technique to measure bond-length distributions and geometries of molecules. Two fundamental questions are addressed in this thesis concerning metastable states of the diatomic hydrogen anions H_2^- and D_2^- and the more complex radical cation $C_2OH_2D_2^+$ of trans-2,3-dideuterooxirane. The measurements on the rotationally stretched and metastable D_2^- were preformed to investigate a discrepancy between a nonlocal resonance theory and a previous photofragmentation study. An agreement is found with theory for the calculated wave functions of states with rotational quantum numbers of $J = 37$ and $J = 38$ and also the photofragmentation data agree with theory when considering a so far neglected fragmentation channel. The study of the trans-2,3-dideuterooxirane represents the first determination of molecular handedness from an enantiopure sample by direct molecular imaging and reached a statistical significance of 5σ. The structures of chiral molecules are related to different chemical properties, while except for the optical activity their physical properties are the same. The applied enantiopure deuterated oxirane sample was chemically linked to the stereochemical reference standard, realizing the first gas-phase test of the fundamental relation between chemical properties and chiral structure that was arbitrarily chosen by Fischer in 1894.

Contents

1 Introduction

Molecules are an essential part in our environment especially since they participate in any chemical reaction. The geometrical structure of the molecules strongly influences these reactions and e.g. determines the strength of chemical bindings. Over the last decades a lot of effort has been put in the determination of molecular structures.

Most commonly molecular structures are determined via spectroscopy. Spectroscopy is the measurement and interpretation of electromagnetic radiation that is absorbed or emitted by a molecule [1]. For the interpretation of the measured data *ab initio* calculations of potential surfaces of a certain molecule, which are related to the molecular structure, are performed to identify rotational and vibrational states. Transitions between those states or the continuum are further predicted and determine the spectra. If measured and calculated spectra agree, the structure of the molecule is believed to be understood. As soon as the number of atoms in a molecule increases or the spectra associated to different structures differ only marginally [2], predictions become much more complicated. In these cases alternative methods to determine the structure are required.

Diffraction techniques also give access to molecular structures, and they are in particular used to investigate large molecules. In these measurements, a sample of molecules is bombarded by a beam of either X-ray photons, electrons or neutrons. If the de Broglie wavelength of the particles is shorter than the bond lengths of the molecule, a scattering pattern is observed. This pattern is again compared to predicted patterns to determine the molecular structure [3]. The diffraction process of a single molecule is very weak and therefore crystalline samples are required in which the periodic ordering of the molecules enhances the signal. This requirement limits the applicability of this method.

A third approach is given by imaging techniques[1] such as photofragmentation [5] or Coulomb Explosion Imaging (CEI) that is in the focus of this thesis. In contrast to the already mentioned techniques, CEI gives direct access to the molecular structure of single molecules in gas phase. It is based on the dissociation of molecules that are rapidly stripped off their binding electrons. For this purpose, the molecules can be bombarded by a laser [6] or highly charged ions [7]. Another possibility to strip off the electrons is to accelerate the molecules to typically 3% speed of light and guide them through a foil target [8] in which the molecular electrons scatter inelastically. All these methods require at least that the binding electrons are stripped off, so the positively charged ionic cores repel each other and gain asymptotic velocities, which cause them to drift apart in a geometry that is defined by the structure of the initial molecule. The molecular structure can then be investigated by, basically, taking a snapshot of the fragments.

To give a well resolved picture of the molecule, the time it takes to strip off the electrons has to be rather quick to decouple the motion of the atoms due to molecular vibrations (10^{-14} s) and rotations (10^{-12} s) from the dissociation process [8]. In this thesis foil induced CEI (FCEI) measurements are presented. An unique advantage of FCEI is the extremely short stripping time of only $\sim$ 0.1 fs. The stripping time in laser ionization measurements, which depends on the pulse length of the laser, is typically several ten fs long [9, 10].

To determine the bond lengths in a FCEI measurement, simulated fragmentation geometries of predicted molecule structures are compared to observed ones. The simulation is based on the reflection approximation [11, 12, 13]. Within the approximation, the wave function of the dissociating fragments is assumed to be a δ-function that depends on the internuclear distances in the initial molecule. In this thesis, the treatment of internal momenta caused by rotational excitation of a molecule within the reflection approximation is discussed and tested by comparing the approximation to fully quantum mechanical calculations [14].

Further, measurements of the structure of the diatomic deuterated metastable anion D_2^-

[1] Molecular imaging studies on surfaces (not in vacuum) are also performed [4].

and the radical cation ($C_2OH_2D_2^+$) of the chiral epoxide $C_2OH_2D_2$ via FCEI are presented. Both measurements exploit the distinct advantages FCEI offers: This is firstly, the small amount of molecules needed for FCEI studies. In fact, the amount of D_2^- anions produced in a typical ion source combined with their short lifetimes makes it so far impossible to investigate the structure of these anions via spectroscopy. In case of the chiral epoxide, the advantage of the direct access to the molecular structure in gas phase allows for answering one of the most fundamental questions of stereochemistry. This study was only possible since in FCEI measurements the fragment species can be identified.

In the first experimental study, the bond length distribution of D_2^- was investigated. The hydrogen anions (H_2^-, HD^-, and D_2^-) are the most simple and fundamental anions considering the number of electrons and nuclei in the molecule. As a resonant transient state, the molecular anionic states influence the cross section of reactions involving neutral hydrogen and the H^- anion [15]. These reactions are highly relevant in low temperature hydrogen plasmas and notably influence the chemistry of the early universe [16]. In 2005, the molecular hydrogen anions were unambiguously observed for the first time in the laboratory. At the same time a theory was presented which explained the lifetimes of the molecules in the μs range by strong rotational excitation ($J > 25$) [17]. Due to the strong rotation, the internuclear distance in these anions of (~ 6 a.u. in case of D_2^-) is large compared to other diatomic molecules. Recent photofragmentation measurements of D_2^- cast doubt on the theoretical predictions for the binding distance and rotational excitation of the anions [5], while at the same time FCEI measurements of H_2^- support both [18]. In this contradicting situation we performed FCEI measurements of D_2^- to test the calculated structure and rotational excitation of the anions and compared these measurements to the photofragmentation data [14].

The structure and in particular the handedness of a complex chiral molecule, consisting of seven atoms, was studied in the second measurement. Two chiral molecules with different absolute configurations, so called enantiomers, consist of the same atoms and are even mirror images of each other but show different structures. These structures are related to different chemical properties, while except for the optical activity their physical properties

are the same. In 1894, Fischer arbitrarily related a certain structure of glyceraldehyde that he labeled (L) to the sense of the optical rotation (+) [19]. This relation between property and structure was linked by chemical synthesis to various other molecules [20]. Even today, it is very challenging and often error prone to determine the absolute configuration of an enantiomer. We determined the absolute configuration of an enantiopure sample of the chiral epoxide $C_2OH_2D_2$ via FCEI. By this, we actually performed the first determination of molecular handedness from an enantiopure sample by direct molecular imaging [21, 22]. The sample was chemically linked to (+)-glyceraldehyde via reactions that did not affect the chiral center. Our FCEI measurements therefore identified also the structure of the stereochemical reference molecule. This tested for the first time in gas phase and directly without the need of any quantum mechanical calculations Fischer's assignment. In addition, the correlation between structure and property of all chiral molecules arranged in the stereochemical network and linked to (+)-glyceraldehyde was implicitly tested [23].

2 Foil induced Coulomb Explosion Imaging

2.1 Principle and realizations

Foil induced Coulomb Explosion Imaging (FCEI) is a technique to measure the structure of molecular ions [8]. The principle of FCEI is illustrated in Fig. 2.1. The Coulomb explosion process is triggered as soon as a molecule with a velocity of a few percent (typically $\sim 3\%$) of the speed of light impinges on a solid target. For FCEI measurements, the target can for example be realized by an ~ 5 nm thick carbon foil. On impact, the binding electrons of the impinging molecule are stripped off rapidly in a scattering process with the target foil electrons [24, 25, 26]. The stripping of the electrons is not necessarily complete and some may remain bound to the atoms of the initial molecule. Without the binding electrons the positively charged fragments immediately feel a Coulomb potential and repel each other. In this process, their mutual potential Coulomb energy is transferred into kinetic energy. Therefore, the fragments gain asymptotic velocities within ~ 1 μm and then start drifting apart from each other. A position and time sensitive detector is typically situated ~ 3 m behind the stripping foil and detects the fragments. The structure of the molecule is imprinted in the asymptotic velocities $\vec{v}_{ij}$, which can be determined via the measured relative detector positions $\vec{r}_{ij}$ of the fragments. For a large distance between foil and detector d and for $\vec{v}_{ij}$ being much smaller than the velocity of the initial molecule v_{mol}, the asymptotic velocities are given in a good approximation by

$$\vec{v}_{ij} \;=\; \frac{v_{\mathrm{mol}}}{d}\vec{r}_{ij}. \tag{2.1}$$

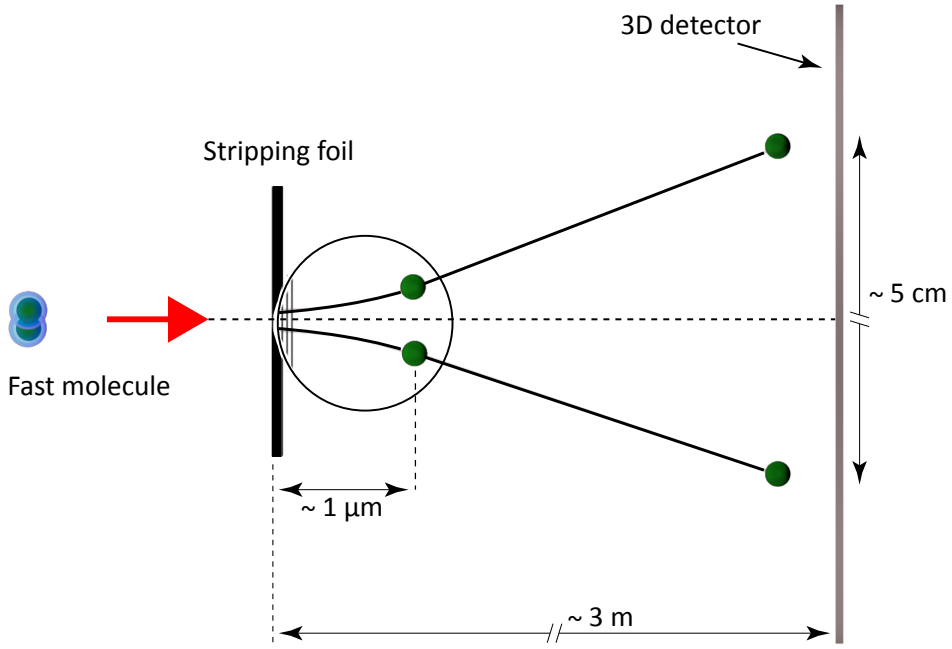

Figure 2.1: Foil induced Coulomb explosion principle. A fast molecule ($\sim$ 3% speed of light) is directed onto an ultra thin (down to $\sim$ 5 nm carbon) stripping foil. While traversing the foil, the electrons of the molecule are scattered away and the positively charged nuclei repel each other within $\sim$ 1 μm. After a few meters the fragments are detected via a position and time sensitive detector. The distance between the fragments on the detector is typically a few centimeters. The center of mass of the fragments is fixed on the prolomgation of the molecular flight path (dashed line).

As seen below, the relative velocities of the fragments are mainly given by the energy gain in the mutual Coulomb field. In comparison, the velocities of the fragments due to vibrational and rotational motion of the incident molecule give a small contribution to the asymptotic velocities which is mostly neglected, but might require attention in particular when the incident molecule is highly excited.

The stripping times in a FCEI experiment of $\sim 10^{-16}$ s are considerably quicker than the time scales of molecular vibration (10^{-14} s) and rotation (10^{-12} s) [8]. Therefore, the internuclear distance between the fragments is considered to be frozen during the stripping process. Taking the short stripping times together with typical ion velocities into account, one can see that stripping to high charge states occurs already while the

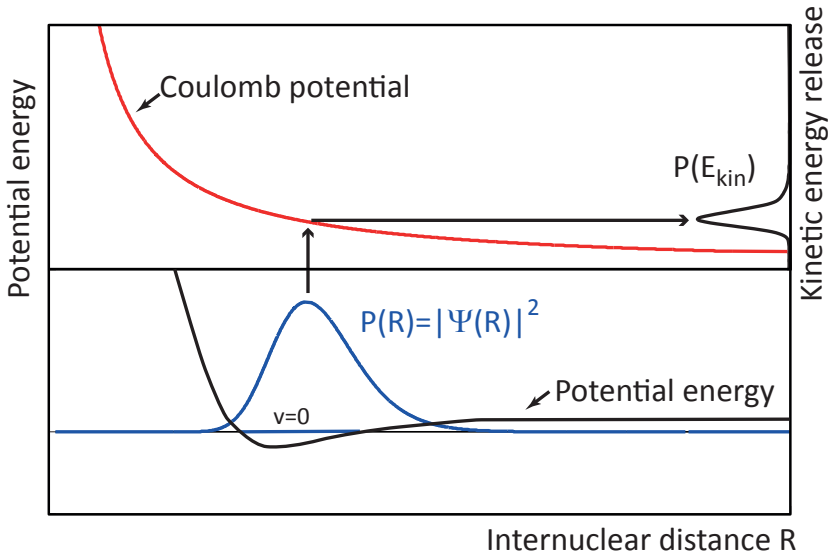

Figure 2.2: Schematic description of Coulomb explosion process according to the reflection principle for a diatomic molecule [11]. The probability distribution of the internuclear distances $P(R)$ is given by the squared wave function $\Psi(R)$. After the stripping process, the positive nuclei find themselves sitting ionized on the Coulomb potential. The Coulomb energy immediately transfers into kinetic energy E_{kin} as the fragments gain asymptotic velocities. A large internuclear distance results in a small kinetic energy release and vice versa.

molecule is traversing the foil. The estimation of stripping times for molecules that are studied in this thesis are presented in Sec. 2.2.1. Scattering and other effects that occur inside the stripping foil are discussed in Sec. 2.2.2.

A schematic view of the Coulomb explosion process for a diatomic molecule is given in Fig. 2.2. In the fast stripping process, the probability distribution of the internuclear distances $P(R)$ (blue) is reflected via the Coulomb potential (red) onto the kinetic energy release axis. Hence, $P(R)$ can in principle be reconstructed if the kinetic energy distribution $P(E_{\mathrm{kin}})$ is known.

To determine the kinetic energy release of the two fragments 1 and 2 in a FCEI measurement, one has to consider their total kinetic energy

$$E_{\mathrm{total}} = \frac{1}{2}(m_1+m_2)\vec{v}_{\mathrm{COM}}^{\,2} + \frac{1}{2}\frac{m_1 m_2}{m_1+m_2}\vec{v}_{12}^{\,2}, \tag{2.2}$$

in the center of mass frame [27]. Here, m_1 and m_2 are the masses of fragment 1 and 2,

respectively. $\vec{v}_{\mathrm{COM}}$ is the velocity of the center-of-mass and $\vec{v}_{12}$ is the relative velocity of the two fragments. The first term corresponds to the initial kinetic energy of the molecule. The second term is the kinetic energy release

$$E_{\mathrm{kin}} = \frac{1}{2}\frac{m_1 m_2}{m_1 + m_2}\vec{v}_{12}^{\,2}. \tag{2.3}$$

Therefore, E_{kin} can be determined via the observed relative velocity $\vec{v}_{12}$ (see Eqn. 2.1).

The shown distribution of the kinetic energy release contains all the information about the molecular structure of a diatomic molecule and can in principle directly compared to predicted squared wave functions. For a molecule consisting of further atoms additional considerations have to made, e.g. to get access to the angles between the atoms.Thus, in case of a three-atomic molecule Dalitz polts, which correlate the kinetic energy contribution of all individual fragments, illustrate the structure of the molecule [28]. In this thesis measurements on a molecule consisting of seven atoms of different species are presented. For such a complex polyatomic species no established approach on how to describe the molecular structure is given and thus had to be developed.

To account for the systematic effects in particular inside the foil, experiment and theory can be compared on the level of the kinetic energy release or a more complex set of detector coincidences. Hence, the Coulomb explosion process of a molecular structure given, e.g., by predicted squared wave functions or stick models is simulated via a well-established Monte-Carlo simulation [12, 13]. For this purpose, an appropriate input data set, containing a list of relative atom positions, has to be generated. The FCEI simulation simulates the Coulomb explosion of each entry individually. At first, the orientation of each molecule to the direction of the molecule beam is randomized before the molecule impinges the foil. Then, the program calculates the trajectory of each fragment through the foil stepwise. In each step, multiple scattering as well as electron loss and capture are considered by assigning each fragment a scattering angle and a charge state. Next, the simulation modifies the trajectories by assuming a point like Coulomb potential between the fragments. Also screening by the electrons of the target is taken into account. After the foil the trajectory of the fragments is further simulated and the relative detected

positions of each fragment are written into an output data set. In this step, the detector resolution, a magnetic field that guides the fragments on the detector and the geometry of the experimental setup are taken into account. To compare simulations and measurements with each other, both are analyzed in exactly the same manner and the results of the analyses are compared. If the simulations agree with the measurements - this is typically tested by a least square fit - the predicted molecular structure is confirmed.

2.2 Properties of the FCEI process

FCEI measurements require the careful consideration of several properties, which are discussed in this section. The estimation of typical stripping times is presented in Sec. 2.2.1. Effects that influence the fragment velocities in the stripping foil are discussed in Sec. 2.2.2. The effect of incompletely stripped fragments on the repelling potential is described in Sec. 2.2.3.

2.2.1 Stripping time scales

The stripping process to the final fragment charge states in FCEI measurements is remarkably fast. The stripping time of a single electron in the thin solid foil

$$\tau = \frac{1}{\sigma n_{\mathrm{Target}} v_{\mathrm{mol}}}, \tag{2.4}$$

with the electron loss cross section σ, the particle density of the target n_{Target} and the velocity of the molecule v_{mol}. For the two cases studied in the thesis, the negative hydrogen anion D_2^- (Sec. 4) and the chiral oxirane $C_2OH_2D_2^+$ (Sec. 5), electron stripping times are estimated. These stripping times can be considered as typical.

The particle density n_{Target} of a diamond like carbon foil is 10^{23} cm^{-3} [29]. Cross sections for electron capture and loss are typically measured for atoms penetrating through gas targets since even the thinnest target foils are usually thick enough to produce charge states near the equilibrium [30]. The Bohr and Lindhard model deals with density effects

of the electron loss cross section and helps to understand the relation between cross sections in gas and solid targets [30]. The model will be discussed briefly in the following. The most loosely bound electron of an ion penetrating through a target is excited in collisions with the target atoms. In a solid target these collisions happen so rapidly that, unlike in a gas target, the excitation rarely redistributes over several electrons or relaxes between single collisions. Due to the decreased binding energy of the excited electron, the electron loss cross section in the next collision is larger. As a result, the effective electron loss cross section in solid targets is larger than in gas targets of the same material. Since the stripping time decreases with a larger cross section (see Eqn. 2.4), the cross section determined in a gas target can be used to calculate an upper limit for the stripping time in a solid target.

The electron loss cross sections of ions impinging on a helium and a nitrogen gas target with a velocity of 2.6×10^8 cm/s ($\sim 1\%$ speed of light) amounts to $\sim 10^{-16}$ cm^2 depending on the nuclear charge of the ions (they are given in Fig. 5 of Ref. [31]). The cross section itself further systematically depends on the electron density in the target molecules/atoms. For our estimation, we assume a similar density in carbon as in nitrogen.

At first, the stripping times of D_2^- are estimated. D_2^- is a very large and strongly rotating molecule, which can be considered as a D^- and a D circling around each other (see Sec. 4). The electron loss cross section σ_H of neutral hydrogen is 2×10^{-16} cm^2. Neglecting isotopic effects, the binding energies of the electron in neutral H and D are the same and thus the electron loss cross sections of H and D at a given velocity are near to each other. The electron loss cross section of the most loosely bound electron of D^- is larger than σ_H.

In the measurements the anions were accelerated to 3% speed of light, which is faster than the velocity v_{mol} the cross section σ_H was measured for. For the estimation of the stripping time this has to be taken into account since the cross section depends on the target velocity. According to the Bohr energy loss formula, it holds that $\sigma(v_{mol}) \propto 1/v_{mol}^2$ or $\sigma(v_{mol}) \propto 1/v_{mol}$ for $Z_{Atom} \geq Z_{Target}$ or $Z_{Atom} < Z_{Target}^{1/3}$, respectively [32]. Here, Z_{Atom} is the atomic number of the atom and Z_{Target} is the atomic number of the target. Between 1% and 3% of the speed of light these relations are not necessarily true: In Fig. 3 of Ref. [31]

the electron loss cross sections of He and Ni ions penetrating a helium target increase for higher velocities (according to the Bohr formula they should decrease). Therefore, the cross sections for 3% speed of light cannot be extrapolated via the Bohr formula. In addition, the velocity dependence differs for various targets (see Graph IV in Ref. [33]). As a consequence, we cannot transfer the measured dependence in helium given in Ref. [31] to our case. Hence, we cannot account for the velocity dependence of the cross section and the calculated stripping time

$$\tau_{\mathrm{D}}^{+} \sim \frac{1}{10^{23}\ \mathrm{cm}^{-3} \cdot 2 \times 10^{-16}\ \mathrm{cm}^{2} \cdot 9 \times 10^{8}\ \mathrm{cm/s}} = 0.06\ \mathrm{fs} \tag{2.5}$$

of the electron in D has to be considered as an approximation for the stripping time. The most loosely bound electron in D^- will be stripped off quicker.

Similarly, stripping times are also calculated for $C_2OH_2D_2^+$. The oxirane radical cation was accelerated to 1% speed of light and the cross sections of Ref. [31] for the atomic constituents are given for the correct velocities. Therefore, the estimated stripping times are "hard" upper limits. The stripping times for the electron in H and D is now $\tau_{\mathrm{H/D}}^{+} < 0.17$ fs since the molecule is slower. For the loss of the first electron in carbon and oxygen the electron loss cross section $\sigma_{\mathrm{O/C}}^{+}$ is 5×10^{-16} cm^2 and for the loss of the second electron $\sigma_{\mathrm{O/C}}^{2+}$ is 2×10^{-16} cm^2. Further charge states are not considered in the analysis of the chiral oxirane measurements. The corresponding stripping times $\tau_{\mathrm{O/C}}^{+} < 0.08$ fs and $\tau_{\mathrm{O/C}}^{2+} < 0.17$ fs. These stripping times are ~ 100 times quicker than the typical stripping times of laser induced CEI.

2.2.2 Foil effects

The stripping of the electrons takes place while the molecular fragments traverses the stripping foil. In the foil, several effects influence the trajectories. Fragments passing through the foil undergo not only electron stripping but also electron capture [12]. Both processes compete to yield the effective fragment charge states and change the Coulomb potential between the fragments. The probability of the charge state in which a fragment

finally emerges the foil depends on the foil thickness and the velocity of the molecule. The statistical uncertainty of the stripping process leads to a broadening of the measured relative velocity (kinetic energy release) distributions. Additionally, multiple scattering of the fragments by small angles occurs. This effect has the strongest impact on the asymptotic velocities and adds to the measured relative velocity (kinetic energy release) distributions a high energy tail due to additional "energy" that is "pumped" into the system [34]. The scattering is minimized by choosing a target foil material with a low nuclear charge Z [12, 13]. Further, while the positively charged ions traverse the foil, they disturb the electron density and by this induce an electronic charge density field [24, 35, 32]. This field extends in an approximately conical shape behind the particle with an exponentially decaying and oscillating intensity [36]. The electric field results in a stopping force and slows down the ion itself. It also causes the so called wake effect since the increased electron density related to one ion attracts other nearby ions. Using a thin foil and a fast molecule minimizes these effects, since both decrease the time the ions spend inside the foil and the Coulomb explosion therefore happens mostly behind the foil where no perturbating fields exist [29, 37, 38].

2.2.3 Effects of incomplete stripping

According to the Bohr criterion, an electron will be stripped in a collision if its orbital velocity is less than the projectile velocity [32]. The orbital velocity of a bound electron in the shell n of an atom with the nuclear charge Z is Z/n a.u.[1]. To reach collision velocities fast enough to trigger the stripping process, particle accelerators are needed that accelerate the molecular ions. In this process, however, the velocity of the molecular ion is limited by its mass for the following technical reasons (see also Fig. 2.3).

A first upper limit is determined by the accelerator used to accelerate the ions. One accelerator available for the present experiments, a single ended Van-de-Graaff accelerator, reaches energies of up to ~ 3 MeV for singly charged ions. This energy sets the first upper

[1] In this thesis atomic units are used, which are based on the properties of the hydrogen atom. The elementary charge e, the electron rest mass m_e and the reduced plank constant $\hbar$ are all defined to equal unity [39]. The Bohr radius $a_0 = 1$ a.u. and the speed of light c = 137 a.u..

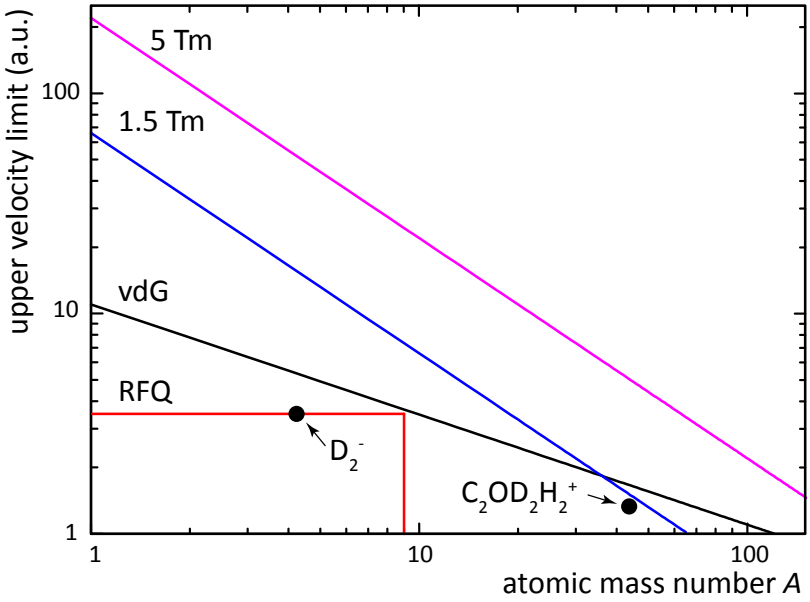

Figure 2.3: Upper limit of molecular velocity due to technical limitations as a function of the atomic mass number A in double logarithmic scale. The velocity of the molecular ions is limited by the energy of the accelerator. The maximum velocity of the single ended Van-de-Graff (black) and the linear radio frequency accelerator (red) situated at the MPIK is shown. A second limitation for the velocity is determined by the rigidity of mass selecting and guiding magnets. The maximum velocity for a magnet with a rigidity of 1.5 Tm (blue) and 5 Tm (magenta) is depicted. The working points of the presented experiments are depicted.

limit for the velocity molecule to $\sim\ 11/\sqrt{A}$ a.u., where A is the atomic mass number. A second upper limit for the velocity is determined by the mass selection or guiding dipole magnets of the accelerated molecular ion before the FCEI measurements. The rigidity

$$R \quad = \quad B \cdot R_c = \frac{p}{q} \tag{2.6}$$

of the magnet with the magnetic field B, the orbit radius R_c, the charge state q of the molecule and its momentum p. The rigidity R in the present case is limited to 1.5 Tm through the availible mass selecting magnet, which leads to a velocity limitation for singly charged molecules of $66/A$ a.u.. In principle, the molecules can be accelerated further in a storage ring or a chain of subsequent storage rings. In these rings the velocity is limited by the rigidity of the ring that may reach higher values at other facilities.

Especially for heavy molecules with a large A, the velocities that can be achieved are not necessarily fast enough to strip off all bound electrons and so some electrons remain bound to the nuclei. The remaining electrons shape the dissociation potential at small distances between the fragments. Since they shield only partially the positively charged nuclei, the actual repelling potential is here steeper than a point-like Coulomb potential with the same charge [40]. In FCEI simulations, using such a point-like Coulomb potential between the fragments, relative velocities can be underestimated and a comparison with such simulations may become unsuitable for testing bond length distributions. On the other hand, bond-angle distributions are expected to be much less influenced by the exact shape of the potential [29, 40].

2.3 Experimental setup at TSR

The setup used for the presented studies on the deuterated hydrogen anion D_2^- and the chiral oxirane cation $C_2OH_2D_2^+$ via FCEI is located at the accelerator facility of the Max Planck Institute for Nuclear Physics (MPIK). A schematic overview of the accelerator building that houses the experimental setup is given in Fig. 2.4. In the D_2^- measurements, a linear radio-frequency accelerator was applied to produce the fast anion beam. This accelerator can be used for positively and negatively charged molecules with a mass up to 9 u, only the molecules are accelerated to a fixed velocity of 0.5 MeV per nucleon. The anions were produced in an off axis duoplasmatron ion source. The source was installed especially for this measurement, since in previous imaging experiments, performed by Lammich *et al.* [5], this source type was shown to produce D_2^- in sufficient amounts. The $C_2OH_2D_2^+$ ions were accelerated by a single ended Van-de-Graff accelerator. The accelerator is commonly used for positively charged molecules that can be accelerated to a kinetic energy of up to 2.5 MeV if they are singly charged. The accelerator is equipped with a cold cathode Penning ion source in which the $C_2OH_2D_2^+$ molecule ions were produced. In both measurements the first bending magnet behind the accelerator was utilized to mass select the ion beam. Several further bending magnets guided the charged molecules

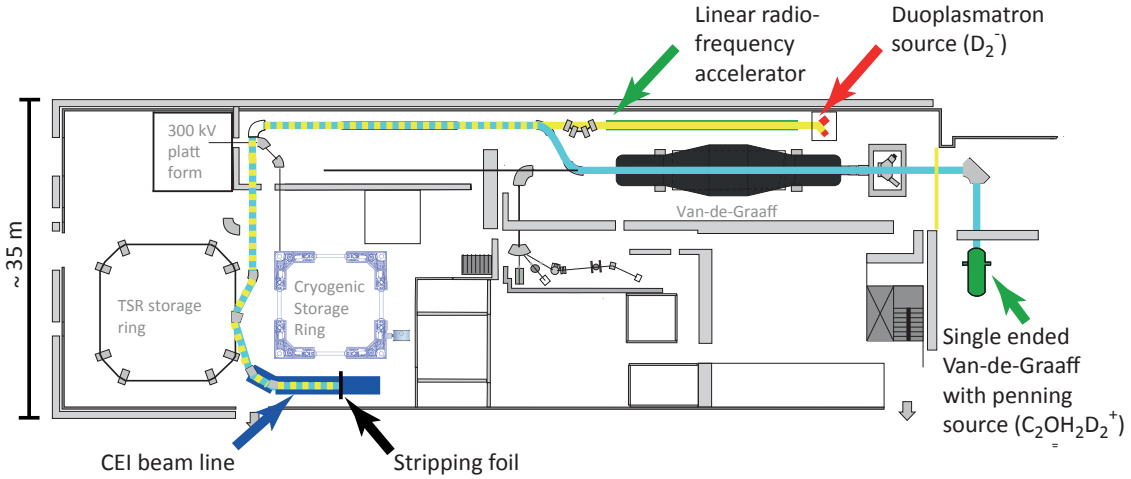

Figure 2.4: Schematic of the accelerator building at MPIK. For the measurements presented in this theses, a duoplasmatron ion source (red) in combination with a linear radio frequency accelerator (green) and a cold cathode Penning ion source in combination with a single ended Van-de-Graff accelerator (green) were used. The cold cathode Penning ion source is located in the accelerator. The accelerated molecule ions were guided via several dipole magnets into the FCEI beamline (blue) where the stripping foil (black) is located. The flight paths from each ion source to the stripping foil are highlighted by the turquoise ($\sim$ 130 m) and yellow line ($\sim$ 100 m). The apparatuses labeled in small fonts were not used in the experiments discussed in this thesis.

into the FCEI beamline.

For FCEI studies at these accelerators a dedicated beamline was set up in earlier work [41]. A schematic of the FCEI beamline is given in Fig. 2.5. A bending magnet guides the ions through two collimators to define the beam profile. In both collimators, apertures with diameters of 5 mm, 2.5 mm, 1.5 mm, 1 mm or 0.5 mm, respectively, can be inserted into the ion beam. The collimators are $\sim$ 3 m distant from each other. Directly behind the collimator 2 and close to the FCEI foil 1 (see Fig. 2.5) an auxiliary magnetic field is situated. When activated, this magnetic field deflects charged molecules. This makes it possible to selectively study the Coulomb explosion of those neutral molecules which formed on the straight line between the last upstream bending magnet the FCEI target. The ions penetrate either a diamond like carbon (DLC) [42] foil 1 with a thickness of 1.2 μg/cm^2 or DLC foil 2 with a thickness of 0.8 μg/cm^2. In the foil the Coulomb explosion process is triggered. After the Coulomb repulsion, the fragments are guided through a

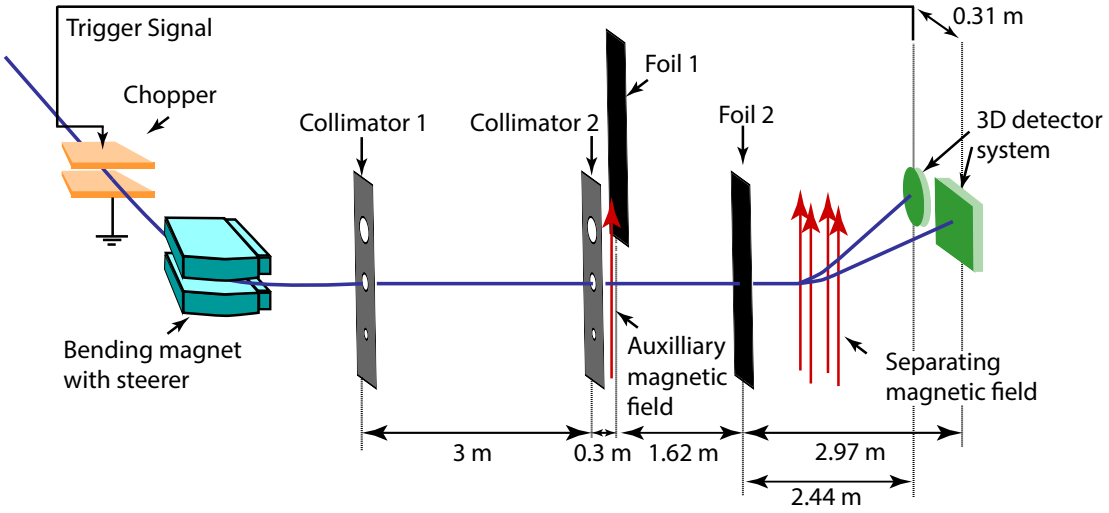

Figure 2.5: Coulomb Explosion Imaging beam line. Behind the chopper, the last bending magnet guides the charged molecules through two collimators to define the beam and direct it onto one of the two DLC foils. When the molecules imping on the foil, the Coulomb explosion process is triggered. In the shown sketch stripping foil 2 is in the beam path. Stripping foil 1 can also be put in the beam path and at the same time stripping foil 2 can be removed. After their repulsion, the fragments are guided through a magnetic field that separates them by their charge-to-mass ratio and guides them onto the detector system, which consists of a round and a rectangular detector. An auxiliary magnetic field can be activated to measure solely the Coulomb explosion of neutral fragments, which formed on the straight beam path after the last bending magnet. The distances between the beam line components are depicted. The distance between the middle of the round and the rectangular detector projected in the plane defined by the rectangular detector of 31.4 cm is not in scale.

further magnetic dipole field which steers them onto specific detector positions by small deflections depending on their charge-to-mass ratios.

Both detectors are capable of detecting multiple hits in coincidence. Each consists of a microchannel-plate (MCP) and a phosphor screen imaged by a CCD camera (compare Fig.5 of Ref. [41]). The round MCP has an active area of $\sim$ 100 mm diameter, and the rectangular detector is 93 mm broad and 76 mm high. In front of the MCPs a $\sim$ 1.5 μm thick aluminized mylar foil, coated with a CsI layer, is installed in the original detector layout to improve the detection efficiency to almost 100% [41]. Ions impinging on this foil create electrons that are accelerated towards the MCP via a potential. Electrons impinging on the MCP start an electron avalanche that creates up to 10^8 well localized

electrons per ion. These electrons are further accelerated towards the phosphor screen where they create a visible light spot on incident. Two 25 Hz CCD cameras monitor the phosphor screens. Their video signal is digitized by Frame Threshold Suppressors that also notify a VME computer to read out the data. The transverse ion positions determined via the cameras have a resolution of ~ 100 μm.

Both detectors are equipped with vertical parallel anode wires that are situated underneath the phosphor and etched on top of a transparent kapton foil. The wires are separated by 1 mm in case of the round detector and 0.5 mm in case of the rectangular detector. An electron cloud impinging on a phosphor screen triggers signals on adjacent wires. The signal of each wire is amplified separately before it is fed into a constant fraction discriminator (CFD). The CFD starts the accumulation of charge into a charge analog to digital converter (QADC). The first incident fragment on the round detector also triggers a common time delayed stop signal, which stops the accumulation of charge in all QADC's at the same time to prevent them from getting saturated before they are read by the data acquisition system (DAQ). The amount of charge that is fed into the QADC's per time unit can be adjusted so their dynamic range meets the demands of the measurements. The accumulated charge translates into a longitudinal time with an accuracy of ~ 200 ps. The longitudinal time differences between fragments correspond to their relative longitudinal positions. In an offline analysis the transverse and longitudinal ion positions are correlated.

At the entrance of the beam line an electrostatic chopper is situated. It is immediately charged when the first ion impact on the round detector is recorded. Thereby, further charged molecules are strongly deflected and prevented from entering the FCEI beamline. Since the ion flux is additionally kept low, in the order of ~ 1 kHz, multi-ion events on the 25Hz CCD cameras are strongly suppressed. As soon as the event was read by the DAQ, the chopper is uncharged again.

Due to the heavy mass of the $C_2OH_2D_2^+$ ions, the molecules could not be accelerated fast enough for fragments to penetrate the original 1.5 μm thick charge multiplication foil. Consequently, the foils had to be replaced by extremely thin mylar foils of 0.5 μm

(Goodfellow). These foils were aluminum coated in a special procedure but they were not additionally coated with a CsI layer since they would not have withstood this procedure. The electron yield of these new foils is therefore lower and the detection efficiency dropped. The new foils were also used in the D_2^- measurement.

2.4 Previous molecular physics studies

Having discuss the FCEI principle and the realization of the experimental setup, it is interesting to briefly show some prominent examples of previous molecular studies using the FCEI method. The incomplete overview includes measurements on $C_2H_2^+$ (Sec. 2.4.1), HD^+ and H_3^+ (Sec. 2.4.2) as well as DCO^+ and DOC^+ (Sec. 2.4.3). Their impact on the measurements presented in this thesis is discussed.

2.4.1 $C_2H_2^+$

FCEI was pioneered in the 70's at the Weizmann Institute in Israel [43, 35, 44]. Zajfman *et al.* reported the measurement of the structure of $C_2H_2^+$ via FCEI in 1991 [45]. The experiment was carried out at the Argonne National Laboratory. The acetylene cation $C_2H_2^+$ was produced via electron impact on acetylene, and it was expected that the cation is mainly produced in the vibrational ground state. To understand their measurements, the authors simulated the Coulomb explosion process of assumed molecular structures and fitted the results to the measurements. The simulation took already foil effects into account. The determined structure of the molecule, the one that resulted in the best fit, was in agreement with previous theoretical and experimental studies of a *linear* molecule. They concluded that it is possible to measure molecular structures using the FCEI technique and even see "the extent of nuclear motions". The approach to compare theory and measurement is still used today.

2.4.2 HD^+ and H_3^+

In 1997, the FCEI setup discussed in the previous section was installed at the Max Planck Institute for Nuclear Physics (MPIK) in Heidelberg as a complement to the storage ring TSR [46, 47, 41]. As a first benchmark experiment for this setup, imaging of the molecular hydrogen ion HD^+ was performed [41, 29, 48]. This molecule is theoretically very well understood and the simplest ion which can cool radiatively in the storage ring. The ions were produced in a standard Penning source source and accelerated to 2 MeV, using a Van-de-Graff accelerator, before they were injected into the TSR. A small part of the stored ions was continuously extracted from the TSR and fed into the FCEI beam line using a "slow extraction" mode. The results of the time resolved measurements showed good agreement directly with calculated vibrational wave functions and also vibrational cooling was observed [41, 29, 48]. Later, the results were used to derive electron-induced vibrational cooling rates of stored HD^+ ions.

Another system of great interest is the triatomic hydrogen molecular ion H_3^+, which has been studied intensely at the MPIK via FCEI [49, 50] and dissociative recombination measurements [51, 52]. H_3^+ is not only the simplest polyatomic ion, it also plays a dominant role in astrochemical models [53, 54]. For the measurements the ions were produced in a gas discharge source. After the molecules were accelerated to 1.43 MeV, they were injected into the storage ring TSR. The time resolved FCEI measurements showed that the molecular ions are produced with very high ro-vibrational excitation in commonly used ion sources. They were proven to relax to the vibrational ground state within 2 s by spontaneous radiative transitions. The measurements also indicated that a large fraction of the molecules remained highly rotationally excited even after extended storage in a 300 K environment. The strong excitation was also observed in the dissociative recombination measurements, which were performed under similar conditions. Previous rate coefficient measurements for the dissociative recombination of H_3^+ showed a discrepancy of a factor of 10 [55]. The results of this measurement led to the conclusion that the discrepancy is influenced by the rotational excitation of the H_3^+ and therefore related to ion source conditions.

Both measurements (amongst others) showed how accurately the wave functions of individual states of hydrogen molecules can be investigated by the FCEI method. The measurements discussed in this thesis benefit a lot from the developments during these experiments, concerning the improvement of the experimental setup and the treatment of measured data.

2.4.3 DCO^+ and DOC^+

Another FCEI experiment carried out at the MPIK was performed with DCO^+ and its isomer DOC^+ in 2002 [29, 56]. HCO^+ and DCO^+ are highly abundant in interstellar space and, e.g., the proton-deuteron isotope ratio in interstellar clouds can be determined via spectroscopy of these molecules [57]. The molecules were produced by the fragmentation of methoxide anions CD_3O^- in the stripping section of the MPIK tandem accelerator and mass analyzed, so that the produced cationic beam could contain both isomeric species DCO^+ and DOC^+. After they were accelerated to 3.16 MeV, the ions were stored in the TSR for up to 12 s where they cooled down to room temperature. The extracted ions were guided into the FCEI beamline and fragmented via the stripping foil. Then, the fragments were further guided through the magnetic field to separate them by their charge-to-mass ratio and by this fragment species C^{2+}, O^{2+} and D^+ could be separately identified. By inspecting the angles of the detected fragments, a relative abundance of the isomer DOC^+ in the ion beam stored in the TSR was determined to a value of $(10 \pm 1)\%$. An isomerziation between low lying vibrational levels of the isomers when stored in the TSR did not occur. Predicted bond length distributions did not agree with the measurement, and it was concluded that this was due to the incomplete stripping of the fragments, which leads to complex dissociation potentials that are not incorporated in the FCEI simulation (see Sec.2.2.3).

These measurements, as a study on a polyatomic molecule containing the heavier atoms of O and C, mark certainly a cornerstone towards the $C_2OH_2D_2^+$ measurements discussed in this thesis, in particular since they also showed that binding angles representing the molecular confirmation can be determined although the fragments are incompletely stripped.

3 Validity of the reflection approximation for heavily rotating molecules

The imaging of molecular structures via FCEI requires the simulation of kinetic energy release distributions from predicted molecular structures since measurement and theory are usually compared on this level. In the simulation the FCEI process is considered as a reflection of the squared wave-function via the Coulomb potential onto the kinetic energy axis as described in Sec. 2.1. By doing so, the initial momenta of the molecule atoms due to vibrations and rotations are neglected. This neglect within the well established reflection approximation [11, 58, 59] is justified as long as the Coulomb energy is much larger than the rotational or vibrational energy and was generally assumed in earlier work. In this section, we present the treatment of strong rotational excitation of a diatomic molecule within the reflection approximation and test it by comparing the kinetic energy release calculated within the reflection approximation to fully quantum mechanical calculations of the kinetic energy release. This discussion is mainly motivated by the study of the structure of the very strongly rotational excited D_2^- anion presented in Sec. 4. Part of this section is already published in [18, 14].

3.1 Quantum mechanics and reflection approximation

In quantum mechanics the overall wave function Ψ of a molecular state is given by $\Psi = \Psi_e \Psi_n \Psi_s$. Here, Ψ_e, Ψ_v, and Ψ_s are the electronic, the nuclear and the spin wave functions, respectively. According to the the Franck-Condon principle, the intensity of a vibronic

transition is (neglecting spin) given by

$$I \;=\; \left| \int \Psi_n'^{*} \Psi_n \left[\int \Psi_e'^{*} \mu_e \Psi_e d\tau_e \right] d\tau_n \right|^2 . \tag{3.1}$$

with μ_e being the dipole operator, Ψ_i' and Ψ_i being the wave function of the final and initial state, while τ_e and τ_n indicate the integral over the full range of the coordinates of the nuclear and electronic wave function, respectively [60, 61]. The integral over the nuclear wave function leads to the Franck-Condon factor.

In FCEI experiments, the electron stripping is very rapid and the molecule can be considered as frozen during this process. The transition is forced by removing the electrons of a molecule via stripping and therefore the transition probability is no longer dependent on the electronic wave functions. For a diatomic molecule, in analogy to Eqn. 3.1, one can calculate the kinetic energy release distribution via the Franck-Condon factor as

$$P_{J,v}(E)dE \;=\; \left| \int_0^\infty \Psi_{J,E}^{*,\mathrm{C}}(\widetilde{R}) \Psi_{J,v}(\widetilde{R}) d\widetilde{R} \right|^2 dE \,. \tag{3.2}$$

Here, $\Psi_{J,v}(R)$ is the nuclear wave function with the internuclear distance R, the rotational quantum number J and the vibrational quantum number v. The continuum wave function $\Psi_{J,E}^{\mathrm{C}}(R)$ of the two dissociating fragments is the solution of the one-dimensional Schrödinger equation

$$\left\{ \frac{d^2}{dR^2} + \frac{2\mu}{\hbar^2} \left[E - V_J^C(R) \right] \right\} \Psi_{J,E}^{\mathrm{C}}(R) \;=\; 0. \tag{3.3}$$

The effective radial potential is $V_J^C(R) = V^C(R) + V_J(R)$, with the Coulomb energy $V^C(R) = e^2/R$ and the rotational energy $V_J(R) = \hbar^2 J(J+1)/(2\mu R^2)$. For $R \to \infty$ the potential $V_J^C(R) \to 0$ and the asymptotic solution for the Schrödinger equation is

$$\lim_{R\to\infty} \Psi_{J,E}^{\mathrm{C}}(R) \;\to\; a \sin\left[k(E)R + \varphi\right] \tag{3.4}$$

with $k(E) = \sqrt{2\mu E}/\hbar$, the normalization factor $a = \sqrt{2\mu/(\pi\hbar^2 k)}$ and a phase φ. The normalization factor ensures that the wave function $\Psi_{J,E}^{\mathrm{C}}(R)$ is energy-normalized [62].

In Eqn. 3.2 two assumptions were made: Effects of the target foil on the nuclear wave functions were neglected and it was assumed that the rotational angular momentum of the molecule does not change in the stripping process. Within the reflection approximation Eqn. 3.2 is simplified be approximating the continuum wave function as

$$\Psi^{\mathrm{C}}_{J,R(E)}(\widetilde{R}) \;=\; \delta(\widetilde{R} - R(E))\,. \tag{3.5}$$

Here, δ is Dirac's δ-function and $R(E)$ is calculated via $V_J^C(R)$ as

$$R(E) \;=\; \frac{e^2}{2E}\left(1 + \sqrt{1 + 4E\frac{h^2 J(J+1)}{2\mu e^4}}\right)\,. \tag{3.6}$$

At this point, the rotational excitation energy is considered as an additional contribution to the Coulomb potential [18]. In order to change to energy normalization the δ-function has to be renormalized [63, 62] and one must in Eqn. 3.2 use

$$\Psi^{\mathrm{C}}_{J,E}(\widetilde{R}) \;=\; \sqrt{\left|\frac{dR(E)}{dE}\right|}\,\delta(\widetilde{R} - R(E))\,. \tag{3.7}$$

With the continuum wave function, given in Eqn. 3.7, Eqn. 3.2 simplifies to

$$P_{J,v}(E)\,dE \;=\; |\Psi_{J,v}(R(E))|^2 \left|\frac{dR}{dE}\right| dE \tag{3.8}$$

with

$$\left|\frac{dR}{dE}\right| \;=\; \frac{R^3}{e^2 R + \frac{\hbar^2 J(J+1)}{2\mu}}\,. \tag{3.9}$$

3.2 Comparison of kinetic energy distributions

To test the validity of the reflection approximation for strongly rotationally excited molecules, we compared calculations of the kinetic energy release distributions $P_{J,v}(E)$ within the approximation to fully quantum mechanical calculations. The kinetic energy release distri-

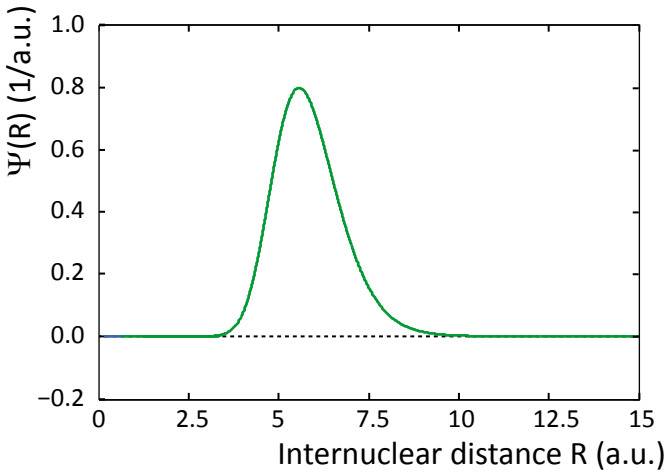

Figure 3.1: Wave function of the deuterated hydrogen anion D_2^- for the $(J = 37, v = 0)$ state as predicted by Čížek *et al.* [64]. Due to the strong rotational excitation the molecule is largely stretched compared to other diatomic molecules.

butions were calculated via Eqn. 3.2 for the quantum mechanics case and via Eqn. 3.8 for the reflection approximation. In the calculations we used the D_2^- wave function $\Psi_{37,0}(R)$ calculated by Čížek *et al.* [64] (see Sec 4.1.2) with $J = 37$ as a starting point for the molecular wave function $\Psi_{J,v}(\widetilde{R})$. The wave function is depicted in Fig. 3.1. The continuum wave functions of the two ionized deuterium nuclei $\Psi^{\mathrm{C}}_{37,E}(\widetilde{R})$ for $J = 37$ are shown in Fig. 3.2 for different kinetic energies E. They were calculated by solving the Schrödinger equation (Eqn. 3.3) numerically via the Numerov method [65, 66].

The kinetic energy release distributions are compared in Fig. 3.3(a). They agree very well with each other and the maximum of the quantum mechanically calculated distribution is only slightly smaller (see inset). With this accuracy, we assume the approximation to be justified for the interpretation of the measurements on D_2^- presented in Sec. 4.

To test the limits of the approximation we varied the wave function of the molecule $\Psi_{37,0}(R)$ in such a way that it mimics a larger molecule with an internuclear distance of 10.5 a.u.. Additionally, we varied the rotational excitation J of the dissociated fragments. By doing so we artificially reduced the availible Coulomb energy and added more rotational energy into the system.

At first the same molecular wave function $\Psi_{37,0}(R)$ was used, but the rotational ex-

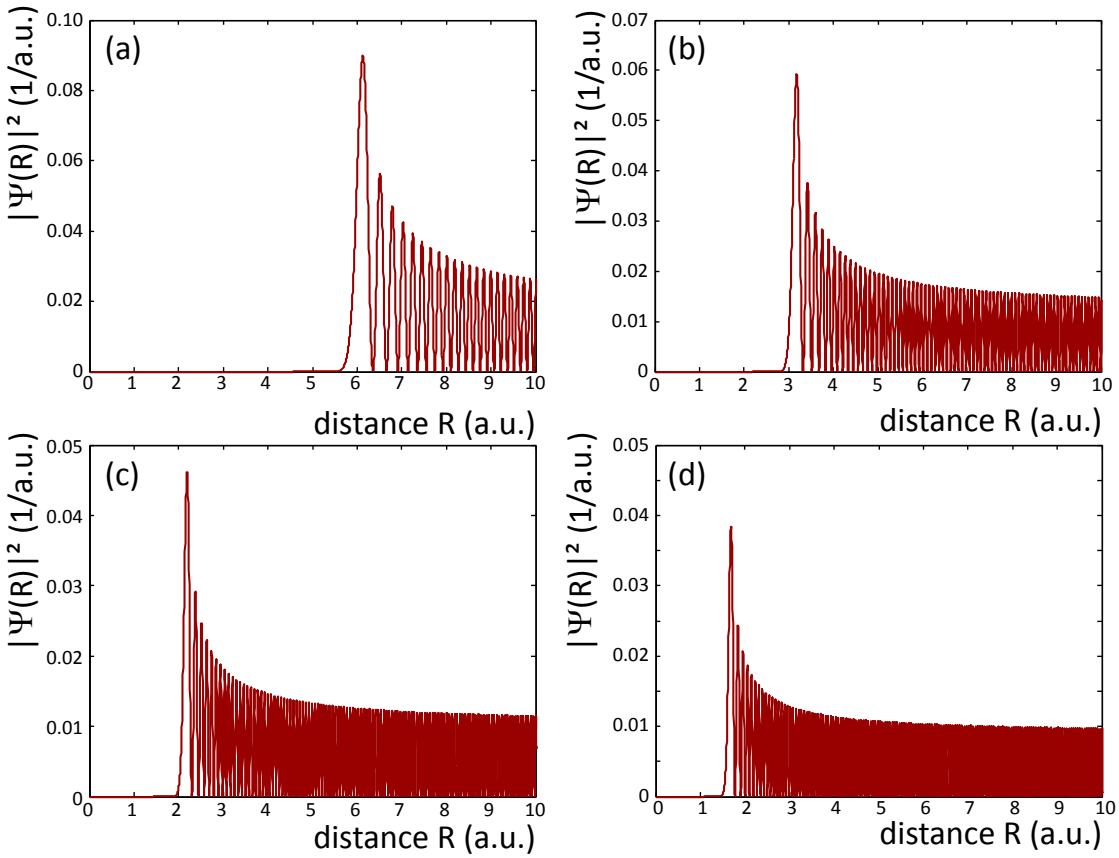

Figure 3.2: Squared wave functions of two separated D^+ for a kinetic energy of (a) 2.5 eV, (b) 5 eV , (c) 7.5 eV and (d) 10 eV. The assumed rotational state of the deuteriums was $J = 37$.

citation J of the dissociating fragments in Eqs. 3.3, 3.6 and 3.9 was increased to 120. As shown in Fig. 3.3(b) both distributions agree still very well with each other, while the peaks of both distributions agree now even better. For further tests, the wave function $\Psi_{37,0}(R)$ (see Fig. 3.1) was shifted by 5 a.u. to larger internuclear distances, setting $\Psi_{J,v}(\widetilde{R}) = \Psi_{37,0}(R-5)$, while $J = 37$ was assumed again. The corresponding kinetic energy release distributions are compared in Fig. 3.3(c). The peak value of the quantum mechanically calculated kinetic energy release distribution is now slightly smaller, while the whole distribution is shifted to higher values by a barely visible amount. In Fig. 3.3(d) the distributions are compared for the same shifted wave function and $J = 120$. The shift is still present but did not increase. The peaks of the distributions agree again better.

Thus we find, very strong excitation up to $J = 120$ does not limit the validity of the

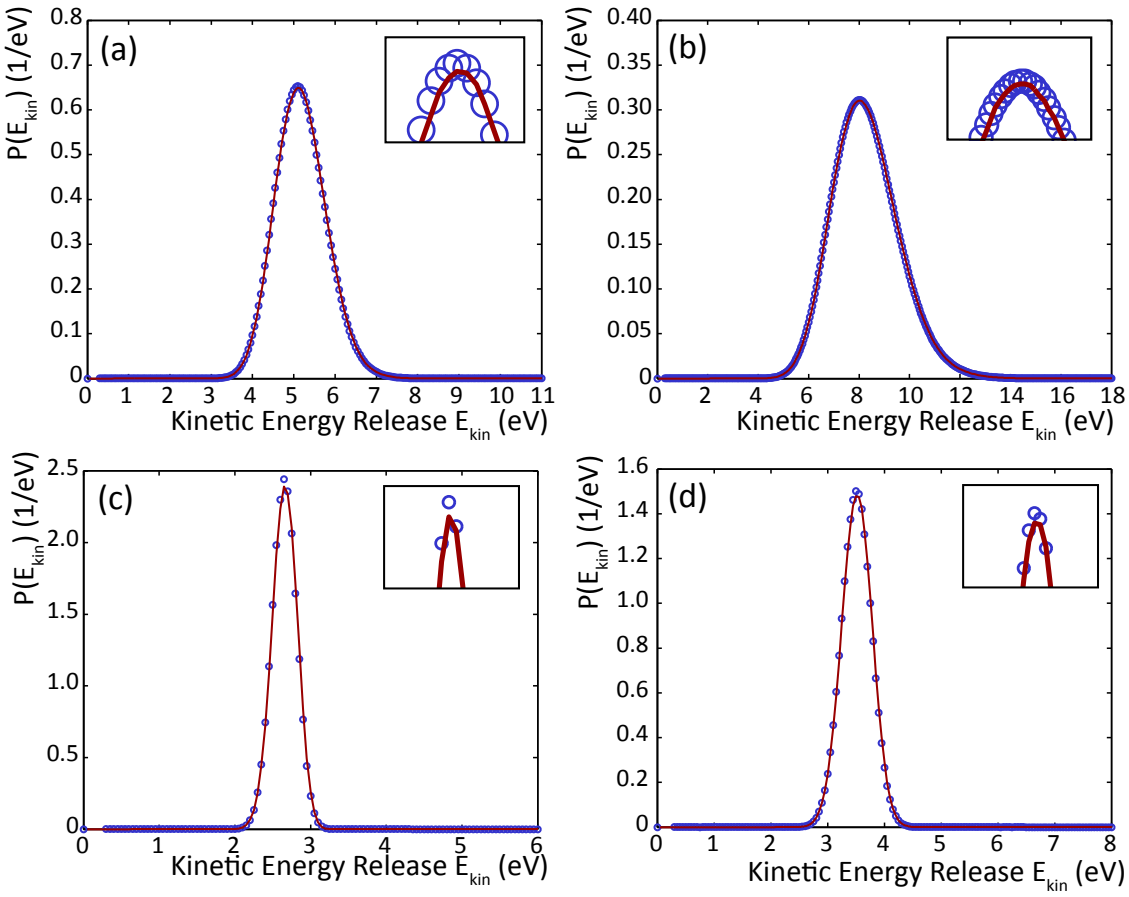

Figure 3.3: Justification of reflection approximation for highly rotational excited molecules. Calculations of the kinetic energy release within the semi-classical reflection approximation (circles) and fully quantum mechanical (lines) are compared. The calculations were performed for (a) $\Psi_{J,v}(\widetilde{R}) = \Psi_{37,0}(R)$ and $J = 37$, (b) $\Psi_{J,v}(\widetilde{R}) = \Psi_{37,0}(R)$ and $J = 120$, (c) $\Psi_{J,v}(\widetilde{R}) = \Psi_{37,0}(R-5)$ and $J = 37$ and (d) $\Psi_{J,v}(\widetilde{R}) = \Psi_{37,0}(R-5)$ and $J = 120$. The insets show a zoom of the distribution maximums.

reflection approximation. On the contrary, since the first peak of the wave function of the dissociating fragments becomes more pronounced the stronger the rotational excitation is (compare Fig. 3.2(d) and Fig. 3.4) the approximation of a δ-function for the dissociating fragments seems to be even better. Also for molecules up to 10.5 a.u., the deviations are still small and, within the uncertainties of the FCEI measurements, do not hinder the interpretation of the experiment. For a large initial molecule the approximation is not as good as for a small molecule, although it is still very well justified. The reason might be found in Fig. 3.2 where the wave functions of the dissociating fragments are shown

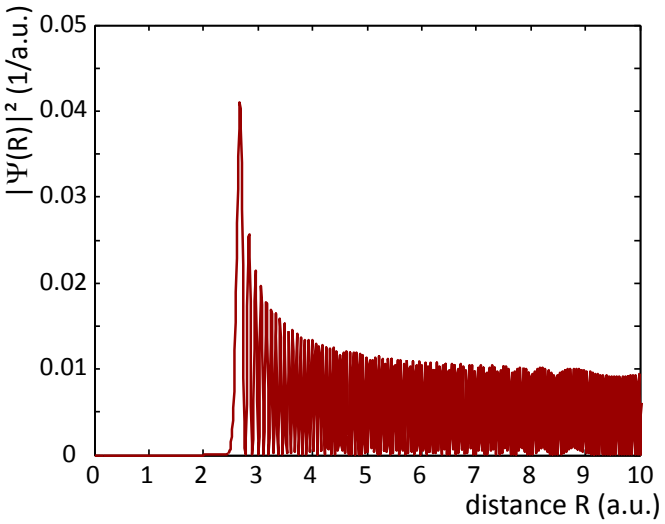

Figure 3.4: Squared wave functions of two separated D^+ for $J = 120$ and a kinetic energy of 10 eV. When compared to Fig. 3.2(d) the first peak of the wave function becomes slightly higher.

for different kinetic energies. For higher kinetic energy releases, and therefore a smaller molecule, the first peak of the wave function gets narrower and again the assumption of a δ-function seems to be more justified.

The treatment of rotation within the reflection approximation as an additional contribution of the rotational energy to the Coulomb potential is therefore valid, and the accuracy of the calculations actually improves the stronger the system is rotationally excited.

4 Structure of rotationally stabilized hydrogen anions

The atoms and molecules of hydrogen are of widest interest and discussed in probably every textbook that introduces into quantum mechanics. What makes these systems so informative and fundamental is that fact that the number of nuclei and electrons involved is small and therefore calculations can sometimes be performed even without the need of including approximations. The calculations provide experimental physicists with exact predictions of states and in combination with highly accurate measurements, quantum mechanical effects can be understood and tested on a very basic level.

The hydrogen molecule H_2 can ionize to H_2^+, while a molecular bond break of H_2 leads to two H atoms, or, with an ionized H atom, protonation of the neutral molecule results into H_3^+. These systems and reactions are today known and understood to much detail. The scenery changes when an electron is added into the neutral system and thereby H_2^- is formed. Indeed, the negative hydrogen molecular ions (H_2^-, D_2^- and HD^-) were observed unambiguously and theoretically understood recently. But still today, the community is confronted with puzzling results of measurements that cast doubt on the predicted physics of these metastable anions.

In the following, foil induced Coulomb Explosion Imaging (FCEI) measurements on D_2^- are presented to investigate these results. An historical outline about previous studies as well as the physics of the hydrogen anions is presented in Sec. 4.1. In Sec. 4.2 the puzzling previous results, which were already brought up and actually motivated our experiment, are discussed in detail. Our measurements and results are discussed in Sec. 4.3. The results are already published in [14].

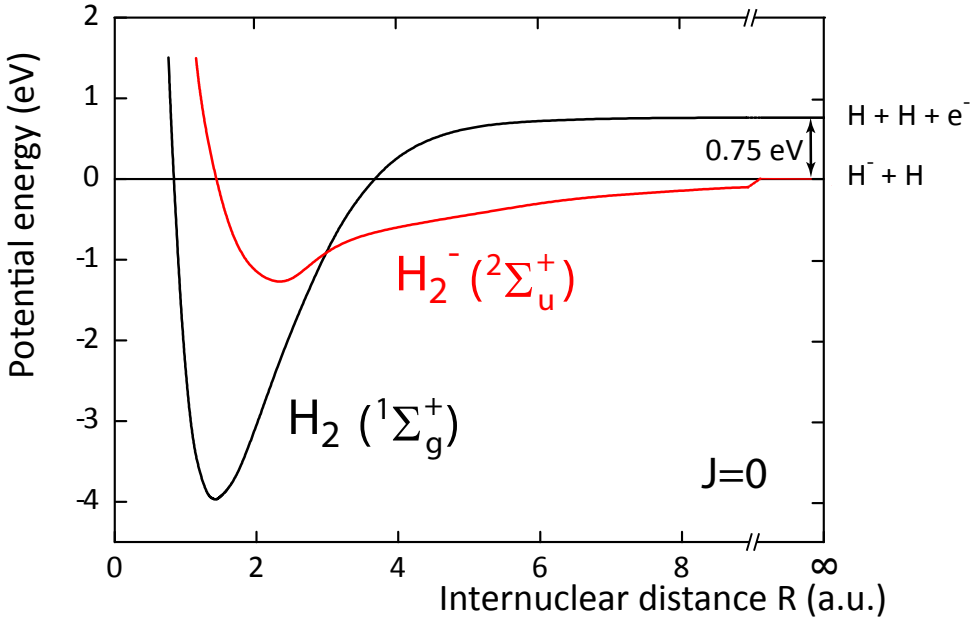

Figure 4.1: Potential curves of H_2 and H_2^-. The H_2^- potential (red) has only a single minimum, occurring above the H_2 potential curve (black). The potential curves were taken from Fig. 1(a) in Ref. [64].

4.1 Diatomic hydrogen anions

4.1.1 Existence of H_2^- and D_2^-

The experimental search for hydrogen molecular anions started with first mass-spectrometric detections of H_2^- that were reported in the 50's and 70's [67, 68, 69]. These measurements were supposedly motivated by early calculations in 1936, showing that the electronic potential curve of the ground state $^2\Sigma_u^+$ of H_2^- has a minimum deep enough to support stable states [70]. In Fig. 4.1 a schematic of the $^2\Sigma_u^+$ potential curve of H_2^- and the $^1\Sigma_g^+$ potential curve of H_2 is shown. For less than 3 a.u., the potential curve of H_2^- is energetically situated above the H_2 potential and thus lies in the continuum states of $H_2 + e^-$. In 1963, calculations showed that the ground state $^2\Sigma_u^+$ of H_2^- is actually unstable with respect to auto-detachment of an electron [71]. Further, Bardsley *et al.* calculated a lifetime of the bound H_2^- state under these conditions of only 10^{-16} s [72]. This lifetime is certainly too short for a possible observation of H_2^- via mass-spectrometry and since also the mass of H_2^- is very close to the mass of isomeric D^- further studies were needed to confirm the

early findings.

In 1984, Bae *et al.* searched again very carefully for the negative anion H_2^- [73]. For this purpose, they directed a positive H_2^+ beam through an alkali metal vapor oven with the hope to form H_2^-. Further, they used a quadrupole deflector as charge separator and energy analyzer. After passing two collimators, the negative anions were supposed to be detected via a Faraday cup or a channel electron multiplier. In their studies they could not find any evidence of H_2^- and so further doubt was cast on the previous detections. At that time the community actually did not believe any negative hydrogen molecular anions exist long enough to be observable.

Finally in 2005, Gloser *et al.* unambiguously identified H_2^- and D_2^- via accelerator mass spectrometry (AMS) at the Vienna Environmental Research Accelerator [17]. The anions were produced in a cesium sputter source with TiH_2 or TiD_2 being the sputtering target. According to the principle of AMS, the anions were selected by their charge-to-mass ratio via an electrostatic analyzer that is combined with a dipole magnet, before they were injected into a tandem accelerator. At the high energy terminal of the accelerator, the electrons were stripped off from the molecular anions and the positively charged fragments were further accelerated. Behind the accelerator the fragments were again selected by their charge-to-mass ratio via a second combination of an electrostatic analyzer and a dipole magnet. Then, the fragments were guided onto an energy sensitive detector. For the identification of the H_2^- molecules e.g., the anions were produced via sputtering on TiH_2. After the source, the ion beam was filtered and only molecules with a charge-to-mass ratio near $-1/2$ e/amu were guided into the accelerator. At this point, the beam was still contaminated by isomeric D^-, which is present due to the natural abundance of deuterium in even the purest TiH_2. In the accelerator, the electrons were then stripped off from the ions and behind the accelerator the beam was mass filtered again. This time only fragments with a charge-to-mass ratio of 1 e/amu, and therefore only H^+ ions arising from accelerated H_2^-, could reach the detector. Since the detector is energy sensitive, two H^+ ions recorded in coincidence gave a unique signal for H_2^- that now identified the molecules unambiguously. Via the time-of-flight from ion source to the tandem terminal stripper,

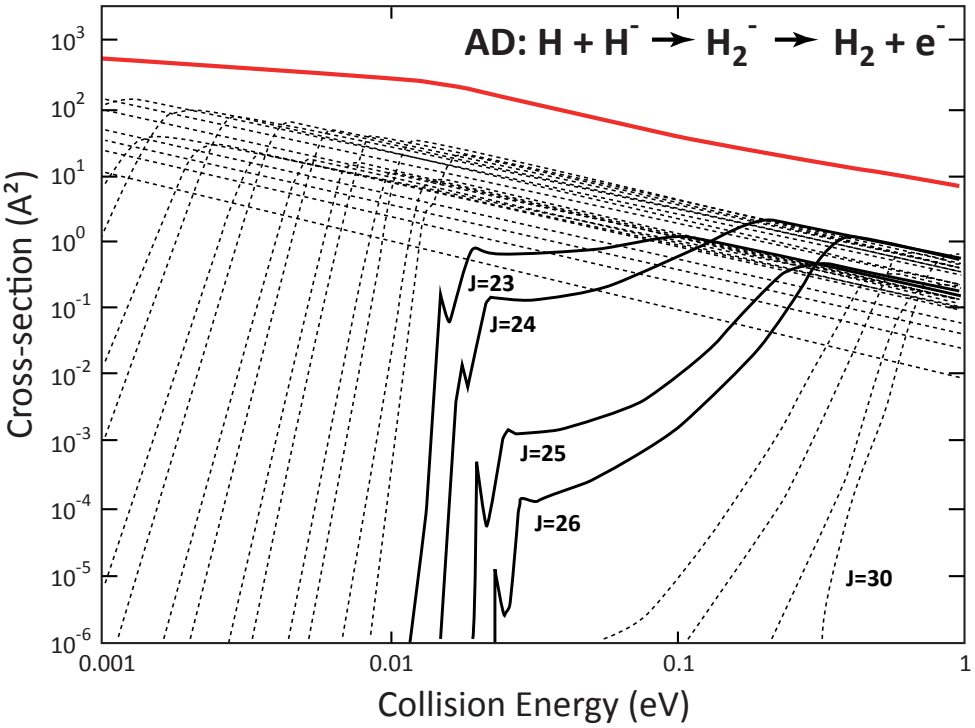

Figure 4.2: Schematic of associative detachment cross section of H + H^- in double logarithmic scale. The total cross section of the process (red) is given by the sum of the partial waves (black). The rotational quantum number J of the partial waves decreases in unit steps from 30 on the right. Metastable states of H_2^- manifest themselves in tunneling resonances of some partial waves (solid black). Due to the low resolution of the plot, the lifetimes cannot be extracted of the resonance widths and, e.g., the resonance of the $J = 20$ state cannot be seen. This schematic was taken from Fig. 2 in [75].

a lower limit of the lifetimes of H_2^- and D_2^- of at least 3 μs and 4 μs was determined, respectively. The observation was also verified by direct mass spectrometry at a very high mass resolution that allowed for the separation of H_2^- and D^- [74]. At this point a theory was required that explains the rather long lifetimes.

4.1.2 Rotationally induced metastability

The hydrogen anions influence the cross section of associative detachment (AD: H + H^- → H_2^- → H_2 + e^-) and dissociative attachment (DA: e^- + H_2 → H_2^- → H + H^-) reactions involving diatomic molecular hydrogen as resonant transient states [15]. In 1998, Čížek

et al. calculated the cross sections of molecular hydrogen AD and DA reactions via a non-local resonant theory [75]. Here, metastable H_2^- manifests itself as tunneling resonances of some partial waves (see Fig 4.2).

The predictions of the AD cross section were successfully tested in merged beam experiments [76, 77]. In these experiments, a neutral H_2 beam, produced via photo-detachment of H^-, was overlapped with a H^- beam at known collision energies. By measuring beam fluxes, overlap volumes and production rates, the total cross section was determined. The results of the measurements that supported theory were insofar important since they allowed for much more accurate simulations of the masses of Population III stars [76].

The close connection of the anions to the AD and DA reactions also explains their impact on different environments and fields. In the primordial universe the chemistry is strongly influenced by AD of $H + H^-$ since this reaction is the most efficient gas phase reaction that formed H_2 [16]. For nuclear fusion devices AD reactions also play an important role for the heating of the plasma [78]. Thus, the experimental fusion reactor ITER requires large quantities of D^- that have to be produced via AD reactions. The anions are then accelerated, neutralized via photo-detachment and finally injected into the plasma where they collide and by this deposit their kinetic energy [79, 80].

The tunneling resonances observed in the cross sections of the partial waves with a high rotational state J gave finally the hint to explain the rather long lifetimes of the hydrogen anions observed by Golser *et al.* [17]. The potential curves depicted in Fig. 4.1 actually change if rotational energy

$$E_{J,\mathrm{rot}}(R) \;=\; \frac{\hbar^2 J(J+1)}{2\mu R^2}\,, \tag{4.1}$$

is added to the non-rotating electronic state energies. Here, μ is the reduced mass and R the internuclear distance. A high J, as shown for $J = 20$ in Fig. 4.3, brings up a centrifugal barrier that peaks at ~ 3 a.u. This creates a second potential minimum at ~ 5 a.u.. As shown in theoretical calculations this potential minimum is deep enough to support bound vibrational levels and H_2^- can exist metastable for $\tau \sim 10^{-12}$ s [17]. Due to

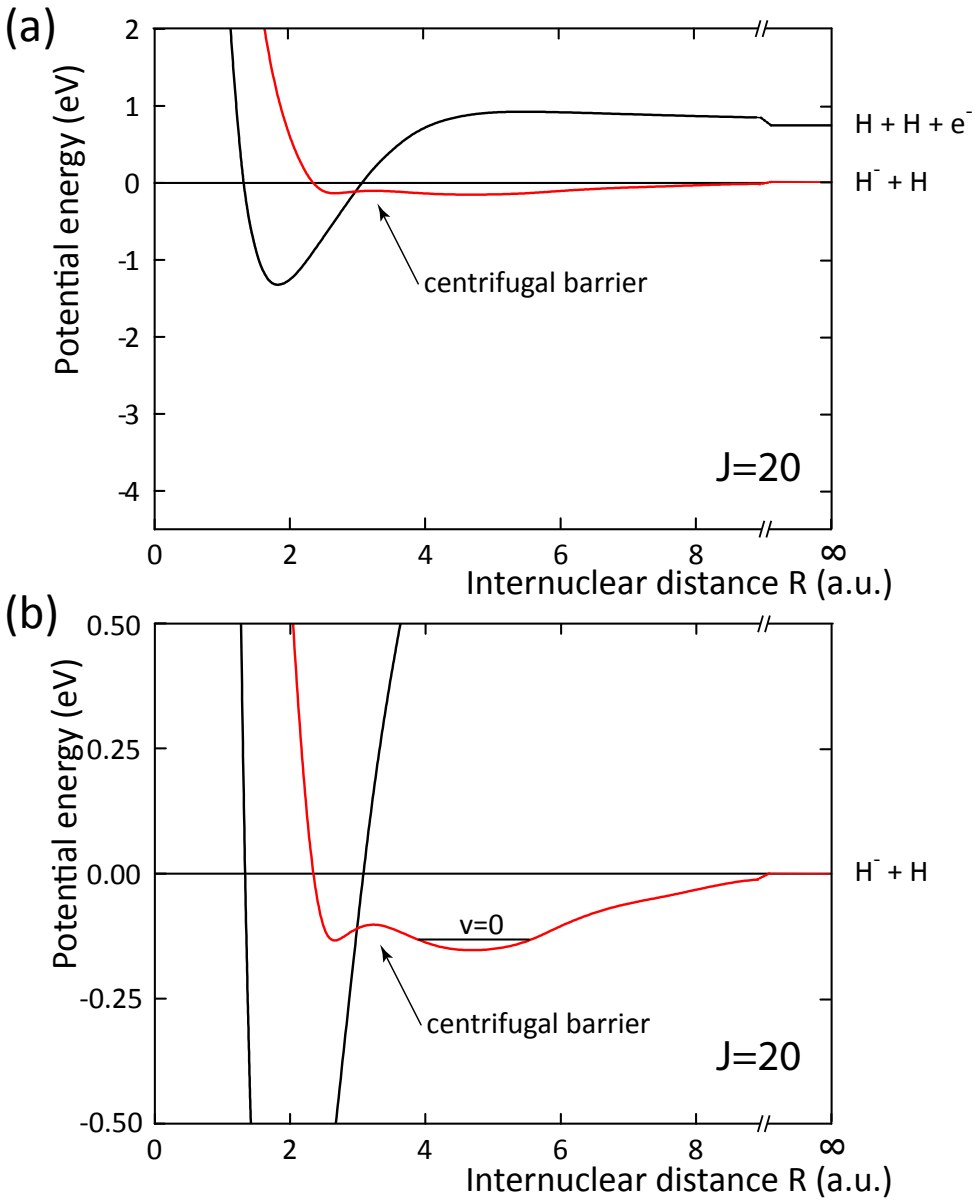

Figure 4.3: Metastability of strongly rotating hydrogen anions. (a) Adding rotational energy (here for $J = 20$) to the potentials depicted in Fig. 4.1 shifts them to higher values and brings up a centrifugal barrier. (b) In a zoom of the curves of (a), a potential minimum of the H_2^- state can clearly be seen outside the continuum state formed by $H_2 + e^-$. H_2^- can exist metastable in this potential minimum.

the strong rotation, this anionic state is much larger than other diatomic molecules and can be considered as a bound system where an H^- ion and an H atom circle around each other.

The same logic applies to several other states of H_2^- with rotational quantum numbers in the vicinity of $J \sim 25$. Also for the deuterated hydrogen anions HD^- and D_2^- a whole "zoo" of stable states exists around $J \sim 27$ and $J \sim 35$, respectively. Without adding energy to the states, they either auto-detach an electron or dissociate, very sensitively depending on the exact shape of the potential. The predicted lifetimes of the states range from $\sim 10^{-12}$ s up to 2 ms and are of course also closely related to the potential shape. Lifetime measurements therefore offer a good way to test the theory.

4.1.3 Tests of the lifetimes and decay channels

Lifetimes

In 2006, Heber *et al.* performed lifetime measurements of the negative molecular hydrogen anions (H_2^-, HD^- and D_2^-) in an electrostatic ion beam trap at the Weizmann Institute molecular physics laboratory [81]. The anions were produced in a cesium sputter source. The sputtered target was either TiH_2, TiHD or TiD_2. The molecules were accelerated to 4.2 keV before they were chopped into few microsecond long bunches, using a deflector. Then, the beam was mass selected by a deflection magnet situated ~ 3.6 m in front of the trap. The trap consists of two electrostatic mirrors between which the trapped ions oscillated. To trap the ions, the entrance mirror was activated as soon as the ion bunch entered the trap. While the ions were trapped, neutral decay products escaped and were detected by a MCP detector that was located behind the exit mirror. Since all possible decay channels produce at least one neutral product, the measured signal is proportional to decay rate of the trapped ions.

An overview of measured and predicted lifetimes of H_2^- and D_2^- is given in Tab. 4.1. For H_2^- and D_2^- the measured lifetimes are up to 8.2 μs and 1890 μs long, respectively.

Table 4.1: Measured and predicted lifetimes of H_2^-, HD^- and D_2^- in μs-range and longer according to [81] (experiment) and [64] (theory), respectively. Rotational quantum numbers J and vibrational quantum numbers v are given for each lifetime τ according to the theoretical predictions. The predicted lifetimes are correlated with the measured lifetimes via the ordering their length: The longest predicted lifetime is related to the longest measured lifetime and so on. Hence, the correlation between predicted and measured states is only true if the predictions of the lifetimes are correct. Except for the $(J = 27, v = 0)$ state of H_2^-, which decays mainly via dissociation, auto-detachment is the dominant predicted decay channel. The predicted lifetimes in brackets are calculated for slight meV-pertubations introduced in the potential. These perturbations influence also the decay channels. Further lifetimes are given in Sec. A.1.

τ_{exp} (μs)	τ_{theo} (μs)	J	v
	H_2^-		
8.2 ± 1.5	0.25 (0.38)	26	0
	0.002 (6.3)	27	0
	HD^-		
50.7 ± 1.0	23 (49)	31	0
	2 (4)	30	0
	0.6 (0.8)	30	1
	D_2^-		
1890 ± 80	2108 (3900)	38	0
84 ± 3	61 (140)	37	0
23 ± 3	16 (17)	37	1
	4 (9)	36	0
	0.9 (1.1)	36	1
	0.5 (0.5)	6	2

When compared, theoretical and measured lifetimes of HD^- and D_2^- agree reasonably but the lifetimes of H_2^- deviate by about one order of magnitude. In 2007, Čížek *et al.* investigated this deviation and calculated the lifetimes with slightly perturbed potentials [64]. Already for meV-perturbations the predicted lifetime of the H_2^- state agrees well with the measurements and the observation could therefore be explained. It should be noted that also the decay channels depend strongly on the exact shape of the potentials.

Decay channels

An investigation of the decay channels (in addition to the lifetime measurements) was performed by Heber *et al.* [81]. For this purpose, they deactivated the electrostatic mir-

rors and combined an electrostatic deflector in the trap with an vertical slit detector as an energy sensitive detector system to identify the fragmentation products. Since the dissociation decay channel is the only decay channel that produces charged fragments, the contribution of the dissociation decay channel to the total decay can in principle be determined via the ratio of the signal of the charged products and the anions.

By this procedure, *dissociation* (yielding D^- and D) was identified as a prominent decay channel of the shortest lived D_2^- state (compare Tab. 4.1). This is in contradiction to the predictions of Čížek *et al.* but the discrepancy may again be explainable by slight meV-perturbations of the potential. The experiments by Heber *etal.* [81] on H_2^- were not able to separate H_2^- from the isomeric D^- and in case of HD^- no dissociation products were observed. While for H_2^- no conclusion concerning the decay channels could be given, it seems that the long lived observed HD^- state decays via auto-detachment as predicted.

In the D_2^- measurements presented in here, we would be sensitive (within limits) to the presence of an auto-detachment decay of D_2^- yielding neutral D_2 as a product, but did not observe this channel as described below.

4.2 Previous studies of the radial wave functions

Another way to test the predictions is the study of the inter nuclear distance distributions of hydrogen molecular anions and hence their nuclear wave functions.

4.2.1 FCEI results on H_2^-

As a precursor work of the presented experiment, the wave functions of H_2^- predicted by Čížek *et al.* [64] were investigated via FCEI at the Max Planck Insitute for Nuclear Physics (MPIK) in 2011 [18]. The Coulomb explosion principle and the FCEI setup at the TSR are discussed in detail in Sec. 2 and the treatment of the rotational excitation of the anion are discussed in Sec. 3. The anions were produced in a cesium sputter source and accelerated to 0.97 MeV by a linear radio-frequency accelerator. Before the FCEI

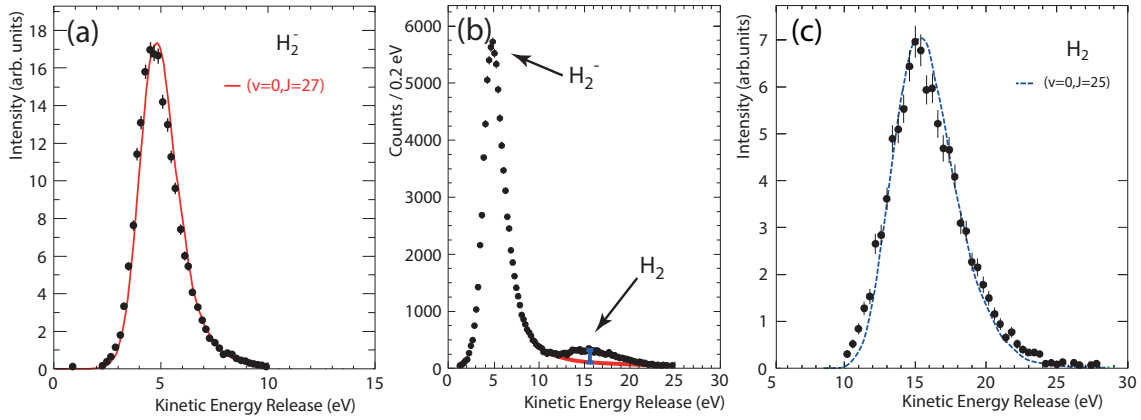

Figure 4.4: Results of FCEI measurements of H_2 and H_2^-. The H_2 and H_2^- distributions were resolved via their different COM positions, which was possible since the earth magnetic field only effects the flight path of the H_2^- anions. (a) Results of the measurements (black points) on H_2^- agree very well with predictions of the $(J = 27, v = 0)$ state (red line). (b) The raw experimental data shows a second peak around 15.5 eV in the kinetic energy release distribution, which was assigned to neutral H_2. The H_2 peak (blue) on top of an estimated background is (red) is depicted. The ratio of the H_2 peak maximum and the H_2^- peak maximum is $r(H_2^-) \sim 240/5700 = 4.2\%$. (c) The measured isolated kinetic energy release (black points) of H_2 agreed with predictions of $J = 25 \pm 2$ (dashed blue line). All Figures were taken from Ref. [18].

measurements the anions were mass selected. The separation of the H_2^- and isomeric D^- is intrinsically given in FCEI measurements since only recorded events with two fragments in coincidence are accepted.

The FCEI results (see Fig. 4.4(a)) for this system agree best with the predicted wave function of the $(J = 27, v = 0)$ state. In these measurements, some H_2^- anions decayed via auto-detachment along the straight section between last bending magnet and the stripping foil. Therefore, Coulomb explosion of neutral H_2 was observed additionally in the raw FCEI data (see Fig. 4.4(b)). The nature of the second, high energy peak in Fig. 4.4(b) was investigated by deflecting the charged anion beam via the auxiliary magnetic field in front of the stripping foil (see Sec. 2.3). This lead to a FCEI spectrum that consisted of a high energy peak only. Since the inter nuclear distance of H_2 is significantly smaller than the inter nuclear distance of H_2^-, the measured kinetic energy release distribution of H_2 appears at much higher kinetic energy releases. When the FCEI results for the

observed H_2 molecules alone was compared to predictions including rotational excitation, the presence of angular momentum near $J = 25 \pm 2$ could be confirmed (see Fig. 4.4(c)).

Moreover, by investigating the relative peak intensities an auto-detachment lifetime of 5 ± 2 μs of the state was determined. This result agrees within the uncertainties with the lifetime determined by Heber et *al*. presented in Tab. 4.1. Since their lifetime measurements includes all decay channels, auto-detachment was identified as the dominant decay channel of the measured state. The measurement is in agreement with predicted lifetime of the $(J = 27, v = 0)$ state when a meV-perturbation [64] of the potential is assumed.

4.2.2 Photofragmentation results on D_2^-

In 2009, Lammich *et al*. performed photofragmentation measurements to test the predicted wave functions of D_2^- at the ELISA storage ring in Aarhus [5]. In these measurements of the molecular structure, the anion was irradiated with a laser pulse. This lead to the photo-detachment of an electron and the subsequent dissociation of the molecule into two neutral D's. The neutral particles were detected via a time and position sensitive detector. For each two body event the kinetic energy release E_{kin} was calculated by combining the impact time difference and the transverse spatial distance. To test the wave functions the measured and predicted kinetic energy release distributions were compared.

A schematic of the principle of photofragmentation is illustrated in Fig. 4.5. After the ionization of the molecule two fragmentation channels open. Theses channels correspond to the ground state $X^1\Sigma_g^+$ and the excited $b^3\Sigma_u^+$ state of D_2. Adding rotational energy shifts the potential curves upwards. In this picture, the rotational angular momentum J of the anion is assumed to be fully transferred to the D_2. As seen in Fig. 4.5, the kinetic energy release is strongly dominated by the rotational energy, especially for an internuclear distance of more than $\sim$ 6 a.u. where the rotational energy contributes almost exclusively to the potential energy. The D_2^- wave function, decaying via the $b^3\Sigma_u^+$ potential, is completely reflected onto the kinetic energy release axis. For the decay via

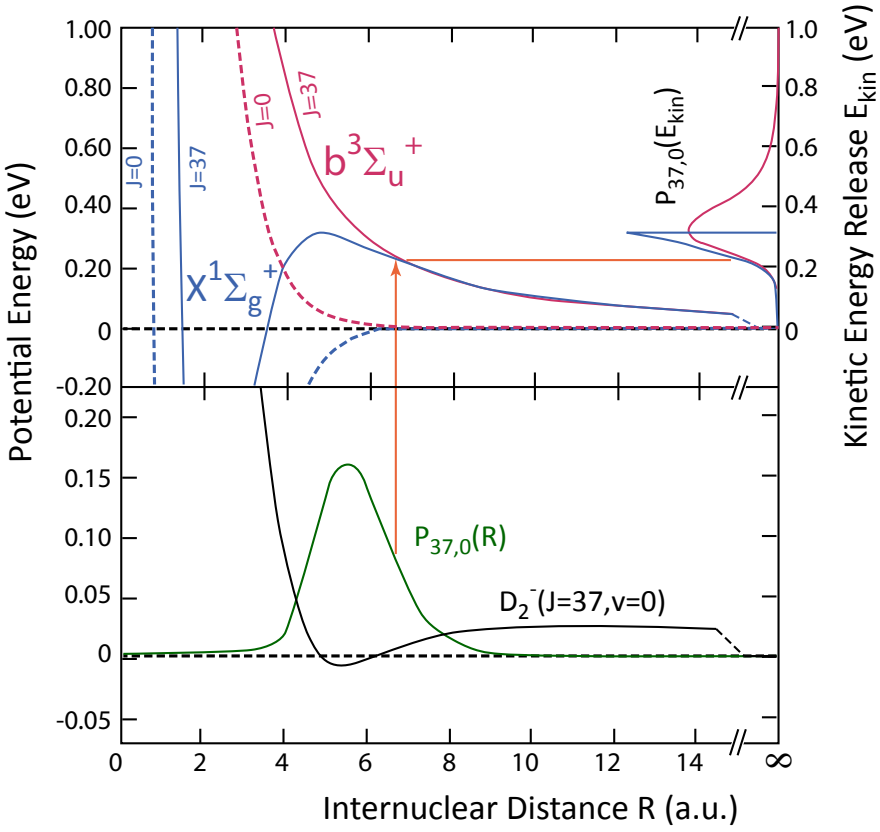

Figure 4.5: Principle of photofragmentation. The potential curve of the $(J = 37, v = 0)$ state of D_2^- is depicted (black). In this picture, the ionization of the anion causes a projection of the squared wave function $P_{37,0}(R)$ (green) onto the kinetic energy release axis via two possible fragmentation channels. The fragmentation channels are the $b^3\Sigma_u^+$ (dashed red) and $X^1\Sigma_g^+$ (dashed blue) potential of D_2. The potential curves are strongly shifted upwards when rotational excitation is considered (solid lines). The shown kinetic energy release distributions $P_{37,0}(E_{\mathrm{kin}})$ are strongly shaped by the rotational excitation.

the $X^1\Sigma_g^+$ potential, the kinetic energy release distribution following from the reflection principle shows a sharp cut at $\sim$ 0.3 eV. This energy corresponds to an internuclear distance of the D_2^- molecules of $\sim$ 5 a.u. and photofragmented D_2^- molecules with a smaller internuclear distance remain bound as D_2. Lammich *et al.* neglected the $X^1\Sigma_g^+$ potential in their analysis, since only for a decay via the $b^3\Sigma_u^+$ potential the wave function is reflected completely and the authors therefore concluded that "it seems likely that the detachment process is dominated by a transition to the $b^3\Sigma_u^+$ state" [5].

For their measurements, they produced the D_2^- anions in a duoplasmatron source, ac-

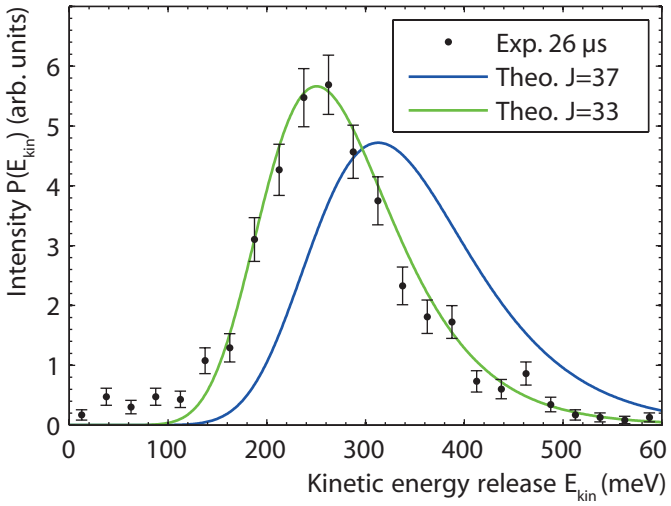

Figure 4.6: Previous results of photofragmentation measurements. The experimental data (black) was recorded 26 μs after ion production. The predicted kinetic energy release of the $(J = 37, v = 0)$ wave function (blue) does not agree with the measurements. When assuming only a rotational excitation of $J = 33$ the kinetic energy release (red) agrees with the measurement even for an approximation of the wave function by the $(J = 37, v = 0)$ wave function. The plot was taken from Ref. [5].

celerated them to 20 keV and mass selected the beam via a separator magnet before they injected the anions into the storage ring ELISA (compare Fig.4 of Ref. [5]). The time of flight of the anions, which includes the one from the source into the ring plus the storage time, was either 10 μs, 26 μs or 107 μs before the ion beam interacted with a crossed, pulsed 532 nm Nd:YAG laser. Neutral fragments were detected via a time- and position-sensitive microchannel plate (MCP) detector, positioned in the extention of a straight section of the storage ring behind one of the electrostatic deflectors.

This 3D detector was equipped with a phosphor screen that was monitored by a CCD camera (Fig. 3 of Ref. [5]). The relative transverse fragment positions were derived with a spatial resolution of ≤ 0.2 mm, while the longitudinal positions are extracted of the relative impact times. This way the kinetic energy release was measured with a resolution of $< 5\%$.

The kinetic energy release was found to be significantly lower than the one predicted assuming dissociation via the $b^3\Sigma_u^+$ potential and the $(J = 37, v = 0)$ wave function. The

discrepancy between the measurement and these predictions is shown in Fig. 4.6 (blue curve). Lammich *et al.* then analyzed their data assuming less rotational energy in the system, while still using the spatial shape of the $(J = 37, v = 0)$ wave function, and found a much better agreement for $J = 33$. This analysis appears reasonable since the kinetic energy release for photodissociation is strongly dominated by the rotational energy and not by the shape of the wave function. Lammich *et al.* concluded that either the predicted angular momentum is overestimated or that the wave functions should be shifted to larger internuclear distances.

Lammich *et al.* also performed lifetime measurements, which allowed them to take calculations by Čížek *et al.* [64] into account for the determination of the relative population of the states. These measurements are mentioned at this point since their results will be included in a comparison of their photofragmentation data to our FCEI measurements on D_2^-. During the measurements the laser was not active and only spontaneously produced neutrals were counted with the MCP detector system. In their analysis the authors made use of the predicted lifetimes and by this they assigned a predicted state to each decay. They observed three different decays related to the D_2^- anion states with a population of 0.6% in the longest lived state $(J = 38, v = 0)$, 44.2% in the second longest lived state $(J = 37, v = 0)$ and 55.2% in the shortest lived state $(J = 37, v = 1)$. This result corresponds to a time since ion production of 10 μs. Also for longer times (26 μs and 107 μs) the relative population of the anion states was measured and can be found in Tab. I of Ref. [5]. As expected, the population of the states changes since their lifetimes are of the order of the times after the ion production (compare Tab. 4.1).

4.2.3 Comparison of the previous results

If one compares the two previous imaging experiments on H_2^- and D_2^-, respectively, the situation looks rather puzzling in particular since the understanding of the isotopologues is based on the same theory. The FCEI measurements of H_2^- agree well with theory and the predicted rotational excitation was even confirmed by the studies of the Coulomb explosion of auto-detached rotating H_2, for which the wave functions are very well known.

At the same time the photo-fragmentation measurements of D_2^- show a severe discrepancy with theory that was in particular attributed to falsely predicted rotational excitation of the bound D_2^- states.

FCEI is a very sensitive technique to measure the shape of the wave function since the kinetic energy release is strongly dominated by the Coulomb energy, while the rotational energy adds $\sim 5\%$. The wave functions are predicted for a specific rotational state and therefore FCEI tests J indirectly. On the other hand, photofragmentation is much more sensitive for almost direct measurements of the rotational state J since here the potentials and therefore the kinetic energy release are strongly defined by the rotational energy as can be seen in Fig. 4.5.

Theory predicts a wave function for a rotational state J, both are therefore strongly related. And so, the contradicting results, in regards of theoretical predictions, can hardly be explained by the different sensitivities both techniques offer. At this point, further input is needed to resolve the situation. This motivated our FCEI measurements of D_2^- that help to test the predictions concerning the structure of the anions. Additionally, we investigated the photofragmentation data and compared them to our results to investigate the rotational excitation of the anions again. Both is presented in the following sections.

4.3 A FCEI experiment on D_2^-

In the puzzling situation, in which one imaging experiment confirms the predicted wave function and the rotational state of the hydrogen anions H_2^- and the other experiment falsifies the predicted rotational excitation of D_2^-, we performed foil induced Coulomb Explosion Imaging (FCEI) of D_2^-.

The experimental setup of this measurement is discussed in Sec. 4.3.1. The measured data are presented in Sec. 4.3.2 and the comparison to theory is shown in Sec. 4.3.3. In Sec. 4.3.4 a look into the photofragmentation data is given and conclusions from our findings are drawn in Sec. 4.3.5.

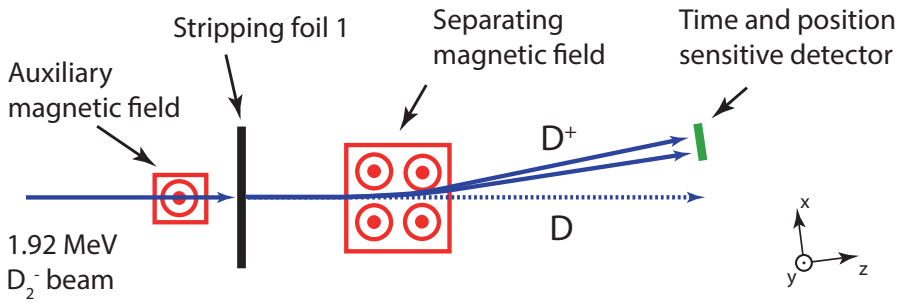

Figure 4.7: FCEI beamline for the D_2^- measurements (top view). The part of the beamline starting with auxiliary magnetic field , where the D_2^- molecules were stripped, is depicted. The separating magnetic field was adjusted in such a way that only D^+ fragments were guided on the round 3D detector. The coordinate system that is aligned via the detector is depicted.

4.3.1 Experimental setup

The FCEI measurements were performed at the Max Planck Institute for Nuclear Physics. In this section, the experimental setup is only very briefly discussed with the focus on the D_2^- measurements since it was already presented in more detail in Sec. 2.3.

The D_2^- was produced in an off axis duoplasmatron ion source before it was injected into a linear radio-frequency accelerator. The anions were accelerated to 1.92 MeV, which corresponds to a molecule velocity of 3.26% of the speed of light. The distance from source to stripping foil was 100 m. Hence, the time-of-flight of the anions was 10.2 μs before they were fragmented. The diameter of the collimator apertures was either 1 mm or 1.5 mm (both values were used during the measurements). The auxiliary magnetic field was deactivated for measurements of the D_2^- wave functions and activated for the search of neutral D_2. In both measurements DLC foil 1 with 1.2 $\mu g/cm^2$ was used.

The Coulomb explosion measurements required the detection of two D^+-fragments in coincidence. Since also neutral D-fragments emerged from the stripping foil (foil effects are discussed in Sec. 2.2.2), the round detector was adjusted to be off axis from the original molecular beam (see Fig. 4.7). Further, the magnetic separation field located behind the stripping foil was set to guide D^+-fragments onto the round detector.

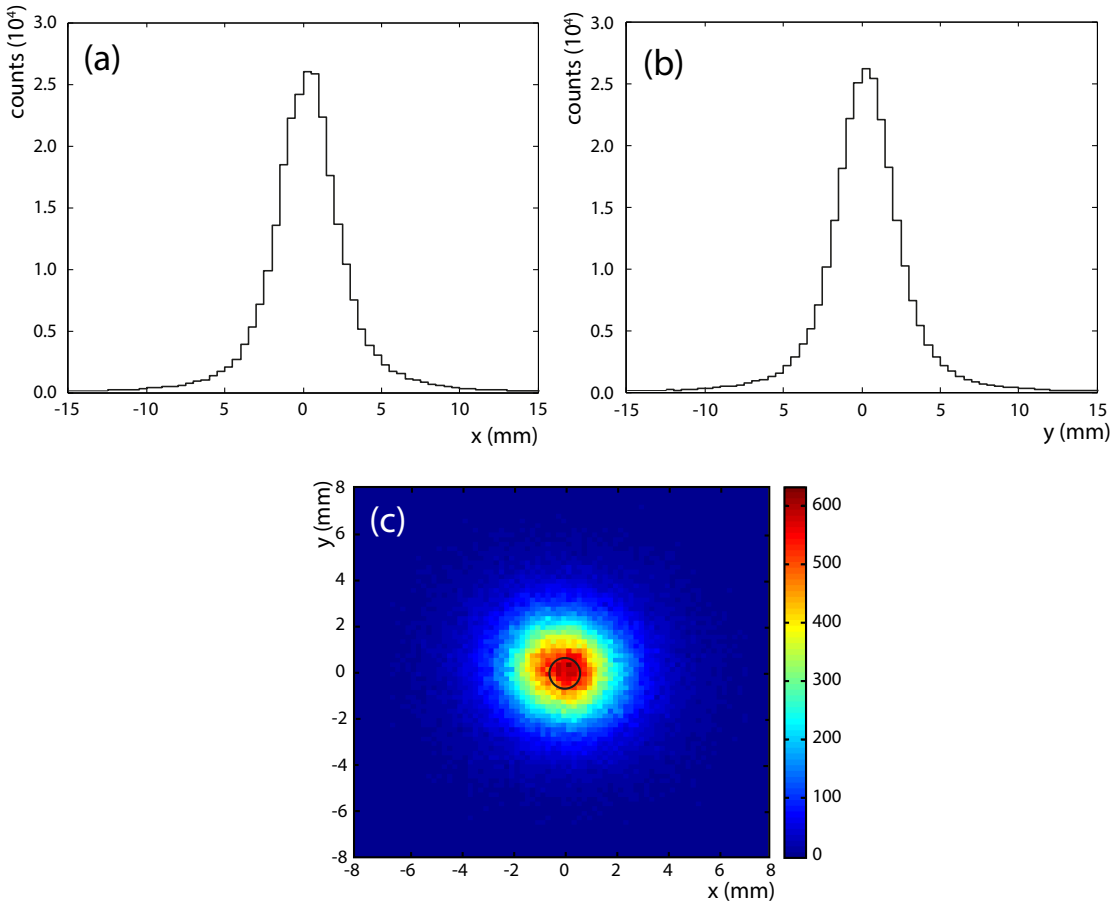

Figure 4.8: COM of all detected two body events. (a) COM projected on the x-axis. (b) COM projected on the y-axis. (c) COM projected on the detector plane. In the detector plane the COM is defined by two collimators in front of the stripping foil. Mainly multiple scattering of the nuclei penetrating the stripping foil smears out the COM position. In order to suppress this effect only events with a maximum distance of 0.5 mm to the central spot (within the black circle) of the COM distribution in the detector plane were accepted.

4.3.2 Experimental data

Center-of-mass distribution

In the first step of the analysis we investigated the distributions of the center-of-mass (COM) of all two body events. These distributions are depicted in Fig. 4.8. In the detector plane, the anion beam was defined by two collimators. By this, the COM position was fixed since the COM of both fragments after the Coulomb explosion followed the direction

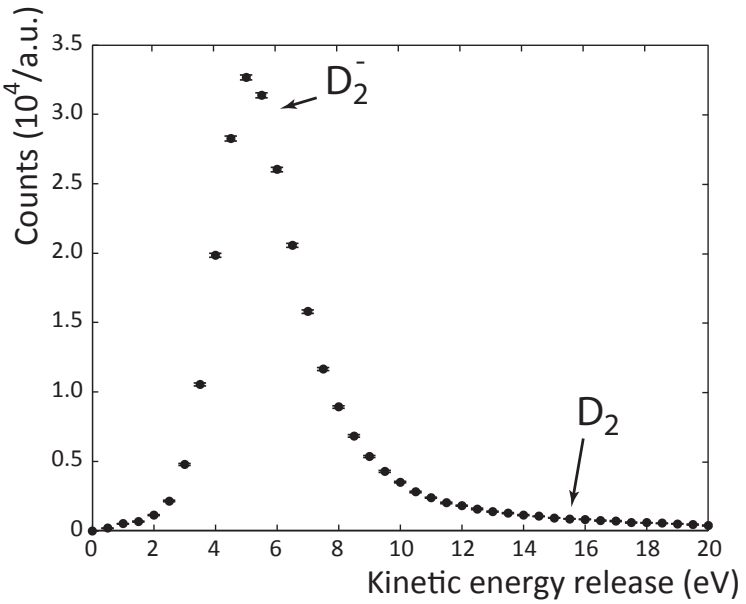

Figure 4.9: Distribution of the raw kinetic energy release of all detected two body events. The distribution peaks at ~ 5 eV. This corresponds to an internuclear distance of the initial molecule of ~ 6 a.u.. When D_2^- auto-detaches an electron in the straight section in front of the stripping foil D_2 can form. D_2 contributions to the measured kinetic energy release, expected at around 15.5 eV (similar to the case of H_2^-, Fig. 4.4(b)), are not visible. The error bars give the statistical 1σ error.

of the original beam. Due to multiple scattering of the fragments inside the foil the shown COM distributions are significantly broader than the spot defined by the collimators (see Sec. 2.2.2).

To account for shifts of the COM, e.g. caused by small drifts of the magnetic separating field, the measured data were sliced in 9 data sets and the central spot of the COM distribution was calculated for each of them. To generate Fig. 4.8 the central spots of the COM distributions of each data slice were centered at the origin of the coordinate system individually and then added.

Kinetic energy release distribution

The measured kinetic energy distributions P_{kin}^{exp} of all two body events, derived as discussed in Sec. 2.1, are depicted in Fig. 4.9. P_{kin}^{exp} peaks at ~ 5 eV. Already at this point of

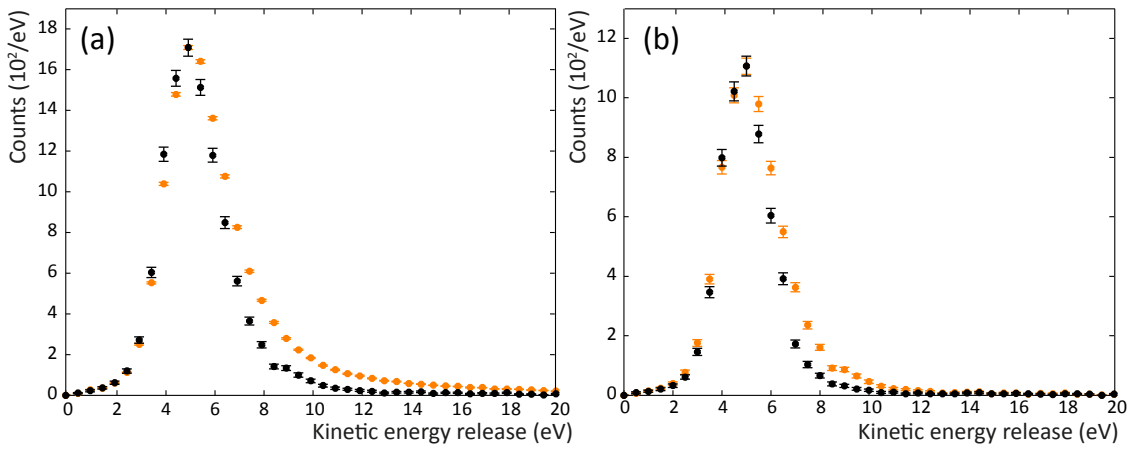

Figure 4.10: Kinetic energy distributions after COM- and additional Angle-cut. The orange and black dots represent the distributions before and after the respective cuts. The distribution before each cut is scaled to equal the height of the distribution after the cut for better comparison. (a) The COM-cut suppresses hard scattered deuteriums, random detector coincidences and detector noise. The low energy tail of the distribution leveled marginally, while the high energy tail is suppressed. The center of the distribution did not shift. (b) The additional Angle-cut suppresses the wake effect. The low energy tail is almost not influenced by the cut. The high energy tail is suppressed. The center of the distribution remains at the same position.

the analysis the investigation of the distribution gives information about the structure of the anion. So does the peak of P_{kin}^{exp} correspond to an internuclear distance of ~ 6 a.u. as a direct consequence of the Coulomb's law. The internuclear distance of D_2^- is therefore significantly larger than the internuclear distance of a neutral hydrogen molecule in the ground state of 1.4 a.u. [61] which corresponds to a kinetic energy release of 19.4 eV. This agrees with predictions of a strongly rotationally excited and therefore extremely stretched D_2^- molecule [64].

The further investigation of the measurements is based on the comparison of our measurements to simulations on the level of the kinetic energy release. For an accurate comparison background events that blur P_{kin}^{exp} have to be suppressed. One background-effect, causing a strong blurring of P_{kin}^{exp}, is multiple scattering of the fragments inside the foil. Since multiple scattering also smears out the COM distributions, it is an established procedure to suppress events where a large amount of multiple scattering occured by accepting only data with a COM near the central spot of the COM distribution (see Fig. 4.8 for the

limit of the accepted events). P_{kin}^{exp} after the COM cut is depicted in Fig. 4.10(a). This cut also suppresses random coincidences, originating from events with two D^+-fragments coming from different anions, and false events caused by detector noise.

An additional effect that blurs the kinetic energy distribution is the wake effect (see Sec. 2.2.2). A charged fragment passing through the foil disturbs its electron density. This influences the trajectories of other charged fragments. The effect is stronger the more the molecular axis is aligned with the flight direction. The orientation of the molecular axis can be deduced from the 3D coordinates measured at the detector relative to the COM of the event. Hence, in order to suppress the wake effect, we accepted only events with $\sin\alpha > 0.48$, where α is the angle between molecular axis and detector plane. The kinetic energy release distribution P_{kin}^{exp} after the Angle-cut is depicted in Fig. 4.10(b). Again, the subtracted events contributed mainly to the high energy tail of the kinetic energy distribution.

Search for auto-detached molecules

During precursor FCEI measurements on H_2^- the auto-detachment lifetime for the observed ($J = 27$,$v = 0$) state of H_2^- was determined [18] (see Sec. 4.1.3). The raw determined kinetic energy release distribution showed a small peak centered at 15.5 eV that had $\sim 4.2\%$ of the height of the H_2^- peak (Fig. 4.4(c)). To identify this peak, all charged particles were in a further measurement deflected via the auxiliary field just in front of the stripping foil. The peak stayed in position while H_2^- contributions disappeared. Therefore, the peak was associated with the Coulomb explosion of neutral H_2, which formed when H_2^- auto-detached an electron in the straight section before the foil (during a drift time of $t_d = 0.47$ μs). An auto-detachment lifetime $\tau_{H_2^-}$ for the observed H_2^- state of (5 ± 2) μs was determined by analyzing the relative intensity of the H_2^- and H_2 peaks.

We tried to apply the same procedure to the D_2^- measurements and carefully checked for neutral D_2 by deflecting the charged particles. However, the number of D's in this further measurement turned out to be too small to be distinguishable from background events. Also the inspection of the measured kinetic energy release distribution P_{kin}^{exp} (in

Fig 4.9) does not show any second peak of D_2. This allows us to estimate an upper limit of the auto-detachment lifetime.

Considering the J quantum numbers predicted for H_2^- and D_2^- states of ~ 25 and ~ 37, respectively, and considering the effective masses μ differing by a factor of 2, one finds that the rotational energy $\propto J(J+1)/\mu$ is predicted to be similar for both molecules. Since also the predicted internuclear distances of both molecules in ground state are nearly the same [82] the D_2 peak should occur close to the H_2 peak position, centered at 15.5 ± 0.2 eV.

Counts in the 15 eV bin can either be caused by background events or by molecular D_2 or D_2^- events. Most of the background events are normally suppressed by the COM cut. However, neutral D_2 events should be searched in all events avoiding this. This is required, because the earth magnetic field deflects only D_2^- such that COM center of the anions is separated from that of neutral D_2. Hence, we compare our raw D_2^- data (Fig. 4.9) to the raw H_2^- data (Fig. 4.4(c)). A density plot of the COM is depicted in Fig. 4.8(c). The plot shows only the center that is attributed the D_2^-.

The "neutral D_2-bin" of 15.5±0.25 eV has 850 counts and the D_2^- peak of (5±0.25) eV has 32660 counts. Since no peak is obvious, a putative peak must be in hidden in the statistical uncertainty of counts in the neutral "D_2-bin" of $\delta(D_2) = \sqrt{850} = 30$ counts. The maximal possible ratio of counts in this peak to the D_2^- peak is thus $r(D_2) = 30/32660 = 0.092\%$. In the H_2^- measurements the ratio of the corresponding peaks $r(H_2^-)$ was $(4.2 \pm 0.5)\%$.

The observed number of D_2 produced during the drift time t_d by the auto-detachment decay rate γ_n of any D_2^- state n can be written as

$$
\begin{aligned}
N(D_2) &= \sum_n N_n \gamma_n \int_0^{t_d} e^{-t/\tau_n} dt && (4.2)\\
&= \sum_n N_n \tau_n \gamma_n \left[1 - e^{-t_d/\tau_n}\right] && (4.3)\\
&\sim t_d \sum_n N_n \gamma_n && (4.4)
\end{aligned}
$$

and the observed number of D_2^- molecules is given by

$$N(D_2^-) = \sum_n N_n e^{-t/\tau_n} \quad (4.5)$$

$$\sim \sum_n N_n \,. \quad (4.6)$$

Here N_n is the number of D_2^- molecules in state n when entering the drift region and τ_n is its lifetime. With a drift length of 6.26 m and molecule velocity of 0.0326c the drift time is $t_d = 0.64$ μs. Even the shortest lived D_2^- state ($J = 37, v = 1$) that can be observed after a flight time of ~ 10 μs has a predicted lifetime of 16 μs (compare Tab. 4.1). Since $t_d \ll \tau_n$ one can expand the exponential function to first order in Eqn. 4.3 and to zero order in 4.5.

With this approximation, the ratio is given by

$$r(D_2) = \frac{N(D_2^-)}{N(D_2)} \cong t_d \sum_n \left(\frac{N_n}{\sum N_n} \gamma_n \right) . \quad (4.7)$$

In the following Section we will show that the D_2^- peak can be interpreted as a superposition of the three predicted anionic states ($J = 37, v = 0$), ($J = 37, v = 1$) and ($J = 38, v = 0$) which are almost evenly populated. Because its lifetime is shortest, we assume the state ($J = 37, v = 1$) to dominate any possible auto-detachment decay. In this case

$$r(D_2) = t_d \frac{N_{(37,1)}}{\sum N_n} \gamma_{(37,1)} \quad (4.8)$$

and with $\frac{N_{(37,1)}}{\sum N_n} = 0.3 \pm 0.1$ we obtain

$$\frac{1}{\gamma_{(37,1)}} = \widehat{\tau}_A > (209 \pm 70) \ \mu\text{s} \,. \quad (4.9)$$

The uncertainty is dominated of that in the relative state population. The determined lower limit of the partial lifetime $\widehat{\tau}_A$ against autodetachment is much larger than the lifetime of the shortest lived state ($J = 37, v = 1$) and hence we can conclude that its

auto-detachment decay is very weak. Therefore, it seems very likely that its decay happens mainly via dissociation, as it was also concluded by Heber *et al.* for this state [81]. This also seems to be likely for the $(J = 37, v = 0)$ state with a total lifetime of 61 μs, while we cannot make a conclusion for the longest lived predicted state $(J = 38, v = 0)$ with a lifetime of 2108 μs.

4.3.3 Results on the structure

Prediction of kinetic energy release distributions

The measurements are compared to theory on the level of the kinetic energy release. For this purpose, the kinetic energy release distributions $P_{J,v}(E_{\text{kin}})$ are simulated via the FCEI simulation individually for the predicted wave functions $\Psi_{J,v}(R)$[1] of Čížek *et al.* [64]. Here, J labels the rotational quantum number, v labels the vibrational quantum number used in the calculation and R is the internuclear distance of the diatomic anion.

The time-of-flight from source to stripping foil was $\sim$ 10 μs, and therefore only the states $(J = 37, v = 0)$, $(J = 37, v = 1)$ and $(J = 38, v = 0)$ of the calculation are stable enough to be observed. The theoretical wave functions $\Psi_{J,v}(R)$ are shown in Fig. 4.11. In preparation for the FCEI simulation, we generated $P_{J,v}(R) = |\Psi_{J,v}(R)|^2$ distributions for each of the three wave functions as input data sets. The generated $P_{J,v}(R)$ distributions are shown in Fig. 4.12. They consist of $2 \cdot 10^6$ single events.

The D_2^- anions are strongly rotational excited and therefore each of its atom has an initial angular momentum, which has to be considered in the analysis (see Sec. 3). Therefore, each event of the input data set was, additionally to the internuclear distance, given initial velocities. The rotational energy of the molecule is given by

$$E_{\text{rot}}^J(R) = \frac{\hbar^2 J(J+1)}{2\mu R^2} \tag{4.10}$$

[1] Two wave functions were available for each state corresponding to either a perturbed or a not perturbed potential (see Sec. 4.1.3). The measured and predicted lifetimes of the not perturbed potential agree better (see Tab. 4.1) and so the corresponding wave functions were used in our analysis.

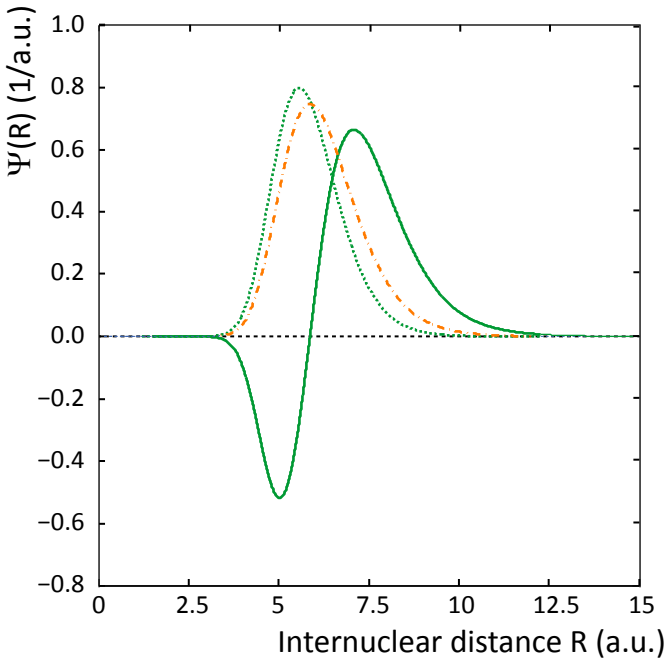

Figure 4.11: Wave functions $\Psi_{J,v}(R)$ of D_2^- predicted by Čížek *et al.* [64] corresponding to the states $(J = 37, v = 0)$ (green dotted), $(J = 37, v = 1)$ (green solid) and $(J = 38, v = 0)$ (orange dash-dotted). The states are stable enough to be observed after a flight time of $\sim 10\mu$s.

in the center-of-mass frame with μ being the reduced mass. Since the atoms of D_2^- share the same mass m_D, the kinetic energy of one deuterium is given by

$$\frac{1}{2} m_D v_J^2 \;=\; \frac{1}{2} E_{\text{rot}}^J(R)\,. \tag{4.11}$$

Hence, each deuterium was given an absolute value of the initial velocity of

$$|v_J(R)| \;=\; \frac{\hbar}{2\mu R}\sqrt{J(J+1)}\,. \tag{4.12}$$

The direction in which the velocity points is also defined: At first, the velocities of the two deuteriums point in opposite directions since the system is rotating. In addition, the direction of the velocities of each deuterium point perpendicular to the molecular and also the rotational axis [18].

The FCEI simulation then calculates the kinetic energy release distributions $P_{J,v}(E_{\text{kin}})$

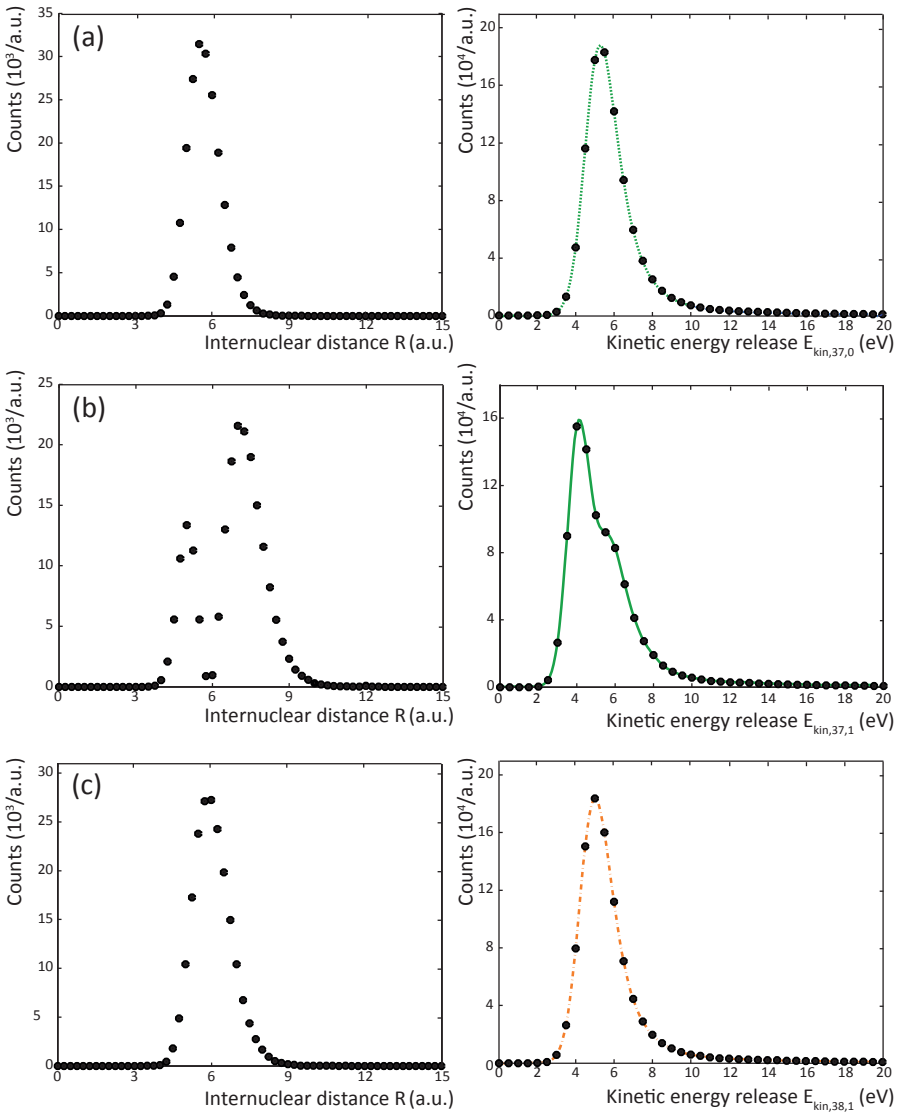

Figure 4.12: Distributions of the squared wave functions and kinetic energy releases for the states (a) $(J = 37, v = 0)$, (b) $(J = 37, v = 1)$, and (c) $(J = 38, v = 0)$. (left) The distributions $P_{J,v}(R)$ are used as input data sets for the FCEI simulation. (right) The $P_{J,v}(E_{\mathrm{kin}})$ distributions are simulated via the FCEI simulation. The distributions are smeared out by multiple scattering and charge exchange processes of the deuteriums in the foil.

taking multiple scattering and charge exchange processes in the foil into account. Also detector resolution and setup geometry are included (see Sec. 2.1). The resulting kinetic energy release distributions $P_{J,v}(E_{\mathrm{kin}})$ are shown in Fig. 4.12 (right handed column). The rotational energy shifts the $P_{J,v}(E_{\mathrm{kin}})$ distributions to E_{kin} values that lie $\sim 5\%$ higher than the rotation less case. Each distribution $P_{J,v}(E_{\mathrm{kin}})$ was normalized to unity, yielding

$\widehat{P}_{J,v}(E_{\mathrm{kin}})$.

Comparison to theory

To compare the predictions to our measurement we fitted superpositions of the simulated kinetic energy release distributions to the measured one, varying the populations of the contributing D_2^- states.

In Fig. 4.13(a) a least square fit of the measured distributions P_{kin}^{exp} with the three simulated and normalized energy release distributions $\widehat{P}_{J,v}$ via

$$P_{\mathrm{kin}}^{exp} = k_{37,0}\widehat{P}_{37,0} + k_{37,1}\widehat{P}_{37,1} + k_{38,0}\widehat{P}_{38,0} \tag{4.13}$$

is shown. The three parameters $k_{J,v}$ determined from the fit yield the relative population of the individual states as

$$Q_{J,v} = k_{J,v} / \sum_{J,v} k_{J,v}\,. \tag{4.14}$$

The fit converged for $Q_{37,0} : Q_{37,1} : Q_{38,0} = 25 : 37 : 38$. The absolute uncertainty of each relative contribution is estimated to $\pm 5\%$. The superposition of the fitted three states reproduces the measurements well. The position of experimental peak and the peak of the fitted superposition agree. This can only happen if the angular momentum is not far from the calculated. Deviations around 2.5 eV are most likely due to bad vacuum conditions during this experiment[2]. Collisions of the anions with the residual gas caused molecular break ups just in front of the stripping foil. As a result, the particles started drifting apart slightly before they got ionized. The kinetic energy release of these events is reduced due to the increased distance between the ions. To minimize the bias of this effect on our fit, events with a kinetic energy release of less than 3 eV were neglected. Due to low statistics, the high energy tail of the distribution starting at "9 eV" was also neglected.

[2] A vacuum leak just 30 cm above the stripping foil was identified during the measurements.

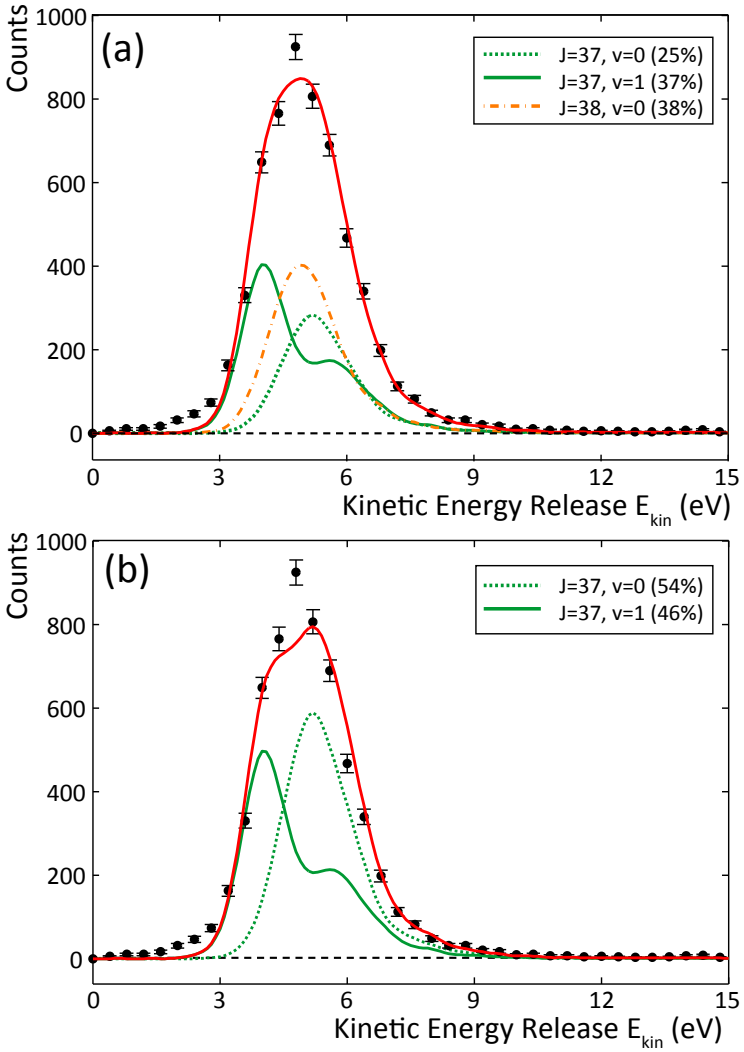

Figure 4.13: Results of the D_2^- measurements. The cutted experimental data is given by the black dots. The simulated events were treated similar to the measured data. (a) The three states $(J = 37, v = 0)$, $(J = 37, v = 1)$ and $(J = 38, v = 0)$ have life times longer than the time-of-flight from the ion source to the stripping foil and can therefore be observed. The superposition of the simulated kinetic energy release distributions (red line) was fitted to the experimental data with the contribution of the single distributions (orange and green lines - see insets) as parameters. (b) Fit of the same data using only the states $(J = 37, v = 0)$ and $(J = 37, v = 1)$. The distributions were simulated using wave functions calculated by Čížek *et al.* [64]. The contribution of the distributions can be seen in the insets.

Table 4.2: The relative population $Q_{37,0} : Q_{37,1} : Q_{38,0}$ of the long-lived anionic D_2^- states is shown for three different measurements including the presented FCEI measurement on D_2^- (accuracy $\pm 5\%$). The time after ion production was for all experiments ~ 10 μs. The ion source type is given.

Measurement	$Q_{37,0}$	$Q_{37,1}$	$Q_{38,0}$	Ion source
FCEI	25%	37%	38%	Duoplasmatron
Lammich *et al.* [5]	44.2%	55.2%	0.6%	Duoplasmatron
Heber *et al.* [81]	$\sim 33.\overline{3}\%$	$\sim 33.\overline{3}\%$	$\sim 33.\overline{3}\%$	Sputter

Heber *et al.* observed three different decays in their lifetime measurements on D_2^-. Since the lifetimes they measured for all states have similar uncertainties one can assume that the states were like in our measurement evenly populated [81] (see Tab. 4.2). In their experiment they used a sputter ions source, while we used a duoplasmatron source. The production process of ions in ion sources is not very well understood and therefore the relative populations of states cannot be well controlled. It is interesting to determine the influence of the natural line width of a state on its population. The natural line width ΔE of a state is related to its lifetime τ for exponential decay via $\Delta E \tau = h$ [83]. The lifetime of the $(J = 38, v = 0)$ state is significantly longer than the lifetimes of the $(J = 37, v = 0)$ and $(J = 37, v = 1)$ state (see Tab. 4.1) and the line width is therefore much narrower. The ratio of the line widths is not reflected in the relative population of the states. The molecules are therefore most likely not produced in a scattering process.

In previous lifetime studies Lammich *et al.* [5] used the same type of ion source (duoplasmatron). They found a contribution of 0.6% of the $(J = 38, v = 0)$, 44.2% of the $(J = 37, v = 0)$ and 55.2% $(J = 37, v = 1)$ state after a time of flight of 10 μs (see Tab. 4.2). We fitted our data allowing for contributions of only the almost exclusively populated two states $(J = 37, v = 0)$ and $(J = 37, v = 1)$ to see if a neglect of the $(J = 38, v = 0)$ state is still in agreement with our data. The fit converged for a relative population $Q_{37,0} : Q_{37,1} = 54 : 46$ and is shown in Fig. 4.13(b). The fit still reproduces the measurements fairly well and thus a negligible contribution of the $(J = 38, v = 0)$ state cannot be excluded. Still, considering the $(J = 38, v = 0)$ state improves the fit.

At this point, the predictions are well reproduced by our measurements. We still cannot

directly analyze J like it is possible for the photofragmentation measurements of Lammich *et al.* [5]. We therefore investigated their findings using their data (see following Sec.).

4.3.4 Comparison with photofragmentation data

Lammich *et al.* performed photofragmentation studies on D_2^- that showed a discrepancy between measurement and theory [5]. They concluded that the predicted rotational angular momentum J is overestimated and consequently also the predicted structure of the anions does not reflect reality (see Sec. 4.2.2). This leaves a puzzling situation as earlier FCEI studies on H_2^- supported the predicted excitation and structure and as also the FCEI studies on D_2^- presented in this thesis are now found to support the predicted structure. In Sec. 4.2.2 we discussed the aspect that photofragmentation measurements give an almost direct access to the rotational angular momentum J unlike FCEI measurements where the Coulomb energy dominates the fragmentation. Hence, we investigated the photofragmentation data by Ref. [5] under the so far unconsidered aspect of an additional decay via the $^1\Sigma_g^+$ channel.

Lammich *et al.* measured the kinetic energy release distributions after times from production of 10 μs, 26 μs and 107 μs (see Fig.6 in Ref. [5]). Due to the short lifetimes of the anions (see Tab. 4.1) the relative populations of the surviving bound D_2^- states was different in each measurement and consequently the measured kinetic energy release distributions are not the same. Clearly, for a comparison with the presented FCEI measurement, the most relevant time parameter is that of ~ 10 μs, corresponding to similar times.

The kinetic energy release distribution at 10 μs after production was compared to fully quantum mechanical calculations of the kinetic energy release using the predicted wave functions of Čížek *et al.* [64]. At first, the kinetic energy release of the states ($J = 37, v = 0$),($J = 37, v = 1$) and ($J = 38, v = 0$) for a decay via the $b^3\Sigma_u^+$ channel and also the $X^1\Sigma_g^+$ channel was calculated (see App. A.2). We assumed that the rotational state J' of the deuterium fragments equals the rotational state of the anion J before its fragmentation,

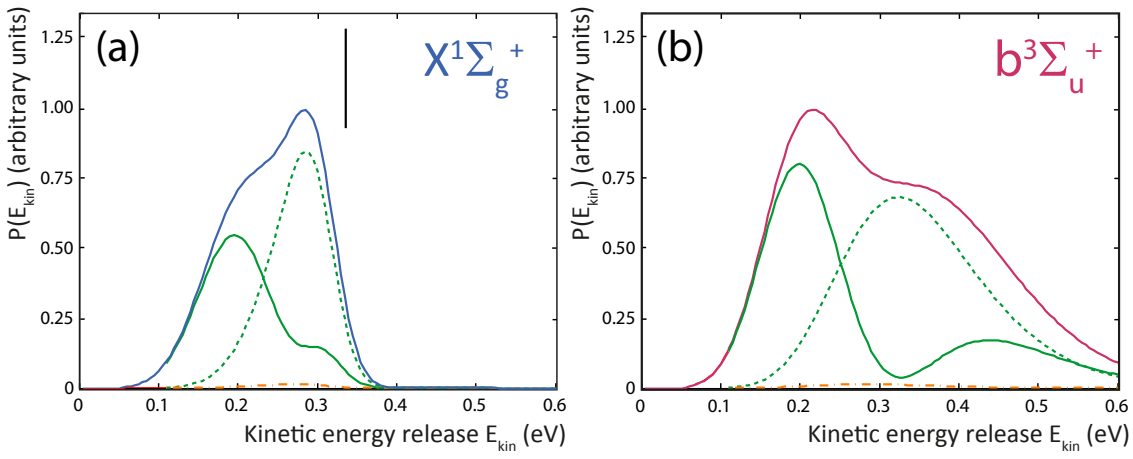

Figure 4.14: Calculated kinetic energy release distributions for a decay via the (a) $X^1\Sigma_g^+$ (blue) and the (b) $b^3\Sigma_u^+$ (red) channel. Each distribution is defined by the superposition of the kinetic energy release distributions of the states ($J = 37, v = 0$) (green dotted), ($J = 37, v = 1$) (green line) and ($J = 38, v = 0$) (orange dash-dotted) that decayed via the corresponding channel with the relative contribution determined by the lifetime measurements of Lammich *et al.*. Each distribution was folded with a Gaussian ($\sigma = 0.02$ eV) to mimic the experimental energy resolution. The peaks of the $X^1\Sigma_g^+$ and $b^3\Sigma_u^+$ distributions were scaled to 1 for this plot. The high energy edge of $X^1\Sigma_g^+$ distribution from the potential shape (Fig. 4.5) is indicated by the black line.

which means that the rotational excitation is transferred fully to the fragmented system. The population of the single anion states at 10 μs was determined in lifetime measurements by Lammich *et al.* to be $Q_{37,0} : Q_{37,1} : Q_{38,0} = 54 : 45 : 1$. We calculated the superposition of the normalized kinetic energy release distributions of all states for each decay channel individually, accounting for these measured populations (Fig. 4.14).

In Fig. 4.15(a) superpositions of the calculated kinetic energy release distribution now including the $X^1\Sigma_g^+$ channel are compared to the photofragmentation measurements. For the comparison we adjusted only the relative contributions of the calculated fragmentation channels ($b^3\Sigma_u^+$ and $X^1\Sigma_g^+$) and scaled the predicted distributions so that their areas equaled those of the measured distribution. We found the best agreement if the $^1\Sigma_g^+$ fragmentation channel contributes significantly with 70%. In this scenario, the discrepancy found by Lammich *et al.* is not reproduced, and in fact a good agreement is found if both fragmentation channels $b^3\Sigma_u^+$ and $X^1\Sigma_g^+$ are allowed. Already here the main features of

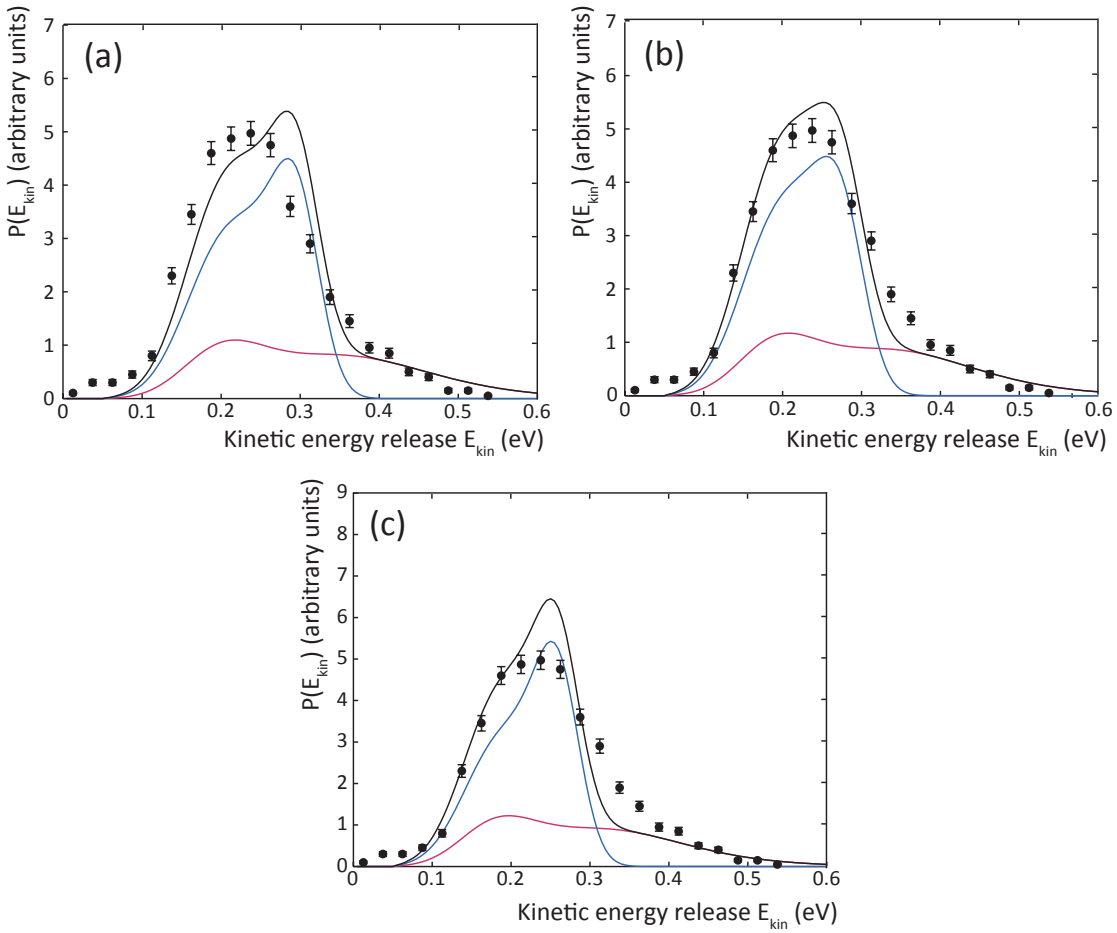

Figure 4.15: Results of the photofragmentation measurements for a tof of 10 μs. The experimental data (dots with 1σ error bars) are redrawn from Fig. 6 of Ref. [5]. The contribution of the $X^1\Sigma_g^+$ (blue) and the $b^3\Sigma_u^+$ (red) distribution to the total kinetic energy release (black) is plotted. The result for different rotational states of the deuterium fragments J' in respect to the rotational state of the anion J are depicted. We assumed (a) $J' = J$, (b) $J' = J - 1$, and (c) $J' = J - 2$. In all plots the relative intensity of both fragmentation channels is $I(X^1\Sigma_g^+)/I(b^3\Sigma_u^+) = 70 : 30$.

the measured distribution are reproduced fairly well, especially since no other parameter than the ratio of the fragmentation channels was adjusted. We therefore assume that the discrepancy observed by Lammich *et al.* is due to the neglect of a possible fragmentation via the $^1\Sigma_g^+$ channel. Their conclusion that theory overestimates the rotational excitation of the anion is not supported by our analysis.

Due to the strong contribution of the $^1\Sigma_g^+$ fragmentation channel the fit is very sensitive

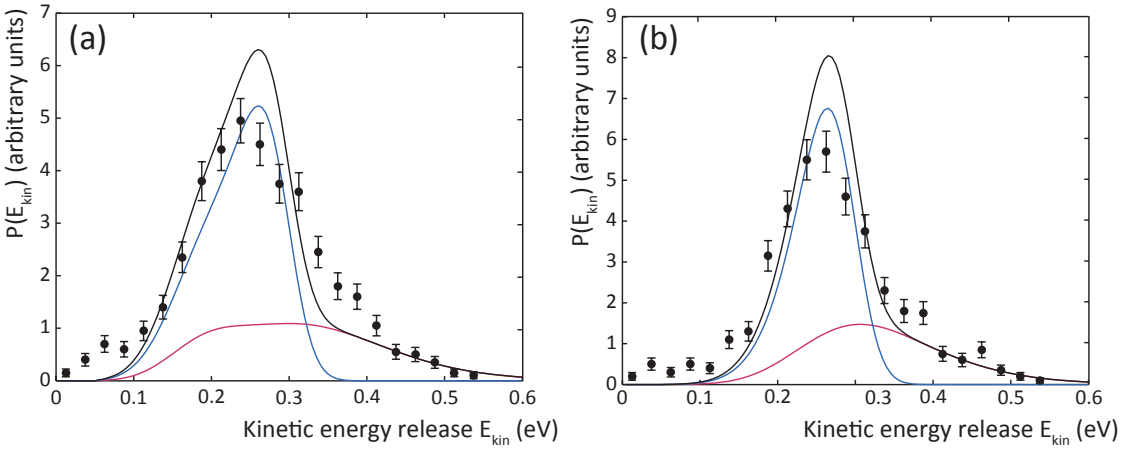

Figure 4.16: Results of photofragmentation measurements for a tof of 26 μs and 107 μs. The experimental data (dots with 1σ error bars) are redrawn from Fig. 6 of Ref. [5]. The contribution of the states according to lifetime measurements was $Q_{37,0} : Q_{37,1} : Q_{38,0} = 68 : 31 : 1$ for the measurements with a 26 μs storage time and $Q_{37,0} : Q_{37,1} : Q_{38,0} = 92 : 3 : 5$ for measurements with the 107 μs storage time. The relative intensity of both fragmentation channels $I(X^1\Sigma_g^+)/I(b^3\Sigma_u^+)$ was 70 : 30. The rotational states of the deuterium fragments J' in respect to the rotational state of the anion J was assumed to be $J' = J - 1$. The contribution of the $X^1\Sigma_g^+$ (blue) and the $b^3\Sigma_u^+$ (red) to the calculated kinetic energy release (black) is plotted.

to the rotational state since the sharp high energy edge of $X^1\Sigma_g^+$ in E_{kin} (see Fig. 4.14(a)) strongly depends on the potential and therefore on the angular momentum J' of the fragments. The R dependence of the wave function is in this scenario negligible. Hence, photofragmentation can be seen as a very sensitive tool to determine J' by investigating exactly this high energy edge. In Fig. 4.15(b) the calculations for $J' = J - 1$ (with $J = 37$ or 38 dependent on the state) are compared to the measurements. This scenario is possible if, e.g., the detached electron carries away one rotational quantum. In contrast to the calculations with $J' = J$ the predicted distribution is shifted by ~ 22 meV to a lower kinetic energy release. The distribution for $J' = J - 1$ reproduces the measurements almost perfectly. Assuming a rotational state of $J' = J - 2$, as shown in Fig. 4.15(c), fails to reproduce the measurements especially at the top of the distribution, but also on the high energy edge. Hence, $J' = J - 1$ is most strongly supported by the measurements and a decay seems to proceed via potential energy curves with $J' \sim 36 \pm 1$.

As a consistency check, we also calculated the kinetic energy release for times since ion production of 26 μs and 107 μs. The comparison to these measurements are shown in Fig. 4.16. The contributions of the single states applied in the model were again extracted from the lifetime measurements. The ratio of both decay channels was here assumed to be $I(X^1\Sigma_g^+)/I(b^3\Sigma_u^+) = 70 : 30$ and we also assumed $J' = J - 1$ since those parameters resulted in the best agreement between measurement and prediction for the time since production of 10 μs. Therefore, no parameter was adjusted. It is remarkable how the calculations still reproduce the data fairly well and only the peaks of the distributions are overestimated. Since the high energy edges of the measured and calculated distribution agree, the rotational state of $J' = J - 1$ is again strongly supported.

4.3.5 Conclusion

We performed FCEI measurements of D_2^- to test predicted wave functions of Čížek *et al.* [64] since in previous photofragmentation measurements by Lammich *et al.* [5] a severe discrepancy between predicted and measured rotational state was reported (see Sec. 4.2).

Our measured kinetic energy distribution is centered at ~ 5 eV. This is in direct agreement with predictions of a very large molecule with an internuclear distance of ~ 6 a.u., which is strongly stretched compared to other molecules by its strong rotational excitation. Our fit of the measurement with the three predicted states $(J = 37, v = 0)$, $(J = 37, v = 1)$, and $(J = 38, v = 0)$ shows good agreement. Therefore, the predicted wave functions seem to be correct. This measurement implicitly tested the rotational excitation of the D_2^- ions, since the wave functions were calculated by theory for a given state with a predicted rotational quantum number J. The discrepancy between theory and measurement regarding D_2^- reported in [5] is not supported by our FCEI measurement on this ion.

We also reconsidered the photofragmentation data as a tool to directly investigate the angular momentum of the D_2^- ion. Here we found that the photofragmentation data agree with the predictions when we consider also a fragmentation via the $^1\Sigma_g^+$ channel that was

so far neglected. This strongly supports the high rotational excitation of $J = 37$ or 38 for the D_2^- ion as predicted in [64] and the calculated R dependence of the wave functions is consistent with the photofragmentation data.

Furthermore we searched for signals of the Coulomb explosion of neutral D_2 molecules formed in the D_2^- beam in order to estimate the auto-detachment lifetime of the bound D_2^- states. We could not identify any contribution of the neutral molecule to our measured data and calculated therefore a lower limit of the auto-detachment lifetime of $\tau_A > (209 \pm 70)$ μs. From this lower limit it seems likely that the shortest lived D_2^- state $(J = 37, v = 1)$ with a predicted lifetime of 21 μs and similarly the second longest lived state $(J = 37, v = 0)$ with a total lifetime of 61 μs decay mainly via dissociation.

With our FCEI measurements and the comparison to the photofragmentation data, we could solve the confusing and puzzling situation concerning the predicted rotational excitation and structure of the anions show that theory has indeed reached a very good understanding of the molecular anions. Nevertheless, small meV-perturbations of the potential of the anions have large impact on their lifetimes and decay channels. Here, future experiments on these properties of the H_2^- and D_2^- metastable states can help to understand the nature of the anions even more accurately.

5 Imaging of a chiral epoxide

Chirality is a fundamental lack of symmetry many objects or systems in nature show, when their mirror images cannot be translated or rotated on top of each other. The specific shape of these complex systems can have a huge impact on the functions in nature but, in the molecular world, the existance of a chiral object is in conflict with the very far going parity symmetry of the fundamental interactions.

Chiral objects can be found in particle physics. Here, the spin of a particle with respect to its velocity defines the helicity of the particle. If the particle mass vanishes, the helicity is constant in all reference systems. These particles are then either right- or left-handed and therefore chiral [84]. In chemistry, especially in stereochemistry which is the discipline that deals with the spatial arrangement of atoms in a molecule, chiral molecules are of great interest. Chiral molecules may exist in two variants, consisting of the same atoms and being the mirror image of each other. Yet, their spatial structures can still be different so that one molecule cannot be superimposed to the other one by any rotation or translation. The two spatial configurations of these variants are called enantiomers [85]. A molecule must have at least four atoms to show chirality.

Molecular chirality challenges the ideas of fundamental physics and especially the symmetry of physical laws [86]. Two years after Heisenberg's formulation of quantum mechanics, in 1927, Hund presented a quantum mechanical model which explained the stability of the enantiomers, making use of the invariance of the mechanical laws under space inversion (parity operation) [86, 87, 88]. He expressed the wave functions of both enantiomers as a superposition of the parity eigenstates. At low energies, the wave functions reside in one of the two wells of the molecular ground state potential surface. Hund estimated the tunneling times between the wells to be of the order of million of years and since each

well is associated to a different enantiomer, his calculations explained the observation of stable enantiomers. His description was in fact the first application of the basic properties of the quantum mechanical tunneling effect even before Gamow's paper on the nuclear α decay [86].

In 1956 Lee *et al.* predicted that parity is not conserved in the nuclear β-decay [89]. One year later, Wu *et al.* confirmed the prediction experimentally [90]. The reason for the parity violation in the weak interaction is that neutrinos have negative helicity [84]. This fundamental parity violation may also have impact on the existence of molecular enantiomers as first discussed by Yagamata [91]. As a result of the contactlike weak interaction of electrons and nuclei of a molecule, a small energy difference between both enantiomers exists and therefore both have different chemical reaction probabilities. So far, however, parity violation in the fundamental molecular interactions has not yet been experimentally observed [86].

Prominent examples for chiral molecules are the amino acids, which are substructures of proteins, or deoxyribose that are building blocks of the DNA molecule. These molecules are central for the molecular basis of life on Earth and, very interestingly, the biologically relevant variants of these molecules often show only one handedness [85]. A part of the scientific community believes that the reason for the homochirality of life is the parity violation in the weak interaction [86].

Today, the determination of the handedness of a molecule is still a very difficult task. In this section, the absolute configuration determination via foil induced Coulomb Explosion Imaging (FCEI) of a chiral molecule is presented, which is linked to the stereochemical standard molecule.

An overview of chirality and its role in stereochemistry is given in Sec. 5.1. In Sec. 5.2, a mathematical equivalent to the Cahn-Ingold-Prelog (CIP) rule is presented. The absolute configuration assignment via FCEI is introduced and tested via a Monte-Carlo simulation. The experimental setup is discussed in Sec. 5.3 and the analysis procedure is explained in Sec. 5.4. In Sec. 5.5, the results and their statistical evaluation are shown. The impact of our measurements on stereochemistry is discussed in Sec. 5.6 and we conclude our findings

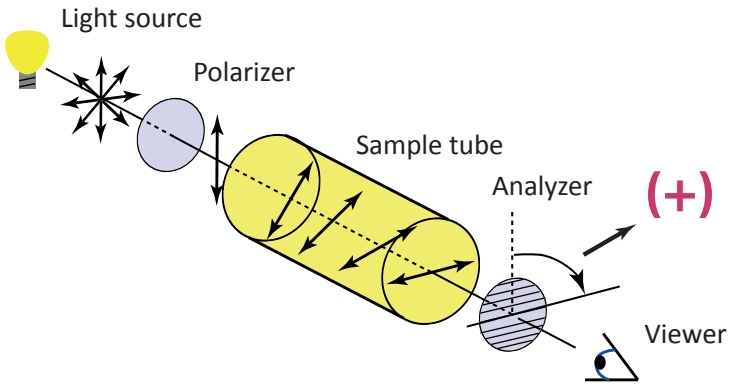

Figure 5.1: Light propagating through an optical active chiral medium. The electric field vector of linearly polarized light rotates in a direction depending on the molecule handedness. As a result, the handedness of chiral molecules can be classified by their optical activity. Rotations to the right or left is labeled (+) or (−), respectively, as shown for the case (+) [92].

in Sec. 5.7.

5.1 Chirality and structure in molecular physics

5.1.1 Ideas of chirality

In 1847, Louis Pasteur was the first to discover chirality in nature when he noticed that tartaric acid crystals exist as two mirror images of each other [93, 94]. He sorted the different crystals by hand and dissolved them separately in a liquid[1]. When he now shone linearly polarized light through each liquid the polarization axis rotated. The direction of the rotation was different for each crystal shape, while for a racemate, a mixture of both variants at equal amounts, the polarization axis did not rotate (see Fig. 5.1) [94]. At a meeting of the Chemical Society of Paris in 1860, Pasteur speculated that the reason for this optical activity may be the asymmetric arrangement of the atoms in the crystal molecules. By this he gave birth to modern stereochemistry [94].

At this time, the optical activity could not be related to the molecular structure, one

[1]His co-workers speculated that this was only possible because of his extreme shortsightedness [95].

reason being that most of the physical properties of chiral molecules, such as their melting point, are identical. Still, if two chiral molecules interact the different enantiomers may show different chemical behavior. The homochirality of biomolecules forming life (see discussion above) implies already that the human body is a partly homochiral[2] environment. An example that demonstrates the different chemical behavior is chiral limonene ($C_{10}H_{16}$) interacting with the human nose. Depending on its handedness, the molecule smells either like citrus fruits or turpentine. Especially, for the pharmaceutical industry the handedness of a molecule is a very important issue since the enantiomers of drugs have different effects in the human body.

The homochirality of live is essential for an efficient biochemistry [85]. One example that illustrates this impressively, is the lock-and-key model developed by Emil Fischer in 1894 [19]. Within this model he postulated that an enzyme can only react on a substrate if both partners have the appropriate shape. By this argument the structure of the molecules became of interest for him. In 1894, it was impossible for Fischer to determine the handedness of a molecule since the different properties of the enantiomers could not be related to the molecular structure and no experimental technique was available to determine it. To have at least a working hypothesis, he arbitrarily assigned dextrorotatory (+)-glyceraldehyde to have (*D*)-configuration[3]. Over many decades to follow, chemists linked this arbitrary structure assignment of glyceraldehyde with the structure of other chiral molecules via chemical reaction correlations, developing a stereochemical network [20].

[2] A homochiral or enantiopure environment consists of only molecules of one handedness.

[3] This notation was introduced by Fischer to relate the handedness of a molecule to its structure. He differentiated the (*D*)-configuration and the (*L*)-configuration. (*D*) and (*L*) stand for dextro (on the right side) and levo (on the left side), respectively. In Section 5.2.1 the more intuitive Cahn-Ingold-Prelog (CIP) rule is presented, which assigns either the (*R*)-configuration (rectus - right) or the (*S*)-configuration (sinister - left). According to the CIP rule, the (*D*)-configuration of glyceraldehyde corresponds the (*R*)-configuration. This is not necessarily true for other molecules.

5.1.2 Methods for determining the handedness

50 years after Fischer's assigment, Bijvoet *et al.* used anomalous X-Ray diffraction (XRD) [96] to determine the absolute configuration of sodium rubidium tartrate crystals, which was chemically linked to glyceraldehyde. Unlike normal diffraction measurements, anomalous XRD is sensitive to the handedness of the molecule since a phase-lag is introduced in one of the atoms forming a molecule by using energy-defined X-rays that exclusively excite it [96]. In their measurement, they found Fischer's assignment to be correct but they stated only very carefully that "the result is that Emil Fischer's convention ... appears to answer the reality". In the following years XRD was established as the standard technique to determine absolute configurations of crystalline chiral compounds [97, 98], although it sometimes leads to false assignments, often due to only small intensity differences of the enantiomers [99, 100, 101, 102, 103].

Further techniques to determine the absolute configuration are vibrational circular dichroism [104, 105, 106] and vibrational Raman optical activity [107], which rely heavily on quantum mechanical ab initio calculations. In the recent years, both methods have been developed to a state where they are extensively used to determine absolute configurations [108]. Both are limited by the wavelength of the used laser and by the accuracy of the theoretical treatment of highly flexible molecules [109]. Lahav *et al.* introduced crystal habit modification by tailor-made impurities to assign the absolute configuration of crystal forming conglomerates via surface interactions [110, 111]. In addition, microscopic techniques can be used to determine the absolute configuration of surface absorbed chiral molecules [4].

A different approach to determine the chirality of gas phase molecules, independent of any quantum mechanical calculations, is Coulomb Explosion Imaging (CEI) in general, as described in the Introduction. Kitamura *et al.* used the CEI technique with highly charged ions (120 keV Ar^{8+}) impacting on vapor molecules to monitor vibrationally induced "dynamic" chirality in perdeuterated methane (CD_4) [7]. The D's of the methane define a tetrahedron, which is expected to "magnify" in the Coulomb explosion process. In the explosion, each D gains an asymptotic velocity in respect to the C. They artificially

introduced chirality in the exploded molecule by ordering three of the four arbitrarily selected velocities by their absolute value and connecting the corresponding vectors according to the ordering of these values. This defines a rotation around the C atom with a given direction and therefore leads to chirality. The direction, either left or right, depends on the initial structure of the molecule and changes with its vibrations. To determine the direction of this rotation they defined an angle depending on the ratios between the three relative velocities. The angle therefore gives access to the different "handedness" of the system introduced by vibrational motion. The measured distributions of angles showed two peaks and therefore a clear separation of angles associated to different handedness. Each handedness was identified equally often within the experimental accuracy, which was expected. Although the chirality was introduced artificially in the molecule by analyzing its vibrational deformation, they concluded that "CEI provides a highly sensitive method of judging the stereochemistry of molecules".

The development of new methods that determine the handedness of chiral molecules is nowadays a busy field. Very recently Berger and Schöffler *et al.* [6] reported, independent from our measurement, an approach to image the "static" absolute configuration of bromochlorofuoromethane (CHBrClF) and of isotropically chiral bromodichloromethane ($CHBr_{37}Cl_{35}Cl$) using cold target recoil ion momentum spectroscopy. Here, the Coulomb explosion of the molecules in a supersonic gas jet is triggered via their interaction with a 40 fs long laser pulse. For both molecules, they neglected the momentum of the H, since the stripping process was rather long and the position of the H in the molecule could not be considered as frozen. Like Kitamura *et al.* [7], they defined an angle via the remaining four particles, which indicated a left- or right-handed coordinate system to differentiate between the enantiomers. The measured samples were a mixture of both enantiomers at equal amounts. The angle distribution showed two clearly separated peaks, one for each enantiomer. In both of their measurements they found an equal number of molecules of each handedness. They concluded, that the direct assignment of the absolute configuration therefore is possible also for "static" chirality. Still, the ionization time via a laser is slow compared to vibration time scales and especially if light atoms are involved the chiral signal smears out easily.

In this thesis foil-induced CEI (FCEI) measurements of trans-2,3-dideuterooxirane ($C_2OD_2H_2$) are presented. For the first time we determined the absolute configuration of a nearly enantiopure sample[4] of molecules in gas phase directly and without the need of any quantum mechanical calculations to relate dichroism or optical activity to the molecular structure. The analysis procedure we developed is based on the stereochemical absolute configuration determination approach (CIP-rule). The determined absolute configuration of the chiral oxirane was chemically linked to glyceraldehyde to test Fischer's assignment and with it the handedness of all molecules arranged in the stereochemical network. Our results on the assignment of the absolute configuration were already discussed in a general scientific journal paper [21] and in more a detailed specialized paper [22]. The synthesis and chemical correlation of the chiral oxirane with glyceraldehyde was published in [23].

5.2 Coulomb Explosion Imaging to determine the handedness of a chiral molecule

Foil induced Coulomb Explosion Imaging (FCEI) was performed on a chiral molecule to determine its absolute configuration by direct imaging. Such an identification of a homochiral probe by direct imaging has in fact never been realized before. The absolute configuration of a molecule is defined by the spatial arrangement of its atoms and its stereochemical description using the terminology defined by IUPAC [112]. This stereochemical description is usually given by the Cahn, Ingold and Prelog (CIP) rule, which relates the handedness of a molecule to its structure [113, 114].

The CIP rule and a developed mathematical equivalent are discussed along with the method for absolute configuration assignment via FCEI in Sec. 5.2.1. We performed our measurements on chiral trans-2,3-dideuterooxirane and the absolute configuration assignment is introduced for this concrete molecule in Sec. 5.2.2. To test our approach we performed simulations that are discussed in Sec. 5.2.3.

[4]The sample contained 97.5 % of molecules with the same handedness.

5.2.1 Absolute configuration assignment

As discussed in Sec. 5, chiral molecules exist in two spatial configurations consisting of the same atoms. Their spatial structures are different in such a way that one molecule is the mirror image of the other. Since the species is chiral, both cannot be rotated or translated to superimpose each other. This defines a property named handedness, which the Cahn, Ingold and Prelog (CIP) rule relates to the structure of *subunits* of a molecule by assigning configurations denoted as (R)- or (S)-configuration. While the determination of the helicity known in particle physics is dependent on only two vectors, in case of chiral molecules multiple properties of the constituent atoms along with the molecular binding types for every subunit have to be considered.

In the following the prescription to assign the absolute configuration of molecules investigated in this thesis is discussed and only single bonds between atoms are assumed. For other molecules additional criteria may have to be taken into account, e.g., how to deal with double or triple bonds or how to deal with axial chirality. Those further criteria are given in [113, 114, 115, 116].

In case of the presently relevant central chirality the different configurations are ascribed to so called chiral centers (marked by *), which are usually formed by a carbon atom. A molecule can have several chiral centers. Each chiral center is connected to four different substituents, which define a tetrahedron with the chiral center in the middle. A substituent consists of an atom or a chain of atoms connected to the chiral center. In case the molecule consists of only four atoms, it generally has a free electron pair, which is then considered as a substituent. The substituent atoms are assigned to spheres. The atoms directly connected to the chiral center are assigned to sphere 1. The next further bound atoms with respect to the chiral center are assigned to sphere 2 and so on (see Fig. 5.2(a)).

To assign the configuration, each substituent is given a priority, which is later related to the spatial arrangement of the atoms. In the CIP definition, the priority is initially given by the atomic number Z of the four atoms of sphere 1. The atom with the highest Z is assigned the highest priority (1), the atom with the second highest Z is assigned the

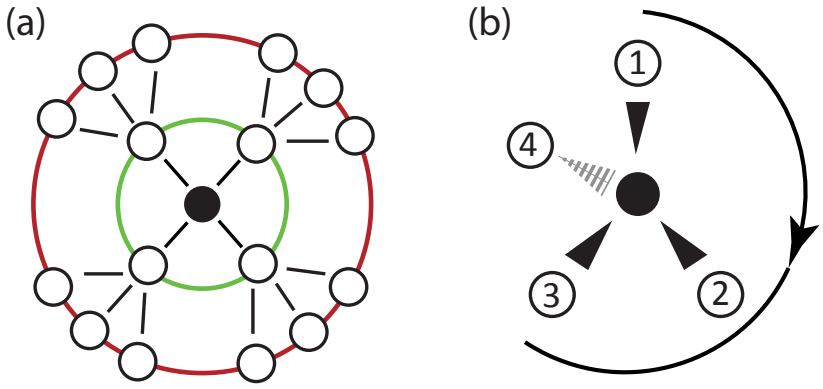

Figure 5.2: CIP-classification of chiral molecules around a single chiral center. (a) Atoms of the four substituents (white) are arranged in spheres that are defined in respect to the chiral center (black). Atoms directly bond to the chiral center are assigned to sphere 1 (green circle), the next further bond atoms to sphere 2 (red circle) and so on. (b) The molecule consists of 4 atoms (white) connected to a chiral center. Atoms connected via the black triangular shaped lines lie before the paper plane, the atom connected with the dashed triangle lies behind the paper plane. If the atomic numbers Z of the substituents are different, they define directly the priority (numbers) of the substituents with 1 being the atom with the highest priority etc.. The three highest prioritized substituents define a rotation direction, which in respect to the lowest prioritized one tells the absolute configuration. The shown chiral center has (R)-configuration.

second highest priority (2) and so on. If there is a free electron pair it is assigned the lowest priority. If the priority assignment is not distinct, the next further bound atoms of sphere 2 are tested. It is possible that several atoms belong to the same substituent in sphere 2. In this case, for each substituent an individual list is generated with the atoms of the corresponding sphere. In this list, the atoms are sorted by their Z, the first entry in this list being correlated to the atom with the highest Z, the second entry to the atom with the second highest Z, and so on. Next, the different atom lists are compared stepwise starting with the first entry. As soon as a different Z is observed, the higher priority is assigned to the substituent with the higher Z. This continues until a decision could be made for all substituents or the end of each list is reached. If the lists have different lengths, it is possible that an atom has to be compared to an empty list position. In this case, the longer list is assigned the higher priority. If the priority assignment is still unclear, this is repeated with the further bound atoms of sphere 3, 4 and so on until the

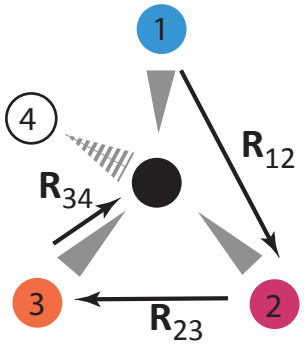

Figure 5.3: Mathematical equivalent to the CIP rule. Three relative position vectors $\vec{R}_{12}$, $\vec{R}_{23}$ and $\vec{R}_{34}$ are defined. The sign of $H = (\vec{R}_{12} \times \vec{R}_{23}) \cdot \vec{R}_{34}$ gives the absolute configuration. The shown chiral center has (R)-configuration, since the sign is positive. The priorities are depicted (smallest number = highest priority and so on).

priorities are distinct or the end of each substituent is reached. Similar to before, a longer substituent is given a higher priority. If a chiral center is part of an aromatic ring, each substituent is investigated until its starting point is reached again. In the case that still no decision could be made, the process is repeated for the unclear substituents with the mass number A being the differentiation criterium. Now a higher A defines in a higher priority.

Once the priorities are assigned, the tetrahedron of a chiral center is aligned in such a way that its constituent with the lowest priority faces to the back. The remaining *three* constituents define a plane. They can always be connected via a rotation from highest to second lowest priority. A rotation to the right (clockwise) identifies the (R)-configuration (rectus - right), a rotation to the left (anti-clockwise) identifies the (S)-configuration (sinister - left) [115] (see Fig. 5.2(b)).

One can specify a mathematical equivalent which relies on a previously made priority assignment and the corresponding direction of the rotation to determine the absolute configuration as defined by the CIP rule. This direct correlation of the stereochemical configuration determination via the CIP-rule with a mathematical model was to our knowledge not discussed before. In the former CEI measurements the identification procedure of the enantiomers was not directly correlated to the CIP rule (see Sec. 5.1) [7, 6].

First, we define three relative position vectors $\vec{R}_{12}$, $\vec{R}_{23}$, and $\vec{R}_{34}$ (see Fig. 5.3) to get access to the three dimensional orientation of the tetrahedron. The indices of the vectors $\vec{R}_{12}$and $\vec{R}_{23}$ correspond to the priorities of the substituents that the vector connects. $\vec{R}_{12}$ connecting the constituent with the highest priority (1) with the constituent with second highest priority (2) and similarly for $\vec{R}_{23}$, while $\vec{R}_{34}$ connects with the chiral center. In principle, it is also possible to connect $\vec{R}_{34}$ to the constituent with the lowest priority (4) instead of the chiral center, since with respect to the plane defined by the first two vectors they point into the same hemisphere. The direction of the rotation is reproduced by $\vec{R}_{12}$ and $\vec{R}_{23}$, while the orientation of the molecule is mimicked by $\vec{R}_{34}$. That means that one could describe the chirality of four-atomic molecules such as $CHDCl^+$, but also any other more complex molecules that show central chirality.

The cross-product $\vec{R}_{12} \times \vec{R}_{23}$ of the two relative position vectors represents the normal of the plane that is defined by the three highest prioritized substituents as specified by the CIP-rule. On the other hand, the triple product

$$H = (\vec{R}_{12} \times \vec{R}_{23}) \cdot \vec{R}_{34} \tag{5.1}$$

equals the volume of the tetrahedron spanned by the involved four atoms multiplied by the factor 6. Its sign is dependent on the relative orientation of the normal and $\vec{R}_{34}$. Considering this property one can define a quantity

$$h = \frac{H}{|H|} \tag{5.2}$$

that assigns the absolute configuration with a well defined relation to the CIP rule. One finds that $h = 1$ for the (R)-configuration and $h = -1$ for the (S)-configuration at the given chiral center. This quantity h is defined molecule per molecule and can be averaged in a series of individual imaging measurements.

In the Coulomb explosion process the structure of a molecule is magnified after its binding electrons are rapidly removed and the charged nuclei repel each other gaining asymptotic velocities $\vec{v}_{ij}$. The crucial point for the measurements of the absolute configu-

ration is that the handedness is conserved during the magnification process, which is true since the explosion takes place in a non-chiral environment and is driven by the parity conserving electromagnetic force. More concretely and for the case of a chiral molecule consisting of four atoms forming a tetrahedron: Before the explosion three arbitrarily chosen atoms define a plane. The fourth atom is on one well defined side of this plane. During the Coulomb explosion of the molecule, this atom will remain on the same side of the plane. Therefore, the sense of chirality is conserved in the Coulomb explosion process that happens in an unchiral environment.

The relative asymptotic velocities $\vec{v}_{ij}$ are recorded by a time and position sensitive detector system (see Sec. 2). After the identification of the fragment species, one can define in analogy to Eqn. 5.1 and Eqn. 5.2

$$H_v = (\vec{v}_{12} \times \vec{v}_{23}) \cdot \vec{v}_{34} \tag{5.3}$$

and

$$h_v = \frac{H_v}{|H_v|} \tag{5.4}$$

as the measure of the configuration of a chiral centers in FCEI measurements. $h_v = 1$ identifies the (R)-configuration and $h_v = -1$ the (S)-configuration.

5.2.2 FCEI of trans-2,3-dideuterooxirane

Choice of molecular species

The goal of our measurement was to test Fischer's assignment (see Sec. 5.1) via a FCEI experiment. Therefore, the chiral molecule that will be imaged has not only to be directly linked to the chemical standard molecule glyceraldehyde but it also has to be produced as an enantiopure probe. In search of an appropriate molecule, Prof. Oliver Trapp of the University of Heidelberg suggested doubly deuterated chiral oxirane $C_2OH_2D_2$ (ethylene

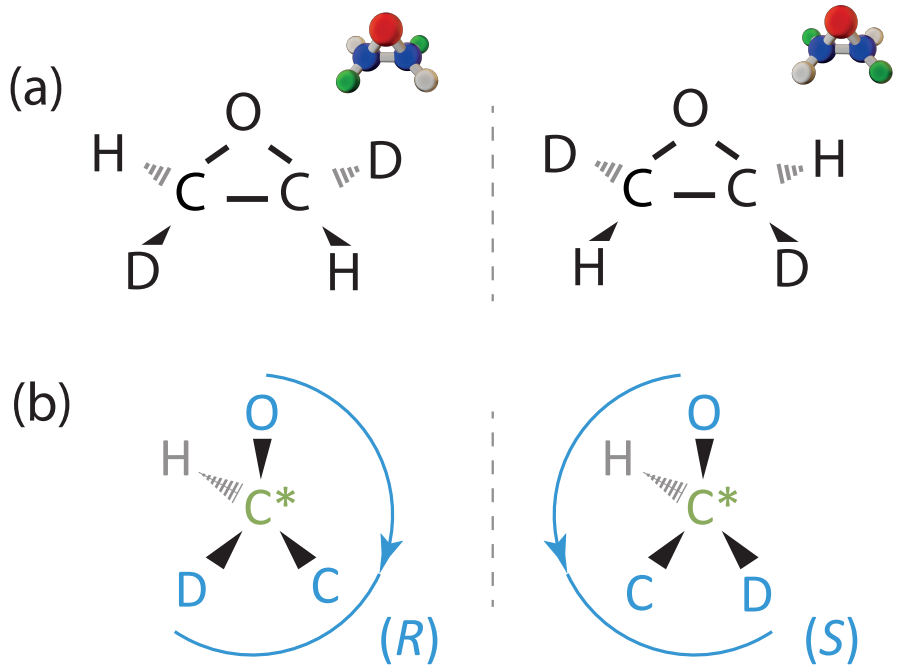

Figure 5.4: The (R, R)- and (S, S)-enantiomers of trans-2,3-dideuterooxirane ($C_2OH_2D_2$). Atoms connected via the black triangular lie before, atoms connected with the lines lie in and atoms connected with the dashed gray triangular lie behind the paper plane. (a) The (R, R)- and (S, S)-enantiomers are depicted in the right and left column, respectively. The position of the H's and D's are exchanged between the enantiomers. Both carbons are chiral centers with the same configuration, due to the C_2-symmetry of the molecule. The molecules are depicted with the atoms in their equilibrium rest positions. (b) The configuration of one of the chiral centers of each enantiomer is determined exemplarily. Each substituent is represented by the atom bound directly to the chiral center. The priority is given by the atomic number Z for O and C. Since H and D share the same Z and no additional atom besides the chiral center is connected to them their priority is defined by the mass number A. The rotation direction with respect to the H gives the configuration. The absolute configuration of the chiral center is depicted.

oxide), which meets these requirements [23]. The two enantiomers of this stable molecule are shown in Fig. 5.4.

In addition, $C_2OH_2D_2$ is a perfect candidate for our measurement concerning the imaging. Its ionization properties, which can be expected to conserve the chirality in the radical cation $C_2OH_2D_2^+$, are discussed below. Hence, these ions of mass 46 amu can be accelerated. Due to limitations of the last bending magnet following the accelerator, the velocity of the molecules impinging the stripping foil is limited and for heavy molecules high charge states of the fragments cannot be produced (see Sec. 2.2.3). Although the suggested molecule is the heaviest molecule on which FCEI measurements were performed with at the Max Planck Institute for Nuclear Physics so far, the beam velocity that can be reached for the chiral oxirane molecules is fast enough to produce sufficiently high charge states of the fragments to support a Coulomb explosion. For the achievable charge state of C^{2+}, O^{2+} and D^+, this was shown already in previous FCEI measurements on DCO^+ and DOC^+ (see Sec. 2.4.3).

Non-chiral undeuterated oxirane (C_2OH_4) consists of seven atoms: one oxygen and two carbons forming a ring and two hydrogens connected to each carbon. It is an organic compound occuring as a colorless flammable gas at 25°C with a faintly sweet odor [117]. Further, it is a liquid at 0°C, while its boiling point at atmospheric pressure is at 10.5°C. Oxirane is soluble in various liquids like water or ethanol and has various applications. It is used, e.g., as a sterilizer for medical devices, since ethylene oxide gas is deadly for viruses, bacteria and fungi [118].

The chiral trans-2,3-dideuterooxirane[5] ($C_2OH_2D_2$) is expected to show the same properties except that the boiling point is slightly higher. In this compound, each C is a chiral center and both share the same configuration. Each enantiomer can be superimposed with itself via a rotation of 180° around an axis going through the O and the middle of the

[5] According to the chemical nomenclature, 'trans-2,3-dideuterooxirane' consists of five parts, which specify the atoms the molecule consists of and give the structure of the molecule: 'trans', '2,3', 'di', 'deutero' and 'oxirane'. As already described oxirane ('oxirane') consists of a C-O-C ring and two Hs connected to each C. The atoms in the C-O-C ring are labeled by 2-1-3. The synthesized molecule is deuterated ('deutero') twice ('di') with one D at each C ('2,3') and in such a way, that both Ds are on different ('trans') sides of a plane defined by the C-O-C triangle.

C-C axis (C_2-symmetry). We will exploit this symmetry in our analysis that is explained later.

FCEI measurements

The chiral oxirane has to be accelerated for the FCEI measurements to 43.9 keV/amu ($\sim$ 1% speed of light) to strip off a sufficient amount of electrons and trigger the Coulomb explosion process (see Sec. 2.1). For this purpose a particle accelerator is used that requires charged molecules, and therefore the chiral molecule has to be ionized by removing one electron in an ion source. It is important, that in this process the chiral information is not lost. Density functional calculations showed that the electron is mainly removed from the oxygen (the most electronegative part of the structure as mostly with oxygen) and that the structures of molecule and ion coincides[6]. The chiral information of this molecule is therefore not expected to be lost. This could mainly occure by the exchange of a D and an H atom forming chiral oxirane to cis-2,3-dideuterooxirane[7].

Due to the limited bending power of the magnets (see Sec. 2.2.3), which guide the molecules from ion source to the stripping foil, the energy of the molecules was limited to 43.9 keV/amu. As discussed below, the analyzed fragmentation events comprised two C^{2+}, and one O^{2+} as well as one D^+ fragment. At the speed of 43.9 keV/amu the fragments also did not penetrate the standard charge multiplication foils in front of our detectors. As a result, the foils had to be replaced and it had to be accepted that the detection efficiency dropped significantly below unity. As a minimum four-fragment coincident events have to be detected. Since both chiral centers of the oxirane share the same handedness, it is sufficient to assign only the absolute configuration to one of them, which can be achieved by detecting the given four fragments (see Sec. 5.2.1). The fragment species were separated via a magnetic field after their Coulomb explosion and guided on different detector positions. The crucial point in the analysis is the determination of the chiral

[6]For the calculations HyperChem 8.07 quantum chemistry program package, Gainesville, Florida, U.S.A was used. The calculations were performed by Prof. Bernd Straub.

[7]According to the chemical nomenclature 'cis' denotes, that the Ds of cis-2,3-dideuterooxirane lie on the same side of the C-O-C triangle. Although the molecule still has two chiral centers, the molecule itself is achiral.

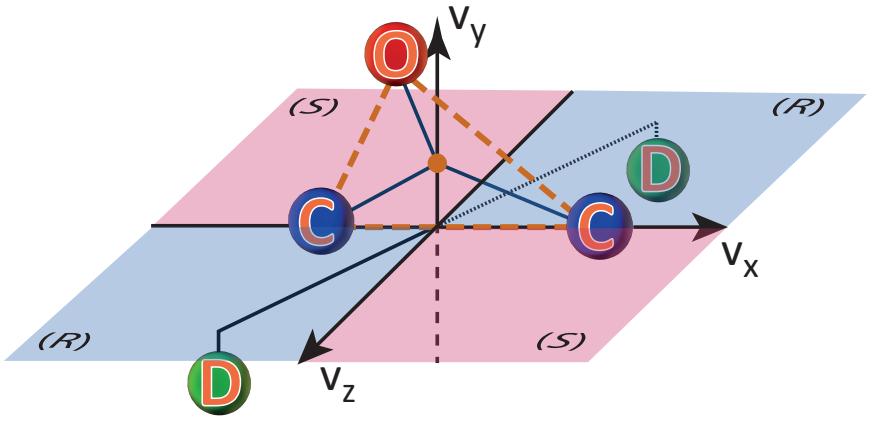

Figure 5.5: Molecule-fixed coordinate system. A coordinate system for each four body event is defined in such a way that the two carbons lie on the v_x-axis and the center of mass of the C-O-C triangle (orange spot) lies on the positive v_y-axis. The position of the detected D is exchange symmetrized. The D's are projected in the v_x-v_z-plane to identify the configuration of the detected chiral center. Each quadrant of the plane is assigned a handedness: D's in blue quadrants identify the (R)-configuration, D's in red quadrants identify the (S)-configuration.

center at which the detected deuterium ion was connected to before fragmentation. This is accomplished by inspecting the deuterium's position (velocity) relative to the triangle formed by the C's and the O (C-O-C-triangle).

For each single-molecule event a coordinate system in velocity space is defined (see Eqn. 2.1) in such a way that both C's lie on the v_x-axis and the center of mass of the C-O-C-triangle lies on the positive v_y-axis (see Fig. 5.5). The orientation of the fragments is ambiguous since a 180° rotation around the v_y-axis of all fragments leads to the same atomic velocity positions. To account for this, the D velocity is exchange symmetrized. If the one observed D fragment has a negative v_x-value, the C with the lower v_x-value is assigned to be the chiral center, and vice versa. After projections of the two thus generated D velocities onto the v_x-v_z-plane, each D identifies the handedness of the configuration by the quadrant it is lying in, according to the CIP-rule and the definition of h_v. Quadrants in red in Fig. 5.5 identify the (S)-configuration and quadrants in blue the (R)-configuration of the detected chiral center.

Extraction of h

Since we detect only four atoms related to one chiral center, we are not sensitive to racemization on a single event basis. To still guarantee that the outcome of our experiment is not biased, the interpretation of the measurement has to be based on the statistical evaluation of deuterium positions for a number of single events.

The chirality parameter H_v in velocity space is defined in Eqn. 5.3. For each event $\vec{R}_{12}$ points from the O to the C, $\vec{R}_{23}$ points from the C to the D and $\vec{R}_{34}$ points from the D to the chiral center C*. Each individual event with $H_v > 0$ ($h_v = 1$) identifies the chiral center the D was attached to as having (R)-configuration, while $H_v > 0$ ($h_v = -1$) identifies the (S)-configuration. For a sample containing 100% of the (R,R)- or (S,S)-enantiomer the expectation value of h_v to be $\langle h_v \rangle = 1$ or $\langle h_v \rangle = -1$, respectively. For a racemic mixture or for cis-2,3-dideuterooxirane $\langle h_v \rangle$ will be 0. The determination of the expectation value is discussed in detail in Sec 5.5.

We performed our FCEI measurements on two samples of chiral trans-2,3-dideuterooxirane: a racemic sample, which contained a mixture of both enantiomers to equal amounts (1:1) and an almost enantiopure sample, which contained 97.5% of one enantiomer. The racemic sample serves as a reference sample, while we determine the absolute configuration of the enantiomer contained in the enantiopure sample.

5.2.3 Simulation of enantiopure data sets

We carried out Monte-Carlo simulations for the foil-induced Coulomb explosion of trans-2,3-dideuterooxirane. The simulation method was described in more detail in Sec. 2.1. It takes multiple scattering and charge exchange processes in the foil into account. A data set containing only (R,R)-enantiomer molecules and a second data set of only the (S,S)-enantiomer molecules were simulated. For the simulations a stick model of the molecule with the atoms in their equilibrium rest positions[8] was used. Initial fragment velocities

[8]For the density functional calculations HyperChem 8.07 quantum chemistry program package, Gainesville, Florida, U.S.A was used. The calculations were performed by Prof. Bernd Straub.

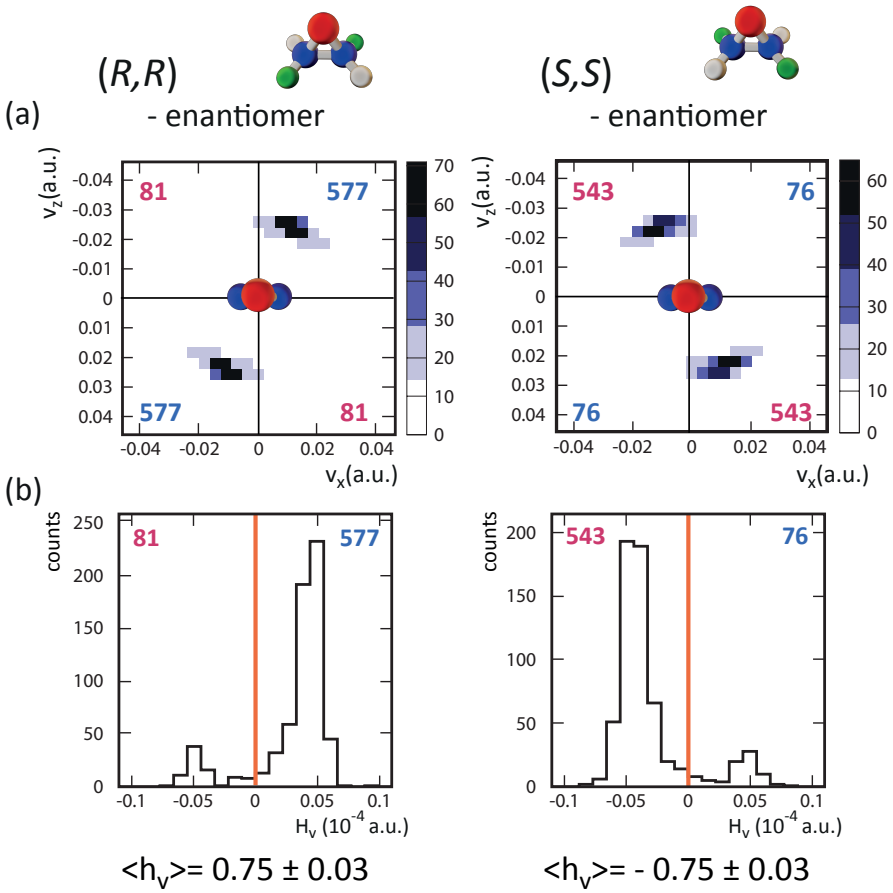

Figure 5.6: Simulation of both trans-2,3-dideuterooxirane enantiomers. (a) The fragments are aligned event per event in the coordinate system shown in Fig. 5.5. The 2D density plots show the D's projected into the v_x-v_z-plane. The numbers represent the number of D's in the corresponding quadrant. Red and blue numbers indicate (S)-configuration and (R)-configuration, respectively. This identification leads in a few cases to false assignments, due to the spread of the deuterium distribution caused by foil effects. The C-O-C triangle is indicated by the red and blue circles. (b) The plots show the H_v-distribution. Positive H_v values assign the (R)-configuration and negative ones the (S)-configuration (see Eqn. 5.3). The expectation value $< h_v >$ is given for both enantiomers.

due to ro-vibrational excitation of the chiral oxirane were neglected. Events with two C^{2+}, one O^{2+} and one D^+, randomly chosen from the two present D^+, were analyzed. These charge states are a compromise between an optimized Coulomb explosion process (high charge states are favored) and the production probability of the charge state.

For each event the fragments were aligned by choosing a coordinate system as shown in Fig. 5.5. 2D density plots, showing the D's of multiple simulated events projected in

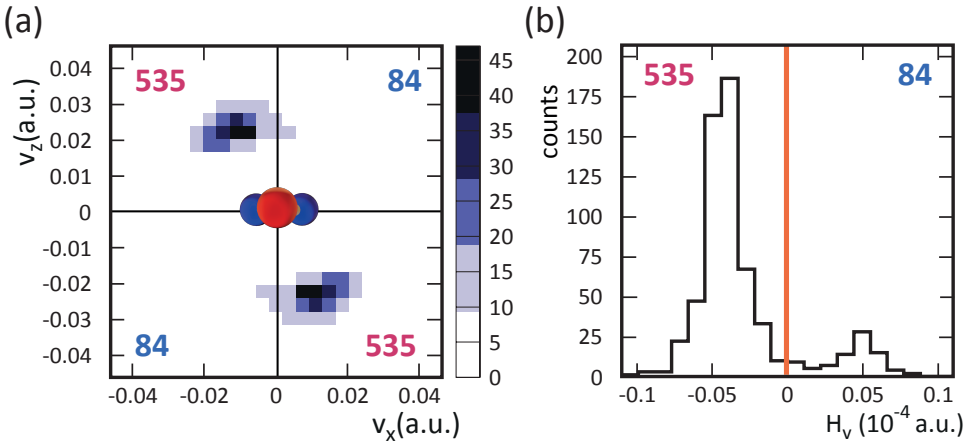

Figure 5.7: Impact of ion position uncertainties on the analysis. The simulated ensemble of the (S, S)-enantiomer shown in Fig. 5.6 was re-analyzed, while the longitudinal separation between both detectors and the transverse position of the O^{2+}-ions were each shifted purposely by 1 cm to mimic the impact of uncertainties. (a) The 2D density plots show the D's in the molecular fixed coordinate system introduced in Fig. 5.5 projected in the v_x-v_z-plane. In contrast to the regular analysis, the introduced error caused the distribution of the D's to spread more strongly. The C-O-C triangle is indicated by the red and blue circles. (b) The H_v-distributions are shown. The peaks are slightly broader compared to the previous analysis without the purposely introduced errors. The expectation value $< h_v >= -0.73 \pm 0.03$. An investigation of the (R, R)-enantiomer showed exactly equivalent results.

the v_x-v_z-plane, are depicted in Fig. 5.6(a). For both configurations the D's accumulate in different spots, and therefore the two enantiomers are clearly distinguishable and show a unique pattern. The deuterium distribution shows exact C_2-symmetry because of the exchange symmetrization of the deuterium positions. The spread of the D's is caused by multiple scattering and charge exchange processes in the foil. The spread leads to a false configuration assignment in a few cases. Fig. 5.6(b) shows the simulated H_v-distributions. For both enantiomers, we identify the correct configuration of the detected chiral centers in 88% of the cases observed. This results in an expectation value of $\langle h_v \rangle = \pm(0.75 \pm 0.03)$ for both enantiomer simulation runs. The definition of $\langle h_v \rangle$ is given in Sec. 5.5.

To estimate the impact of ion position uncertainties on the configuration determination, we purposely shifted recorded fragment positions during the analysis of the simulation. These shifts represent uncertainties that will be introduced in two ways in the analysis of

the measurement. Firstly, we will use two detectors that had to be synchronized in such a way that the longitudinal positions (hit times) of fragments on different detectors can be compared (see Sec. 5.3). Secondly, to identify the fragments, they are guided through a magnetic field (in horizontal plane) that separates them by their charge-to-mass ratio. To address the influence of the separating magnetic field on the ion trajectories, we will have to consider the horizontal positions of each ion charge state center and relate them to the horizontal positions on the detector (see Sec. 5.4.1). We re-analyzed the already shown simulation and purposely shifted the longitudinal positions of the D^+-fragments and the horizontal coordinate of the O^{2+}-ions by 1 cm each. Both introduced errors are larger than the uncertainties we estimated for the corresponding corrections. The result of the analysis of these events for the (S, S)-enantiomer is shown in Fig. 5.7. The errors caused a very small drop in the expectation value $\langle h_v \rangle$ of 0.02 to $\langle h_v \rangle = \pm(0.73 \pm 0.03)$ compared to a simulation without these purposely introduced errors. The analysis procedure is therefore very robust against any uncertainties in the position corrections, which only lead to a "racemization" of the signal.

In the simulation, molecular vibrations and foil polarization effects were neglected. In addition, the repelling potential was simplified to be a point-like Coulomb potential, while the real potential is shaped by the remaining electrons in the C and O ions. As a result, in the 2D representation of the measured data the D-distributions will be smeared out more strongly and a larger amount of false identifications of the chiral centers are expected. Therefore, we expect $|\langle h_v \rangle|$ smaller than 0.75 in our measurement. A method to minimize especially molecular vibrations by inspecting the measured area of the C-O-C-triangle is presented in Sec. 5.4.2.

It is important to point out that our measurements do not aim at the detection of the enantiomeric purity of a given chiral oxirane sample. This can be accomplished by other methods much more accurately. With our measurement we intend mainly to determine the absolute configuration of an enantiopure chiral sample.

5.3 Experimental setup

Based on the considerations given above, we performed FCEI measurements to assign the absolute configuration to an enantiopure trans-2,3-dideuterooxirane ($C_2OH_2D_2$) sample. The assignment required the detection of four fragments in coincidence: Two carbon ions, one oxygen ion and one deuterium ion.

The setup at the TSR was discussed in detail in Sec. 2.3. For the chirality measurements, the gaseous chiral oxirane was ionized in a cold cathode ion source to the radical cation $C_2OH_2D_2^+$ and accelerated by a single-ended Van-de-Graff to a kinetic energy of 2.02 MeV. The energy corresponds to a velocity of the molecules v_{mol} of 0.97% of the speed of light. Both collimators in the FCEI beamline had an aperture of 1 mm and the DLC foil 2 with a thickness of 0.8 μg/cm^2 was used. The auxiliary magnetic field was deactivated.

The separating magnetic field and the detector chamber were adjusted in such a way that O^{2+}- and C^{2+}-fragments were guided onto a rectangular detector and the D^+-fragments onto a round detector. The H^+-fragments were deflected more strongly and were not detected (see Fig. 5.8). The foil-to-detector distance was 2.44 m for the round detector and 2.97 m for the rectangular detector. The O^{2+} and C^{2+} distributions could be observed completely by the rectangular detector (see Fig. 5.9). Although the round detector was moved closer to the foil for this measurement, the D^+-distribution was still slightly larger than the round detector.

Each detector has its own coordinate system (x_d, y_d, z_d) in which the x_d-axis is parallel to the horizontal detector plane pointing in the same direction as increasing magnetic deflection. The y_d-axis is parallel to the vertical detector plane pointing upwards and the z_d-axis is parallel to the longitudinal beam direction pointing with the flight direction. Although the detectors are not perfectly parallel (see Fig. 5.8) we defined a laboratory coordinate system, denoted by the spatial coordinates (x, y, z), in which we treated the axis of the detectors as if they were parallel. The uncertainty we introduce by this measure in the fragment positions can safely be neglected. This is justified, as can be seen in Sec. 5.2.3, where the results of simulations with larger detector position uncertainties

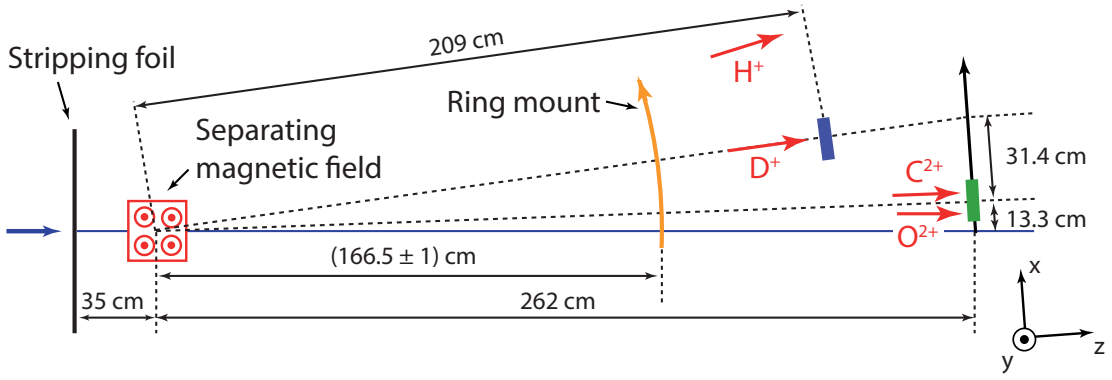

Figure 5.8: FCEI setup for chirality measurements (top view). Both detectors are mounted in the same vacuum chamber with their distance d from each other of 31.4 cm being fixed. The chamber can be rotated around the center of the magnetic field, which allows for the adjustment of the detectors. During the chirality measurements, the chamber was positioned in such a way that the middle of the rectangular detector (green) in x is 13.3 cm away from the flight path of neutral fragments, which can be read out at the ring mount. By additionally adjusting the magnetic field of the separating magnet, the D^+-fragments of the Coulomb exploded oxirane were guided onto the round detector (blue) and O^{2+}- and C^{2+}-fragments onto the rectangular detector. The laboratory coordinate system is depicted. Its center coincides with the center of the rectangular detector. The fragments were identified by their x-position.

are discussed than the ones introduced by this approximation. The laboratory coordinate system (x, y, z) reflects the orientation of the rectangular detector and its origin is defined its center. In the following, detector positions of the fragments are given in this laboratory coordinate system (x, y, z).The molecule-fixed coordinate system shown in Fig. 5.5 is independent of this definition of the laboratory coordinate system.

During the oxirane measurements the two detectors were used for coincidence measurements with different foil-to-detector distances for the first time and therefore had to be synchronized to determine the relative longitudinal positions. During the oxirane measurements the round detector was 52.7 cm closer to the foil and the stop signal, fed into the ADCs of the rectangular detector, was additionally delayed for 186 ns. This compensates for a distance of 53.8 cm. We therefore subtracted $z_0 = 1.1$ cm from the z-coordinate of ions on the rectangular detector. The estimated uncertainty δz_0 is 0.1 cm. It is dominated by the uncertainty of the delay time measurement.

All fragment positions on the round detector were multiplied by the ratio of the different detector-to-foil distances $\sim 30/25$ to account for the different foil to detector distances. The distance between the middle of the round detector projected in the plane defined by the rectangular detector and the middle of the rectangular detector was fixed at $d = 31.4$ cm.

5.4 Data analysis

From the detector hits the fragment types O^{2+}, C^{2+} and D^+ must be identified. Only the D^+-fragments were guided onto the round detector and thus their identification is trivial. O^{2+}- and C^{2+}-fragments were guided to the rectangular detector. Due to the static detector distance and the slow velocity of the molecular ion beam, both ion distribution were not fully separated and partly overlapped by the C^{1+}-distribution (see Fig. 5.9). Hence in contrast to D^+, the identification of these fragments by their x-position is more challenging.

The fragment identification will be discussed next (Sec. 5.4.1). To improve the contrast by suppressing background events, we also developed a filter criterium concerning the area of the C-O-C triangle after fragmentation (velocity space), which is introduced in Sec. 5.4.2. Due to the overlap of the ion distributions on the rectangular detector, the ion identification can go wrong and, e.g., an oxygen can be treated as a carbon and vice versa. We developed a statistical approach to subtract contributions of these falsely identified events from the measured data. This is presented in Sec. 5.4.3. All these procedures enhance the signal-to-noise ratio but do not enhance the signal of one chiral configuration more than the other. Therefore, they do not alter the final conclusions from of the experiment.

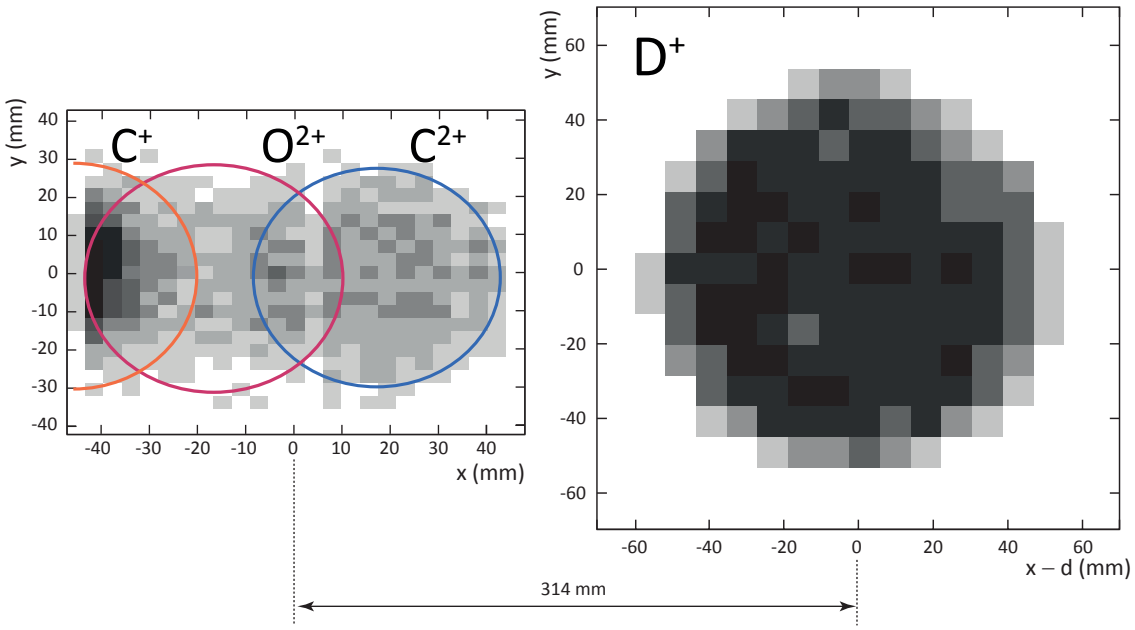

Figure 5.9: Ion impacts on the rectangular and the round detector. The regions where C^+-, C^{2+}- and O^{2+}-impacts are expected are highlighted on the rectangular detector (left). The ion distributions partly overlap. Depicted are events with one, two and three fragments on the rectangular to improve the statistics of this plot. Events with two hits in coincidence on the round detector are depicted in the right panel. This detector is fully covered by D^+-fragments (although it looks like its partly covered due to the binning). The detection efficiency of the round detector is slightly inhomogeneous. This is most likely caused by the charge multiplication foils in front of the MCP since the low energetic D's can barley penetrate the foil and are therefore very sensitive for slight variations of its thickness. The distance between the middle of both detectors d is depicted.

5.4.1 Fragment identification

In the final data taking of the FCEI measurements, we adjusted the magnetic field in such a way that the center of the D^+-distribution coincided approximately with the center of the round detector. From the arithmetic mean of all two body events on the round detector in x we then determined the center of the D^+-distribution $x_0(D^+)$ (see Fig. 5.10(a)). The magnetic field drifted slightly during the measurements. By separating the data in ~2 hour slices we were able to account for these shifts by re-calculating the distribution center $x_0(D^+)$ for each data slice (see Fig. 5.10(b)).

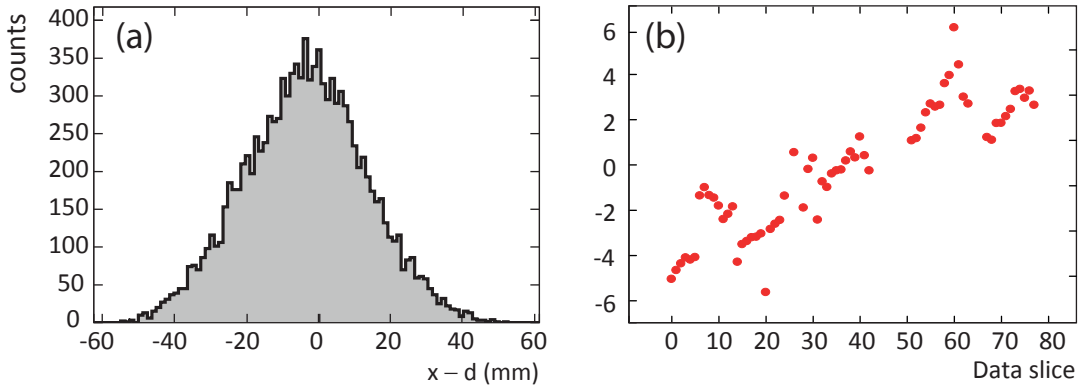

Figure 5.10: Center-of-mass of two body events on the round detector. (a) x-projection of the center-of-mass on the round detector that are depicted in Fig. 5.9. These events were recorded in the first two hours of the measurements. The averaged arithmetic mean corresponds to the center of the D^+-distribution $x_0(D^+)$. For this data slice, tt caluculates as $x_0(D^+) = 309$ mm. (b) Position of averaged arithmetic mean for all data slices.

The detection efficiency of the round detector is inhomogeneous. This can influence the arithmetic mean distribution and therefore $x_0(D^+)$ since two fragments that hit the detector in a more sensitive spot are more likely to be detected than two fragments that hit the detector in an insensitive spot. Hence, the corresponding arithmetic mean of the fragments that hit in the more efficient spot will appear more often and the distribution deforms. To determine the influence of the detector efficiency inhomogeneity on $x_0(D^+)$, we calculated the skewness

$$v = \frac{1}{n}\sum_{i=1}^{n}\left(\frac{x_i - \overline{x}}{\sigma}\right)^3 \tag{5.5}$$

of the distribution. Here, n is the number of the events, x_i is the arithmetic mean of event i, $\overline{x}$ is the averaged arithmetic mean of the distribution and σ is the standard deviation [119]. The skewness v equals 0.004 and therefore the distribution is almost perfectly symmetric[9]. As a result, the detector efficiency does not influence the determination of the charge state center and can be neglected in the following.

[9]For a perfectly symmetric distribution the skewness is 0 and for a completely asymmetric distribution it is ± 1.

Table 5.1: Ion distribution centers $x_0(i)$ with an accuracy of ± 2 mm. The centers were calculated using the calibrated Eqn. 5.6.

i	q_i/A_i	$x_0(i)$ [mm]
O^{3+}	3/16	32.8
C^{2+}	1/6	14.3
O^{2+}	1/8	-22.5
C^{1+}	1/12	-59.3

The deflection in the magnetic field can be approximated by

$$x_0(i) \;=\; \alpha \frac{q_i}{A_i} - \beta \tag{5.6}$$

with the factor α being proportional to the magnetic field strength. Eqn. 5.6 was calibrated by using the determined charge state center of the D^+-distribution and the known detector chamber adjustment (see Fig. 5.8) that defines $\beta = 133 \pm 2$ mm. The uncertainty in β is introduced when reading the exact chamber adjustment on a scale at the ring mount. The COM-distribution determined in the first two hour slice (Fig. 5.10) is centered at $x_0(D^+) = 309$ mm. According to Eqn. 5.6

$$\alpha \;=\; \left[x_0(D^+) - \beta\right] \frac{A_D^+}{q_D^+} \; \frac{e}{amu} mm = 884 \; \frac{e}{amu} mm. \tag{5.7}$$

and therefore

$$x_0(i) \;=\; \left(884 \frac{q_i}{A_i} \; \frac{amu}{e} - 133 \right) \; mm \tag{5.8}$$

with an uncertainty $\delta x_0(i) = \pm 2$ mm. The distribution centers of other fragment distributions $x_0(i)$ can now be calculated (see Tab. 5.1). We repeated this calibration procedure for each data slice. At this point it is important to point out again that the simulation presented in Sec. 5.2.3 has shown that our analysis procedure is very robust against any uncertainty in $x_0(i)$. Deviations from the true value will only result in a racemization of our signal and cannot lead to a false assignment of the absolute configuration.

Next the contribution of the different ions to the observed distribution on the rectangular

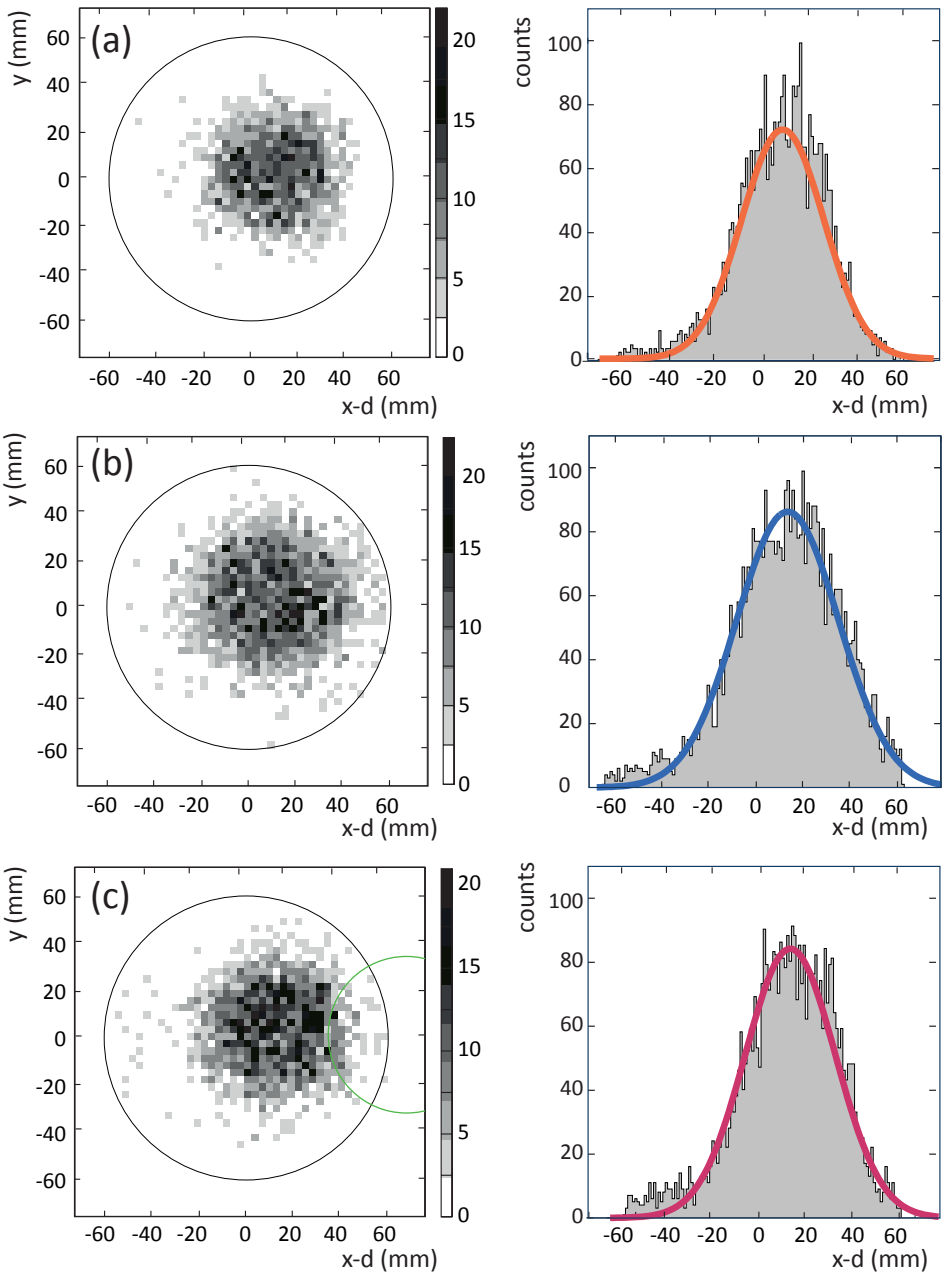

Figure 5.11: Separated (a) C^{+}-, (b) C^{2+}-, and (c) O^{2+}-distributions recorded on the round detector. The overlapping ion distributions of the rectangular detector were separated by increasing the magnetic separation field and guiding the ions on the round detector. The left plots show the distributions projected in the detector plane. The areas within the black circle represent the detector. The right plots show the distributions projected onto the x-axis. The x-distributions were fitted using a box function with soft edges. The C^{2+}-distribution is not fully separated from the O^{3+}-distribution (green circle).

detector was determined. After applying a stronger field on the separating magnet, the ion distributions for C and O fragments could be measured individually on the *round* detector. The distributions in x were fitted by a box with soft edges, which usually agrees very well with individual FCEI ion distributions. The fit function is defined by the difference of two error functions

$$F(x) \;=\; \frac{a}{\sqrt{2\pi}} \left(\int_{-\infty}^{(x-b+c)/d} e^{-(1/2)\,t^2} dt - \int_{-\infty}^{(x-b-c)/d} e^{-(1/2)\,t^2} dt \right) . \tag{5.9}$$

In the least square fit four parameters were adjusted: Parameter a to scale the function, b to define its center, c to account for its width and d to set the rise of its flanks. The distributions and the fit are shown in Fig. 5.11. Using the C^{2+}-distribution, we determined an upper limit of 11% for the intensity of the O^{3+}-distribution relative to the C^{2+}-distribution (see App. A.3). The impact of the O^{3+}-ions on the fit of the C^{2+}-distribution is negligible.

The fitted functions $F_i(x)$ (i for C^+,C^{2+} and O^{2+}, respectively) were now positioned in such a way that the centers of the functions coincided with those of the ion distributions for the magnet settings in the FCEI measurement, shown in Tab. 5.1. Each function was normalized to unity using

$$\int_{x_\mathrm{a}}^{x_\mathrm{b}} \widehat{F}_i(x) dx \;=\; 1\,, \tag{5.10}$$

with x_a and x_b being the detector limits. The normalized $F_i(x)$ are denoted as $\widehat{F}_i(x)$.

With the fragment specific functions the measured x-projection of three body events on the rectangular detector as observed during the oxirane measurements, $P_\mathrm{exp}(x)$ (Fig. 5.12) were analyzed. We normalized the full distribution to

$$\int_{x_\mathrm{a}}^{x_\mathrm{b}} P_\mathrm{exp}(x) dx = 3 \tag{5.11}$$

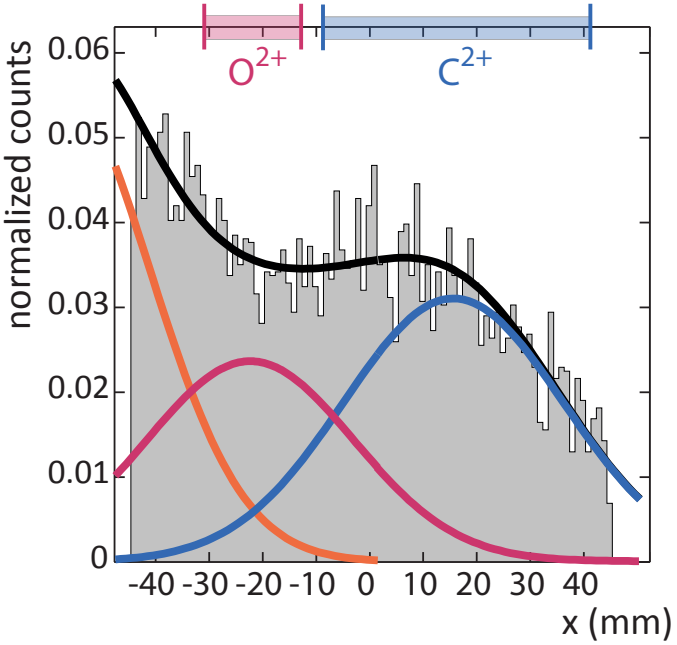

Figure 5.12: Determination of the ion identification windows. The three body events (see Fig. 5.9) recorded on the rectangular detector are projected onto the x-axis. The normalized distribution $P_{\mathrm{exp}}(x)$ (gray) was fitted with $P_\gamma(x)$ (black line). The contribution of the three ion distributions of C^+ (orange), C^{2+} (blue) and O^{2+} (red) to the fit are plotted individually. The C^{2+}- and O^{2+}-windows are highlighted by the red and blue bar in the top of the plot, respectively.

to account for the three detected fragments. Next we defined three functions

$$P_{\mathrm{O}^{2+}}(x) = \widehat{F}_{\mathrm{O}^{2+}}(x)\,, \tag{5.12}$$

$$P_{\mathrm{C}^{+}}(x) = 2\gamma\widehat{F}_{\mathrm{C}^{+}}(x) \tag{5.13}$$

and

$$P_{\mathrm{C}^{2+}}(x) = 2\,(1-\gamma)\,\widehat{F}_{\mathrm{C}^{2+}}(x)\,, \tag{5.14}$$

with γ being the probability of a detected carbon fragment to be singly charged. The sum of the three functions

$$P_\gamma(x) = P_{\mathrm{O}}(x) + P_{\mathrm{C}^{+}}(x) + P_{\mathrm{C}^{2+}}(x) \tag{5.15}$$

was fitted to the normalized x-projection $P_{\mathrm{exp}}(x)$, with the only fit parameter being γ. The

fit converged for $\gamma = 0.27$ and is shown in Fig. 5.12. We defined O^{2+}- and C^{2+}-windows to identify the according fragments by their x-position on the rectangular detector. To maximize the likelihood of a correct ion identification, the centers of the windows were chosen to coincide with the centers of the corresponding ion distributions. The full width of the O^{2+} windows was chosen to be 18 mm and the that of the C^{2+} windows was chosen to be 50 mm (see colored ranges in Fig. 5.12). It is obvious that the ion distributions overlap and therefore some false ion identifications are inevitable. We performed a fit that also allowed for contributions of O^{3+}-ions to $P_{\mathrm{exp}}(x)$. This fit resulted in a negligible contribution of O^{3+}. In the following analysis we neglected O^{3+} ions.

For the further analysis, we accepted events with one hit in the O^{2+} window, two hits in the C^{2+} window and one or two hits on the D^+-detector. Events with two hits on the D^+-detector were split into two events in such a way that both events share the C-O-C triangle but each event has a different D.

Finally, the corresponding distribution center $x_0(i)$ of the identified charge state (see Tab 5.1) was subtracted from the measured x-position of each fragment to account for the influence of the separating magnetic field on their trajectories. Now, the detector positions represent the asymptotic velocities $\vec{v}_{ij}$ of the fragments gained in the Coulomb explosion process. The velocities were calculated according to Eqn. 2.1.

5.4.2 Study of the C-O-C geometry

At this point of the analysis we are able to study the Coulomb explosion of the molecule. As a first step we investigated the area of the C-O-C triangle after the Coulomb explosion that is in velocity space,[10] using all events remaining after the ion identification cut described in Sec. 5.4.1. The distribution of the velocity space area A_{COC}, , after this first cut is shown in Fig. 5.13(a). The observed A_{COC}'s range between 0 and 36×10^{-5} (a.u.)^2. The peak of the distribution is at $\sim 16 \times 10^{-5}$ (a.u.)^2.

Especially the occurrence of comparatively small areas is quite astonishing at this point,

[10] 1 a.u. $= \alpha c$. A typical velocity of a Coulomb exploded fragment would be ~ 0.01 a.u. (compare Fig. 5.16).

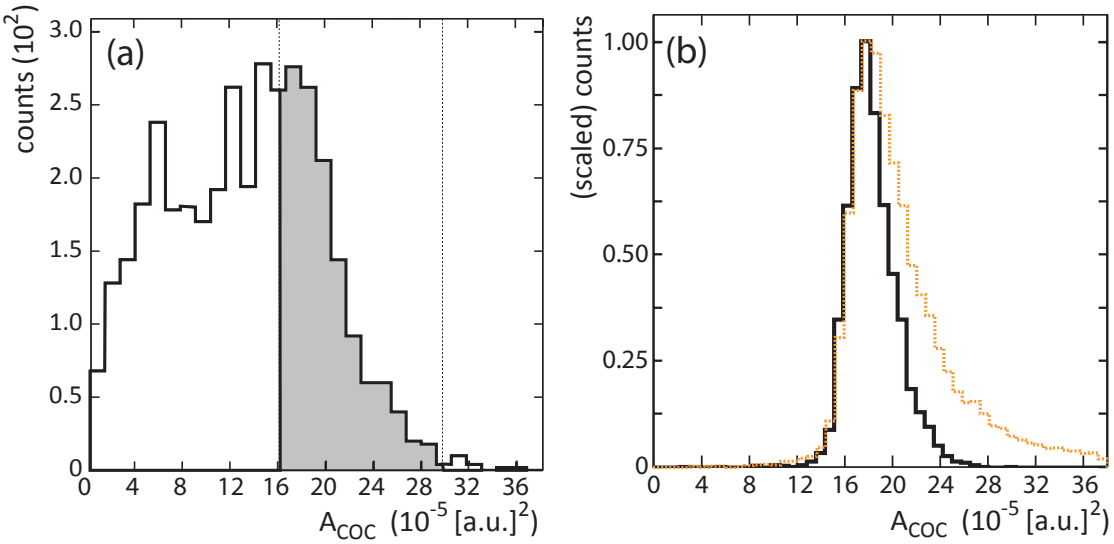

Figure 5.13: Area of the C-O-C triangle in velocity space. (a) Area distribution of the measured triangle. (b) Simulated area distribution before (full line) and after (dashed line) the ion identification cut. The peaks of both distributions are scaled to 1 to allow for a better comparison. Due to the ion identification windows the probability to detected events with triangle areas larger than 16×10^{-5} (a.u.)^2 drops significantly until at 28×10^{-5} (a.u.)^2 the probability is close to zero. Therefore, the high area flank of the simulated distribution after the ion identification cut is shaped by the windows and agrees with the measured distribution. The deviation between simulated and measured distribution for areas smaller than 16×10^{-5} (a.u.)^2 is caused by strong molecular vibrations. To suppress the vibrations only areas within the dashed window are accepted.

since they correspond to an initial molecular structure, before the Coulomb explosion, that is particular large, apparently corresponding to oxirane with its atoms strongly elongated from the equilibrium positions. There are several possibilities which can cause these observations:

- Systematic effects of the FCEI process (see Sec. 2.2) may influence the trajectories of the individual fragments.
- A bias might be introduced by misidentifying the fragments and thus falsely interpreting the effect of the magnetic field.
- Strong molecular vibrations may lead to a deformation of the initial molecular structure.

To investigate the explanations, we compared Monte-Carlo simulations of the Coulomb explosion process to our measurements. The simulations are already discussed in Sec. 5.2.3. They take charge exchange and multiple scattering inside the foil into account. Systematic effects of the detector and the magnetic separating field are also considered. For the simulation a stick model of the chiral molecule in its equilibrium rest positions was used as an input parameter. Since the fragment species is known in the simulation, all fragments were identified correctly.

The simulated C-O-C triangle after the Coulomb explosion is almost equilateral. The distribution of the simulated A_{COC} is shown in Fig. 5.13(b) before and after the ion identification cut. It is obvious that the ion identification cut suppresses a large number of events since the fragments have to hit the two ion identification windows on the rectangular detectors. But even further, the ion identification cut limits the maximum A_{COC} that can be detected since C-O-C triangles with an area too large do not "fit" the two defined windows. In fact, the acceptance for events with A_{COC} larger than $28 \times 10^{-5}\,(\mathrm{a.u.})^2$ is close to zero. To compare the simulated and the measured distributions, we will use the simulated distribution *after* the ion identification cut.

The simulated A_{COC} after the ion identification cut range between $13 \times 10^{-5}\,(\mathrm{a.u.})^2$ and $24 \times 10^{-5}\,(\mathrm{a.u.})^2$. The distribution peaks at $\sim 18 \times 10^{-5}\,(\mathrm{a.u.})^2$. The simulated distribution is therefore much more defined than the measured one. The high-area flank of the measured distribution agrees roughly with the simulated one, indicating that its shape is strongly influenced by the detector windows.

The simulation already considers multiple scattering and charge exchange processes. Both effects can therefore not be the reason for the small measured A_{COC}. The influence of foil polarization effects on the fragment trajectories, which is not considered in the simulation, is in general smaller than multiple scattering especially since C and O are heavy particles. Although the effects will broaden the simulated distribution, they cannot cause the small measured areas. Effects of incomplete stripping are also not fully considered in the simulation since the repelling potential is assumed to be a point-like Coulomb potential. As discussed in Sec. 2.2.3, the actual potential causes a stronger Coulomb

explosion and the measured A_{COC} should therefore be shifted to larger values compared to the simulated distribution. This effect thus also fails to explain the measurement.

To identify the fragments by their detector positions, they were guided through a magnetic field, which separated them by their charge-to-mass ratio in x-direction. After their identification we reversed the influence of the magnetic field on the fragment trajectories by subtracting $x_0(i)$ from the fragments x-position (see Sec. 5.4.1). In case the fragment identification goes wrong, the corrected x-position is biased since $x_0(i)$ is different for each ion species. This causes a strong deformation of the C-O-C triangle, which then can consequently influences the area of the triangle. In the following section we show a way to calculate the probability for events to be falsely identified. This allowed us to inspect the A_{COC}'s of events that have a high probability to be falsely identified. We found that only a small percentage of these events showed an A_{COC} smaller than $15 \times 10^{-5}\,(\mathrm{a.u.})^2$. False fragment identification does therefore not explain the large observed number of events below this limit.

We are hence left with the third one of the explanations considered above. Strongy vibrational excitation may indeed be expected as the oxirane was ionized in an ion source by a very harsh production process and it was not left time to radiatively relax before the Coulomb explosion was triggered. Therefore, we consider that the reason for the events with small areas of the C-O-C triangle is strong vibrational excitation. In events with strong deformation of the C-O-C triangle, in particular obvious by small areas A_{COC}, it is clearly difficult to assign the correct chiral center to the detected D, which relies on the seize and shape of the C-O-C skeleton (see Sec. 5.2.2). Hence, to suppress events of strongly deformed molecules in the further analysis, only events with A_{COC} between $15 \times 10^{-5}\,(\mathrm{a.u.})^2$ and $30 \times 10^{-5}\,(\mathrm{a.u.})^2$ were accepted.

5.4.3 Investigation of residual wrong identifications

Next we investigated the impact of false ion identification on our measurement. For this, we calculated the probability of each event to be assigned correctly. This allowed us

to subtract purposely generated background events from the measured data to get an impression of their contribution to our measurement.

Three fragments hit the rectangular detector at positions x_1, x_2, and x_3. One of these fragments is the doubly charged O and the other two are C's that are either singly or doubly charged. A fragment on the rectangular detector with given x_i-position is an oxygen ion with the probability

$$\widetilde{P}_{O^{2+}}(x_i) = \frac{P_{O^{2+}}(x_i)}{P_{O^{2+}}(x_1) + P_{O^{2+}}(x_2) + P_{O^{2+}}(x_3)} \,. \tag{5.16}$$

Once the oxygen is assigned, the remaining two fragments have to be carbon ions that are either singly- or doubly-charged with the probabilities

$$\widetilde{P}_{C^{+}}(x) = \frac{P_{C^{+}}(x)}{P_{C^{+}}(x) + P_{C^{2+}}(x)} \tag{5.17}$$

or

$$\widetilde{P}_{C^{2+}}(x) = \frac{P_{C^{2+}}(x)}{P_{C^{+}}(x) + P_{C^{2+}}(x)} \,, \tag{5.18}$$

respectively. As illustrated in Fig. 5.14, twelve different permutations i of the ion species are possible and their probabilities to reflect reality are given by

$$\begin{aligned}
P'_1 &= \widetilde{P}_{O^{2+}}(x_1)\, \widetilde{P}_{C^{+}}(x_2)\, \widetilde{P}_{C^{+}}(x_3) \,, \\
P'_2 &= \widetilde{P}_{O^{2+}}(x_1)\, \widetilde{P}_{C^{+}}(x_2)\, \widetilde{P}_{C^{2+}}(x_3) \,, \\
P'_3 &= \widetilde{P}_{O^{2+}}(x_1)\, \widetilde{P}_{C^{2+}}(x_2)\, \widetilde{P}_{C^{1+}}(x_3) \,, \\
P'_4 &= \widetilde{P}_{O^{2+}}(x_1)\, \widetilde{P}_{C^{2+}}(x_2)\, \widetilde{P}_{C^{2+}}(x_3) \,, \\
P'_5 &= \widetilde{P}_{C^{1+}}(x_1) \widehat{P}_{O^{2+}}(x_2)\, \widetilde{P}_{C^{1+}}(x_3) \,, \\
\vdots &= \quad \vdots \qquad \vdots \qquad \vdots \\
P'_{12} &= \widetilde{P}_{C^{2+}}(x_1)\, \widetilde{P}_{C^{2+}}(x_2) \widetilde{P}_{O^{2+}}(x_3) \,.
\end{aligned}$$

By accepting only events with one hit in the O^{2+}-window (position x_1) and two hits in the C^{2+}-window (positions x_2,x_3) on the rectangular detector, we chose one specific

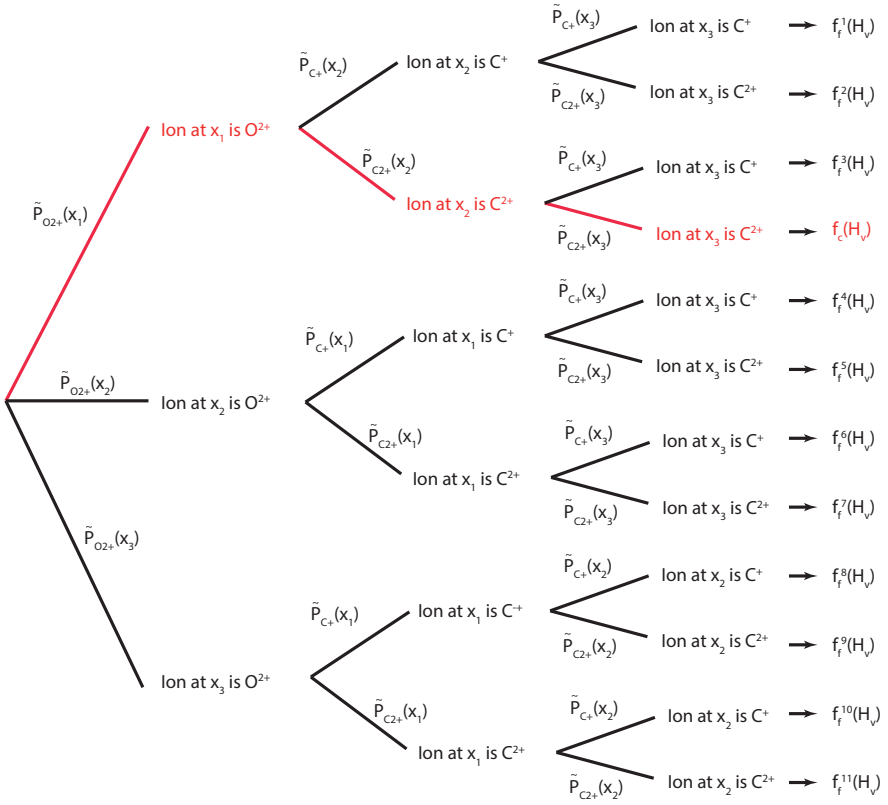

Figure 5.14: Probability tree for three body events on the rectangular detector. The ions were identified via the ion identification windows. Events with one fragment in the O^{2+}- and two fragments in the C^{2+}-window on the rectangular detector were accepted. The fragment position in the O^{2+}-window is x_1 and the fragment positions in the C^{2+}-window are x_2 and x_3. The probability for the ion identification to reflect reality is $P_4' = \widetilde{P}_{O^{2+}}(x_1)\,\widetilde{P}_{C^{2+}}(x_2)\,\widetilde{P}_{C^{2+}}(x_3)$ (red branch). In total twelve different permutations to identify the ions are possible. The permutation with correctly identified events is related to the distribution $f_c(H_v)$. The permutations with falsely identified events are related to the distributions $f_f^n(H_v)$.

permutation (see red branch in Fig. 5.14). As a result of our considerations, we find that on the average the fraction of $c_c = 72\%$ of the events is identified correctly and $c_f = 28\%$ of the events are identified falsely.

We generated background samples from the measured events (using both measurements for a racemic and an enantiopure sample) by purposely mis-identifying the fragments. For generating the samples we re-defined the ion identification windows: The new "O^{2+}-window" covered detector positions $x = (-36 \ldots -6)$ mm and the "C^{2+}-window" covered

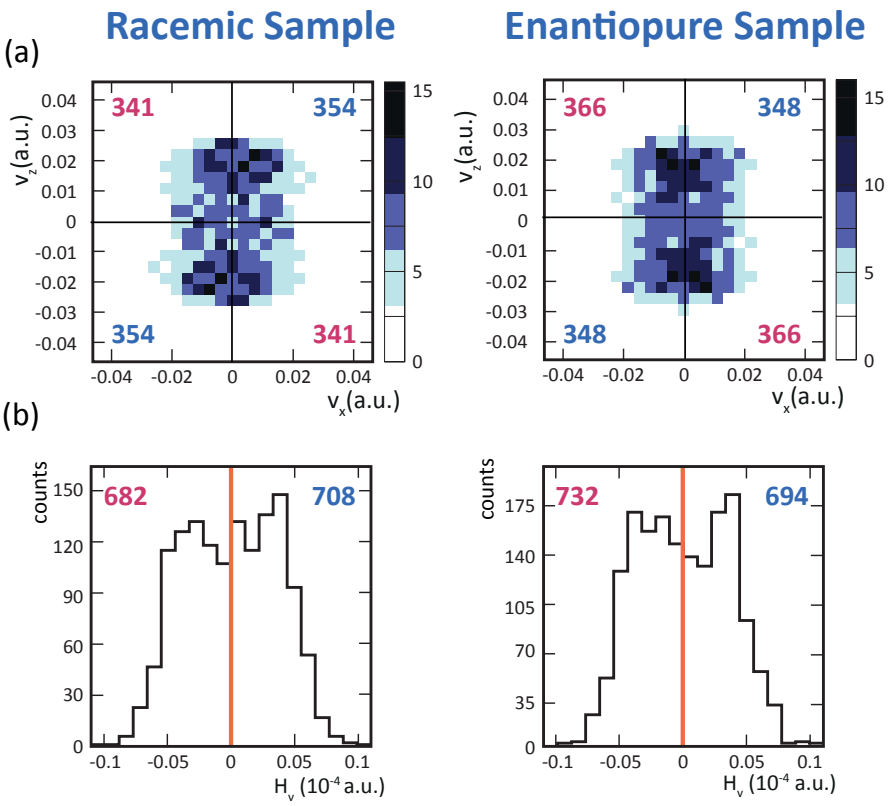

Figure 5.15: Generated background events for the two measured samples were measured. (a) Density plots of the D's projected in the v_x-v_z-plane. (b) Shown are the H_v distributions. The numbers represent the number of D's in the quadrants.

detector positions $x = (12 \ldots 45)$ mm. This time we accepted events with two hits in the "O^{2+}-window", which we arbitrarily identified as O^{2+} and C^{2+}, and one hit in the "C^{2+}-window", which we identified as C^{2+}. In the fraction $c_B^f = 75\%$ of the events, the fragments were identified falsely and consequently $c_B^c = 25\%$ of the events were identified correctly.

Using the background samples, we generated density plots of the D's projected in the v_x-v_z-plane and related H_v-distributions (see Fig. 5.15). To do so, we analyzed the background samples in the same manner as the original sample. For both investigated samples the generated background events look similar, with a flat H_v distribution, and show no asymmetry as expected by the molecular chirality. The numbers of D's in each quadrant agree within their uncertainty. We can hence consider to subtract these background distributions, after suitable scaling, from the original samples without enhancing the signal

of only one configuration and biasing our result.

The H_v-distributions of the original sample and the background sample are given by

$$F_{\mathrm{O}}(H_v) \;=\; N_{\mathrm{O}}(c_{\mathrm{c}}^{\mathrm{O}} f_{\mathrm{c}}^{\mathrm{O}}(H_v) + c_{\mathrm{f}}^{\mathrm{O}} f_{\mathrm{f}}^{\mathrm{O}}(H_v)) \tag{5.19}$$

and

$$F_{\mathrm{B}}(H_v) \;=\; N_{\mathrm{B}}(c_{\mathrm{c}}^{\mathrm{B}} f_{\mathrm{c}}^{\mathrm{B}}(H_v) + c_{\mathrm{f}}^{\mathrm{B}} f_{\mathrm{f}}^{\mathrm{B}}(H_v))\,, \tag{5.20}$$

respectively. Here, N_{O} and N_{B} are the number of events in the original and in the background sample. $f_{\mathrm{c}}^{\mathrm{O}}(H_v)$ and $f_{\mathrm{c}}^{\mathrm{B}}(H_v)$ are the normalized distributions of the corresponding sample for correctly identified events, while $f_{\mathrm{f}}^{\mathrm{O}}(H_v)$ and $f_{\mathrm{f}}^{\mathrm{B}}(H_v)$ are the normalized distributions for falsely identified events.

In total eleven permutations $f_{\mathrm{f}}^{i,n}(H_v)$ (see Fig. 5.14) contribute to the falsely identified events for each sample i and therefore

$$f_{\mathrm{f}}^{i}(H_v) \;=\; \sum_{n=1}^{11} a_{i,n} f_{\mathrm{f}}^{i,n}(H_v)\,. \tag{5.21}$$

Here, $a_{i,n}$ is the contribution of each permutation to the background. It has to be mentioned that the contribution of the different $f_{\mathrm{f}}^{i,n}(H_v)$ to the background sample is not the same as to the original sample and thus $a_{\mathrm{O},n} \neq a_{\mathrm{B},n}$ for most likely all n. But if we assume that the background functions $f_{\mathrm{f}}^{i,n}(H_v)$ are the same, the relation $f_{\mathrm{f}}^{\mathrm{B}}(H_v) = f_{\mathrm{f}}^{\mathrm{O}}(H_v)$ still holds and we can define a new H_v distribution containing only correctly identified events given by

$$\begin{aligned}
F_{\mathrm{C}}(H_v) \;&\equiv\; N_{\mathrm{O}} c_{\mathrm{c}}^{\mathrm{O}} f_{\mathrm{c}}^{\mathrm{O}}(H_v) && (5.22)\\
&=\; F_{\mathrm{O}}(H_v) - N_{\mathrm{O}} \left[\frac{c_{\mathrm{f}}^{\mathrm{O}}}{c_{\mathrm{f}}^{\mathrm{B}}} \frac{F_{\mathrm{B}}(H_v)}{N_{\mathrm{B}}} - \frac{c_{\mathrm{f}}^{\mathrm{O}} c_{\mathrm{c}}^{\mathrm{B}}}{c_{\mathrm{f}}^{\mathrm{B}}} f_{\mathrm{c}}^{\mathrm{B}}(H_v) \right] && (5.23)\\
&\approx\; F_{\mathrm{O}}(H_v) - \underbrace{\frac{c_{\mathrm{f}}^{\mathrm{O}}}{c_{\mathrm{f}}^{\mathrm{B}}} \frac{N_{\mathrm{O}}}{N_{\mathrm{B}}}}_{\equiv s} F_{\mathrm{B}}(H_v)\,. && (5.24)
\end{aligned}$$

To clean our original sample of background events, we can therefore scale the background plots with s (defined in Eqn. 5.24) and then subtract them from the original plots. By this we also subtract $\frac{c_{\mathrm{f}}^{\mathrm{O}} c_{\mathrm{c}}^{\mathrm{B}}}{c_{\mathrm{f}}^{\mathrm{B}}} = 9\%$ of events with correct fragment identification.

5.5 Experimental results and discussion

In the experiment, we analyzed the enantiopure sample blindly, not knowing which enantiomer it contained. The goal of the measurement was to determine the absolute configuration of the chiral oxirane in the enantiopure sample.

The results of the measurements are shown in two representations. In the first representation, each event is plotted in a coordinate system in which both C^{2+} lie on the v_x-axis and the center-of-mass of the C-O-C triangle lies on the positive v_y-axis (see Fig. 5.5). The D's , projected in the v_x-v_z-plane, assign the configuration to the chiral center by the quadrant they lie in. Hence, D's in quadrant II and IV assign the (S)-configuration and D's in quadrant I and III assign the (R)-configuration.

The second representation is given by the H_v-distributions. H_v is defined in Eqn. 5.3. Positive and negative H_v-values assign the (R)- and (S)-configuration to the detected chiral center, respectively. To get a statistical handle on our results and to identify the enantiomer, we defined h_v as a measure of the absolute configuration of the detected chiral center (see Eqn. 5.4). Its expectation value calculates as

$$\langle h_v \rangle \;=\; \frac{(N_+ - N_-)}{(N_- + N_+)}\,. \tag{5.25}$$

Here, N_+ is the number of events with $h_v = +1$ ($H_v > 0$) and N_- is the number of events with $h_v = -1$ ($H_v < 0$). N_+ and N_- are given by the blue and red numbers in both representations, respectively. A negative sign of $\langle h_v \rangle$ identifies the (S,S)- and a positive sign the (R,R)-enantiomer.

As discussed in Sec. 5.2.3, we performed Monte-Carlo simulations, which showed that due to multiple scattering and charge exchange processes in the foil 12% of the exploded

molecules are assigned the wrong handedness and therefore the expectation value for an 100% enantiopure sample is $\langle h_v \rangle = \pm 0.75$. Additional effects, not considered in the simulation, like incomplete fragment stripping, foil polarization effects and especially molecular vibration will smear out the signal further. The expectation value $\langle h_v \rangle$ of the measured enantiopure sample will therefore be smaller than ± 0.75. We still expect $\langle h_v \rangle = \pm 0$ for the racemic sample.

To determine the statistical significance of our measurements Poisson statistics is assumed. The 1σ uncertainty for the count rates is given by

$$\delta N_+ \;=\; \sqrt{N_+} \tag{5.26}$$

and

$$\delta N_- \;=\; \sqrt{N_-}. \tag{5.27}$$

The statistical uncertainty of $\langle h_v \rangle$ is thus given by

$$\delta\langle h_v \rangle \;=\; \sqrt{\left[\frac{2\,N_-\,\delta N_+}{(N_- + N_+)^2}\right]^2 + \left[\frac{2\,N_+\,\delta N_-}{(N_- + N_+)^2}\right]^2} \tag{5.28}$$

and we define the statistical significance of our result by

$$\sigma \;=\; \frac{\langle h_v \rangle}{\delta\langle h_v \rangle}\,. \tag{5.29}$$

In Fig. 5.16 all events satisfying only the ion identification criterium are shown. For the racemic sample these are 1844 events. In 953 events the (S)-configuration and in 891 the (R)-configuration is assigned to the detected chiral center. Of the enantiopure sample 1643 events were accepted. Here, 744 identify the (S)-configuration and 899 the (R)-configuration. A trend towards the (R,R)-enantiomer is visible ($\langle h_v \rangle = 0.094 \pm 0.025$). Since, H_v is proportional to the area of the C-O-C triangle (see Eqn. 5.3) and the area distribution extends to very small values, due to molecular vibration (see Fig. 5.13), the H_v-

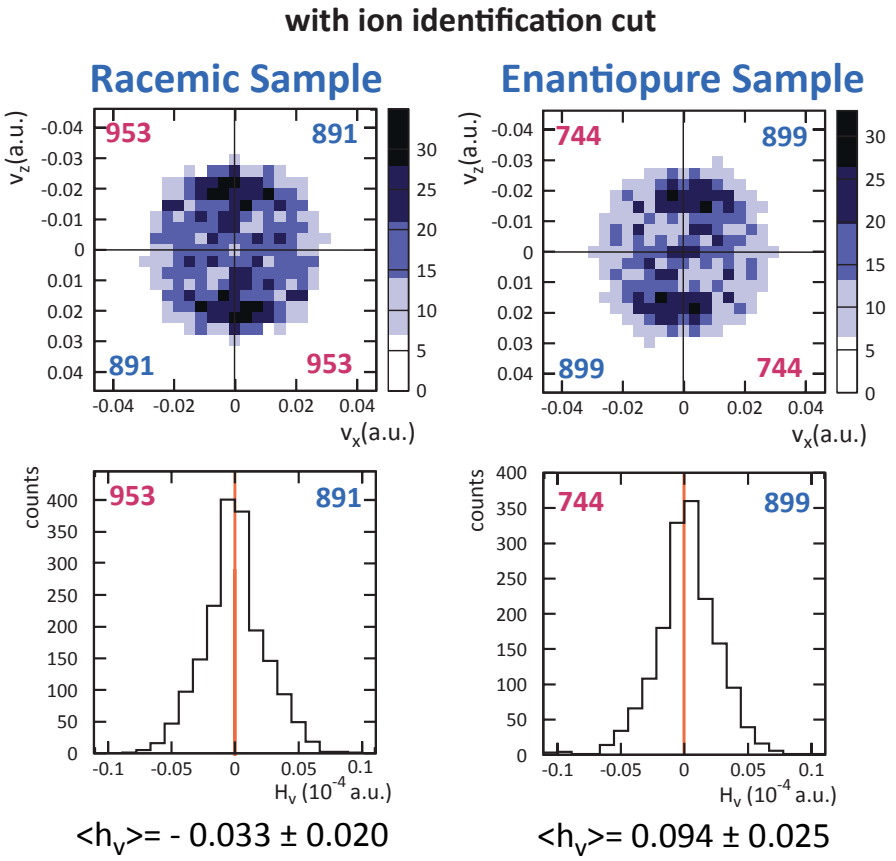

Figure 5.16: Results of absolute configuration measurements after the ion identification cut. The left and right plots show the results for the racemic and enantiopure sample, respectively. The number of D's in each quadrant is given. Upper panels: All events are plotted in the coordinate system defined in Fig. 5.5. The density plots show the D-positions of all four body events. The plots are C_2-symmetric due to the exchange symmetrization of the D's. Already at this point the pattern hints that the enantiopure sample is of the (R, R)-enantiomer. Lower panels: H_v-distribution of four-body events. The statistical significance that the enantiopure sample is of the (R, R)-enantiomer is 3.8σ.

distributions centers at small absolute values. The expectation value $\langle h_v \rangle = -0.033 \pm 0.020$ for the racemic sample and $\langle h_v \rangle = 0.094 \pm 0.025$ for the enantiopure sample. Already at this point, the enantiopure sample is identified as the (R, R)-enantiomer with a statistical significance of 3.8σ. However, compared to the simulations (Fig. 5.6) the event distributions in the v_x v_z plane are considerably broadened. Near $|v_z| = 0.02$ many events are found with both signs in v_x even in the enantiopure case. We interpret this by the additional systematic effects and molecular vibrations that are both neglected in the simulation.

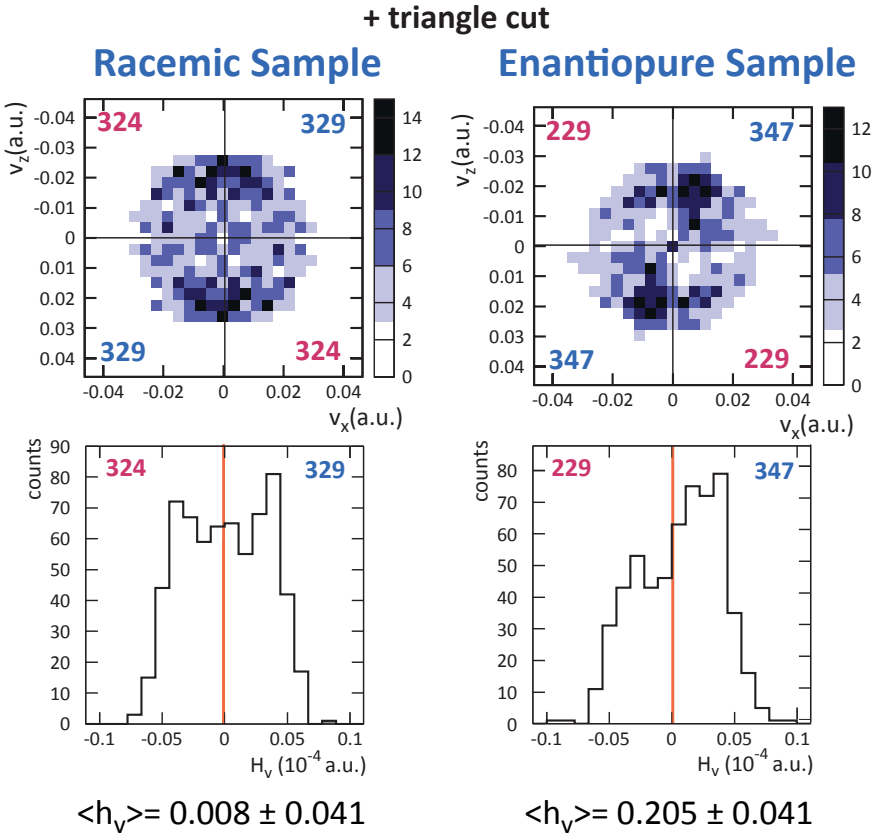

Figure 5.17: Results of absolute configuration measurements after the ion identification cut and the triangle cut. Upper panels: After the triangle cut the pattern of the density plot is much clearer and identifies the enantiopure sample to be of the (R, R) configuration. Lower panels: The H_v distribution now shows a clear signal towards the (R, R)-enantiomer, with the statistical significance being 5.0σ.

To suppress background events, mainly caused by strong vibrations of the molecule, we have developed the cut concerning the area of the C-O-C triangle A_{COC} as described in Sec. 5.4.2. We accepted only events with a value of A_{COC} between $15 \times 10^{-5}\,(\mathrm{a.u.})^2$ and $30 \times 10^{-5}\,(\mathrm{a.u.})^2$. For these events the measured areas agree with simulated areas of non vibrating chiral oxirane. The events remaining after this cut are presented in Fig. 5.17. Here, the (S)- and the (R)-configurations are assigned to 324 and 329 events, respectively for the racemic sample, while for the enantiopure sample 229 and 347 events identify the (S)- and the (R)-configurations, respectively.

The expectation value of the chirality parameter after the C-O-C triangle cut amounts

to $\langle h_v \rangle = 0.008 \pm 0.041$ for the racemic sample. As expected this agrees with zero within its uncertainty. For the enantiopure sample we find $\langle h_v \rangle = 0.205 \pm 0.041$, which identifies the (R, R) enantiomer with a statistical significance of now 5.0σ.

The fragment identification via the C^{2+}- and O^{2+}-windows can go wrong since the ion distributions overlap each other significantly. Hence, e.g., an O^{2+} can be identified as an C^{2+} and vice versa. The triangle cut already suppresses a small amount of these events. To get an idea of the impact of the remaining falsely identified events on our signal, we calculated the number of mis-identified events, generated the same number of background events and subtracted them from our data (for details see Sec. 5.4.3). The results of our measurements after the additional subtraction of the background are shown in Fig. 5.18. The racemic and the enantiopure sample in total now contain 411 events and 362 events, respectively.

After the subtraction, the number of D's in each quadrant i is given by

$$N_{i,\mathrm{C}} = N_{i,\mathrm{O}} - s \cdot N_{i,\mathrm{B}}. \tag{5.30}$$

Here, $N_{i,\mathrm{O}}$ and $N_{i,\mathrm{B}}$ are the number of D's in the original and in the background sample of quadrant i, respectively. The expectation value

$$\langle h_v \rangle_{\mathrm{C}} = \frac{(N_{+,\mathrm{C}} - N_{-,\mathrm{C}})}{(N_{-,\mathrm{C}} + N_{+,\mathrm{C}})} \tag{5.31}$$

and the uncertainty

$$\delta\langle h_v \rangle_{\mathrm{C}} = \frac{2}{(N_{-,\mathrm{C}} + N_{+,\mathrm{C}})^2} \sqrt{N_{+,\mathrm{C}}^2 \delta^2(N_{-,\mathrm{C}}) + N_{-,\mathrm{C}}^2 \delta^2(N_{+,\mathrm{C}})} \tag{5.32}$$

with

$$\delta^2(N_{-,\mathrm{C}}) = (N_{-,\mathrm{O}} + s^2 N_{-,\mathrm{B}}) \tag{5.33}$$

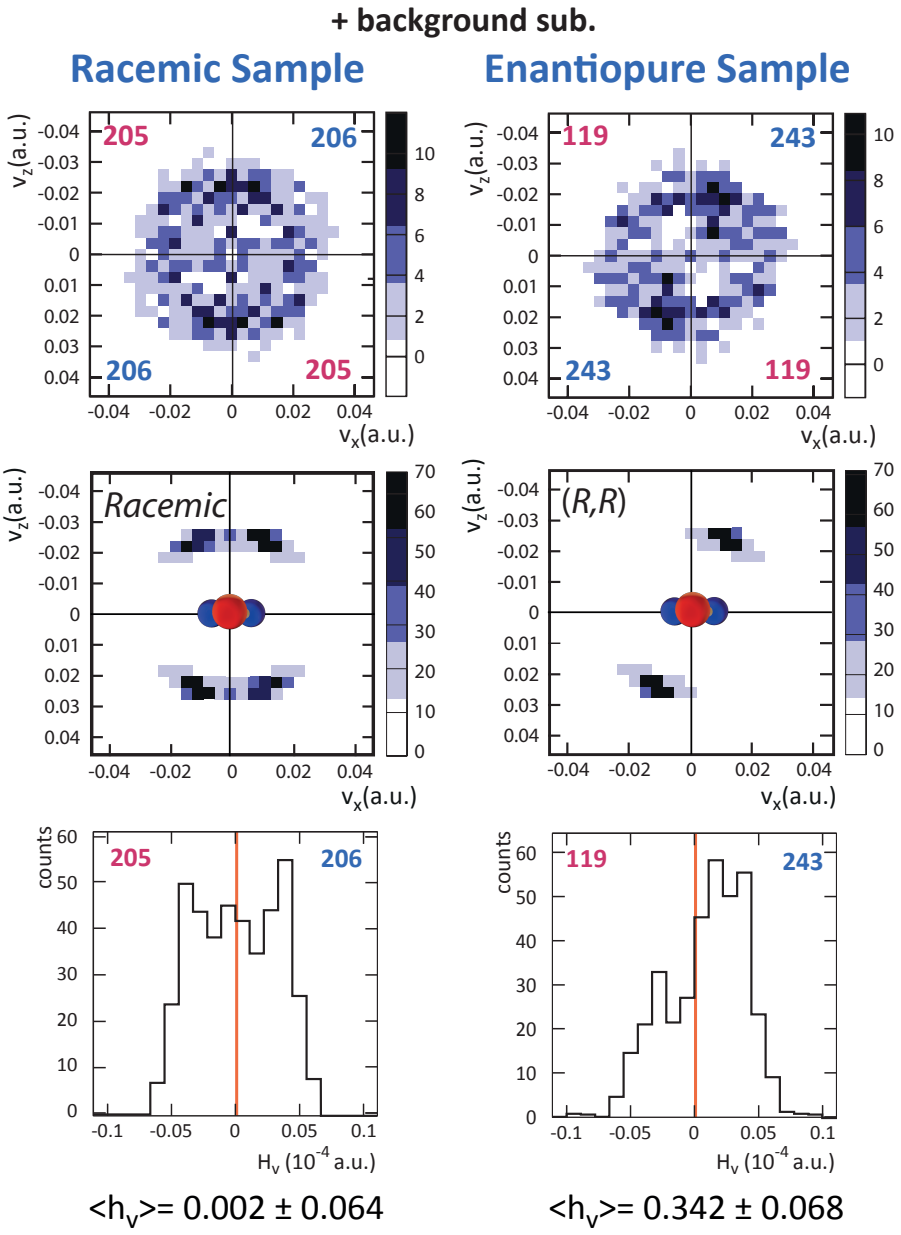

Figure 5.18: Background subtracted plots. Upper panels: The pattern of the density plot of the enantiopure sample identifies the (R, R)-configuration. Middle panels: The simulated density plots of Fig. 5.6 are depicted again to allow an easy comparison with the measurements. The configuration of the simulated oxirane is given. The patter that the measured enantiopure sample shows is similar to the pattern of the simulated plot of (R, R)-oxirane. The pattern of the measured racemic sample is similar to a superposition of both simulated configurations. Lower panels: The contrast of the H_v-distribution improved strongly. The statistical significance of the signal related to the (R, R)-configuration improved to 5.1σ.

and

$$\delta^2(N_{+,\mathrm{C}}) \;=\; (N_{+,\mathrm{O}} + s^2 N_{+,\mathrm{B}})\,. \tag{5.34}$$

The statistical uncertainty is defined by

$$\sigma \;=\; \frac{\langle h_v\rangle_{\mathrm{C}}}{\delta\langle h_v\rangle_{\mathrm{C}}}. \tag{5.35}$$

After background subtraction $\langle h_v\rangle_{\mathrm{C}} = 0.002 \pm 0.064$ for the racemic sample and $\langle h_v\rangle_{\mathrm{C}} = 0.342 \pm 0.068$ for the enantiopure sample. The skewness of the distribution and with it the contrast is more pronounced. Since $\delta\langle h_v\rangle_{\mathrm{C}}$ is also higher because of the additional uncertainty introduced by the background sample, the statistical confidence increases only slightly to 5.1σ. As already discussed in Sec. 5.4.3, the background subtraction is only valid if we assume that the eleven different background permutation have similar patterns in the density and H_v-plots.

The simulation showed an optimal value of $\langle h_v\rangle = 0.75 \pm 0.03$ for enantiopure (R,R)-2,3-dideuterooxirane (see Se. 5.2.3). For a comparable number of events, the nearly enantiopure sample we performed our measurements with, showed $\langle h_v\rangle_{\mathrm{C}} = 0.342 \pm 0.068$. To our belief, the difference between both values is mainly caused by the strong vibrational excitation of the molecules and in particular the vibrational motion of the D's. Also, we cannot exclude some influence from racemization of the chiral oxirane trans-2,3-dideuterooxirane to cis-2,3-dideuterooxirane during the ionization process in the source.

5.6 Impact of FCEI results on stereochemistry

The FCEI measurements were performed in collaboration with the group of Prof. Oliver Trapp from the University of Heidelberg. To test Fischer's assignment (see Sec. 5.1) they applied our FCEI measurement results and correlated the determined absolute configuration of the (R,R)-2,3-dideuterooxirane to (+)-glyceraldehyde. The details concerning the correlation are given in [23]. The approach to the correlation and the synthesis of the

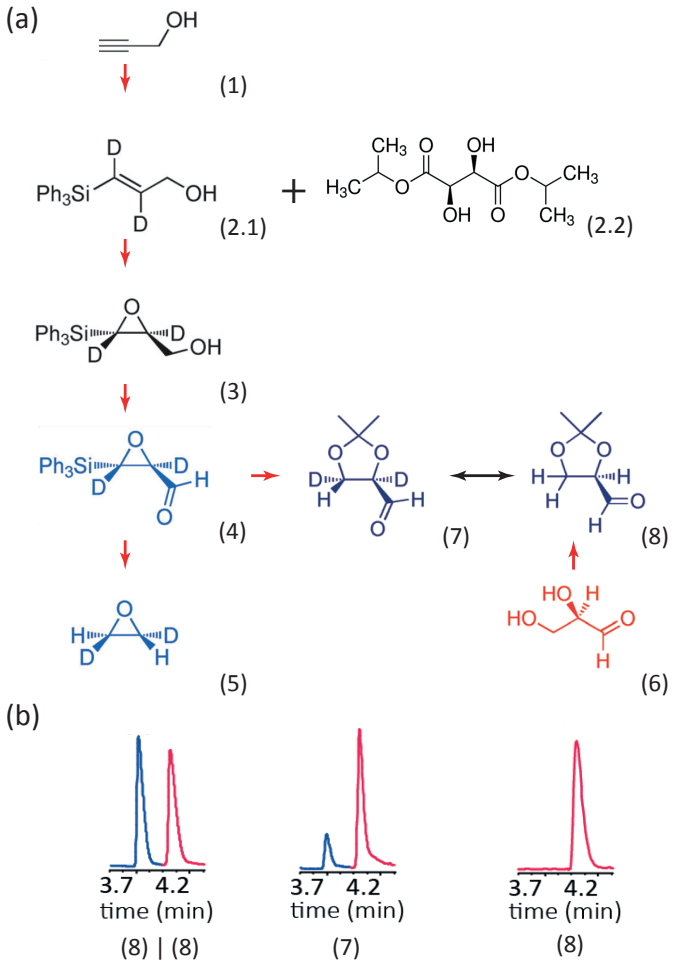

Figure 5.19: Confirmation of Fischer's assignment. The absolute configuration of the chiral oxirane was assigned to be (R, R) via our FCEI measurements. To confirm Fischer's assignment the absolute configuration of the oxirane was linked to (+)-glyceraldehyde. (a) Synthesis of trans-2,3-dideuterooxirane and correlation with (+)-glyceraldehyde. Red arrows indicate chemical correlations and the black arrow a correlation via enantioselective gas chromatography. (b) Results of enantioselective gas chromatography of (left) ketals related to a mixture of (+)- and (−)-glyceraldehyde, (middle) the ketal (7) and (right) the ketal (8). The figure was made of figures of Ref. [23].

oxirane will be briefly discussed here.

The trans-2,3-dideuterooxirane was synthesized from commercially available propargyl alcohol (1) in several steps (see Fig. 5.19(a)). A key step was the one in which the chirality (absolute configuration) was introduced in the molecule. This was performed by

an enantioselective epoxidation of an allyl alcohol (2.1), using (+)-diisopropyl tartrate[11] (2.2) as the carrier of the chiral information, with an enantiomeric purity of 97.5% applying the Sharpless procedure [120]. All further chemical transformations did not affect the stereogenic centers or occurred under known stereoselectivity, so that the chiral information and enantiomeric purity is conserved to the target compound. Epoxyalcohol (3) was then oxidized to an aldehyde (4), which after two more steps yielded the trans-2,3-dideuterooxirane (5). From our FCEI measurements the absolute configuration of the oxirane was determined to be (R, R).

A direct synthesis that correlates the absolute configuration of the oxirane (5) with (+)-glyceraldehyde (6) is not available and therefore a different approach had to be developed. From the determination of the absolute configuration of the oxirane, the absolute configuration of the precursor aldehyde (4) is also known. This molecule was transformed into a ketal (7), representing the same stereochemical information. (+)-glyceraldehyde[12] (6) was synthesized into a deuterated analogue of the same ketal (8).

To correlate the absolute configurations of ketal (7) to ketal (8), enantioselective gas chromatography was performed. In enantioselective gas chromatography, a column containing a chiral substance is used. As the enantiomers of a sample interact differently with this chiral substance, they have different retention times and thus also elute at different times. The deuteration of ketal (7) does not influence this time. The results of the gas chromatography are shown in Fig. 5.19(b). The time resolved spectrum left shows the signals correlated to a racemic mixture of (+)- and (−)-glyceraldehydes, which can obviously be resolved. The plot in the middle shows the signal of ketal (7) that has one major peak (red), eluding at the same time as the peak of the ketal (8), correlated to only the (+)-glyceraldehyde (6) shown in the right plot. This confirms that they have the same absolute configuration, i.e. (+)-glyceraldehyde has the (R)-configuration. This result confirms Fischer's correlation. The small blue peak in the middle plot, representing the (S)-configuration, can be found since the Sharpless epoxidation gives the product in only 97.5% enantiomeric purity and an additional racemization of the sample in the

[11]The molecule is commercially available.
[12](+)-glyceraldehyde with a known sense of the optical activity is commercially available.

synthesis procedure from (4) to (7) occurs.

5.7 Conclusion

We have performed FCEI measurements on trans-2, 3-dideuterooxirane and determined the absolute configuration of a 97.5% enantiopure sample to be the (R, R) configuration with a statistical significance of 5.0σ. The measurement of a racemic sample was used as reference and showed, as expected, no signal that would lead to the identification of one of the enantiomers. For the first time, we determined the absolute configuration of an enantiopure sample of chiral molecules in gas phase without the need of quantum mechanical calculations to predict optical activity or the scattering process in X-ray diffraction.

A mathematical equivalent to the CIP-rule, which relates the handedness of a molecule to its structure, was developed and applied to our FCEI measurements. Our results are therefore connected with the stereochemical standard nomenclature. It is possible to adopt this method to all chiral molecules with central chirality that can be classified via the CIP-rule and apply it in the analysis of other future molecular imaging measurements.

The determined absolute configuration of the (R, R)-enantiomer was chemically linked to the stereochemical standard molecule (+)-glyceraldehyde by Prof. Oliver Trapp and his group. With this correlation it could be shown that (+)-glyceraldehyde has (R)-configuration[13]. As part of the collaboration our FCEI measurements could, therefore, directly confirm Fischer's arbitrary assignment. This result confirms also relation between structure and property of many other chiral molecules that are correlated to (R)-(+)-glyceraldehyde and arranged in the stereochemical network.

[13]The (R)-configuration of glyceraldehyde corresponds to the (L)-configuration in Fischer's denotation

6 Summary and perspective

Foil induced Coulomb Explosion Imaging (FCEI) was used to investigate the structure of two fundamental molecules: The anion D_2^- and the chiral epoxide $C_2OD_2H_2$. D_2^- is a light, diatomic and homonuclear molecule. $C_2OD_2H_2$ is heavy, in fact it is the heaviest molecule FCEI has been performed with at the Max Planck Institute for Nuclear Physics (MPIK) so far, and it consist of seven atoms with different species. These different properties define two different regimes of questions one can answer via FCEI measurements.

In case of the D_2^- anion we were able to compare the bond length distribution to theoretical predictions very accurately. This was possible due to the stripping of all electrons of the fragments, since the light molecule could be accelerated sufficiently. If all electrons are stripped off, the assumption of a point like Coulomb potential, like it is used in the Monte-Carlo simulation that allows for comparing predicted and measured molecule structures, is valid. Over the years, FCEI measurements were established at the MPIK and the experimental setup and analysis procedure was optimized giving a basis for these advanced studies.

In case of $C_2OD_2H_2$ we identified the positions of atoms in the molecule to determine the handedness of an enantiopure sample for the first time via FCEI. The measurements were at the edge of what is actually possible with the current experimental setup and especially motivated by the direct access FCEI gives to the molecular structure. It is conceivable to further establish FCEI as a dedicated tool to determine the handedness of small molecules since it offers several unique advantages.

In FCEI measurements, the ultra-fast electron stripping takes less than 1 fs and produces a net molecular charge state of at least 4. This time scale is considerably faster than

molecular vibrations and rotations and even the position of light atoms such as H and D can be considered as frozen during the stripping process. For the chirality measurements, the ultra-fast stripping time made it possible to chose such an fundamental anorganic molecular epoxide as oxirane for the measurements at all, whose chiral information is imprinted in the positions of the D and the H atoms. Laser induced CEI measurements have recently also been used to investigate the chirality of molecules [6]. In these experiments, the electron stripping was triggered by a strong laser pulses. The stripping time in these type of measurements is dependent on the time length of the laser pulse, which is typically several ten fs long. Therefore, molecular vibrations of light atoms cannot be considered as frozen and any chiral information imprinted in these atoms smears out. In fact, heavy atoms (heavy alkali substituents) were the carrier of the chirality in these species. Still, laser induced CEI measurements have the advantage that they can be applied on neutral molecules and no ionization, as required for FCEI measurements, is needed.

For FCEI measurements the molecule ions are mass selected before the electron stripping by guiding the molecule ions through a magnetic dipole. This allows for a very distinct molecule selection on which the chirality measurements are performed with. This is another unique feature of FCEI measurements. Therefore, even very small traces of chiral molecules in a contaminated sample are possible to access, especially when additionally taking into account the ability of q/A fragment identification after Coulomb explosion of the molecule. Combined with a very efficient stripping probability this allows for chirality measurements on very small samples. E.g. in our measurement, we used less then 100 mg of the enantiopure sample. Considering these advantages in combination with highly accurate mass spectrometry, imaging of subgroups of larger molecules seems possible.

The experimental setup can be optimized in several points for successor chirality measurements. Our measurements showed strong vibrational excitation of the molecule, since the molecular ions were extracted from a "hot" discharge ion source. The vibrations blurred the absolute configuration signal strongly. Softer ion production in a special source would improve the measurements significantly. Another approach to suppress molecular vibration is to store the hot molecular ions for sufficiently long time (several 100 ms) to allow

the relaxation of their vibrational excitation by spontaneous photon emission. For this purpose, the molecules can be either stored in a storage ring or, since very small amounts are sufficient for FCEI measurements due to the efficient stripping process, in an ion trap.

The ion identification was rather complicated and error prone since the fragment species did not fully separate. To achieve a full separation, the molecules have to be accelerated to higher velocities, since this narrows the fragment distributions. In addition, a dedicated chamber design that allows more options in the adjustment of the detector distances will be of advantage in further measurements since this would allow to more freely adjust the q/A fragment separation. Both measures would improve the fragment identification and thus increase the performance of the data analysis.

In this thesis two structure studies on fundamental molecules, which contained light hydrogen and deuterium atoms, via foil-induced Coulomb Explosion Imaging (FCEI) were presented. The D_2^- measurements showed how accurately bond length distributions and therefore the full molecular structure could be resolved under perfect FCEI conditions. Although the limits of FCEI were pushed far away from the ideal, due to the additional mass of the molecule in the chirality measurements, complex questions like the handedness of $C_2OD_2H_2^+$ could be answered. In the discussion above several points were mentioned that would certainly help to optimize the measurements on complex and heavy molecules. These would certainly improve future measurements of the handedness of molecules or other very specific questions on the structure of complex molecules.

A Appendix

A.1 Further predicted lifetimes of the hydrogen anions

Lifetimes of H_2^-, HD^- and D_2^- in the μs-range and longer are shown in Tab. 4.1. Čížek et *al*. calculated further lifetimes that they presented in Fig. 3 and Fig. 4 of Ref. [64] [64]. Some of these lifetimes are shown in Tab. A.1, in Tab. A.2 and in Tab. A.3. The lifetimes of the heavier systems are longer since it is more difficult for the heavy particles to tunnel through the barriers [64].

Table A.1: Predicted lifetimes of H_2^- (given in [64]). If not stated otherwise, the main decay channel is auto-detachment.

τ_{theo} (s)	J	v
$0.3 \cdot 10^{-8}$	27	1 (dissociation)
	...	
$0.6 \cdot 10^{-9}$	26	1 (dissociation)
	...	
$0.1 \cdot 10^{-7}$	25	0
$0.6 \cdot 10^{-8}$	25	1
$0.2 \cdot 10^{-9}$	25	2 (dissociation)
$0.9 \cdot 10^{-9}$	24	0
$0.3 \cdot 10^{-9}$	24	1
$0.1 \cdot 10^{-9}$	24	2
$0.8 \cdot 10^{-10}$	24	3 (dissociation)
	...	

Table A.2: Predicted lifetimes of D_2^- (given in [64]).

τ_{theo} (s)	J	v
	...	
$0.9 \cdot 10^{-7}$	29	0
$0.3 \cdot 10^{-7}$	29	1
$0.2 \cdot 10^{-7}$	29	2
$0.9 \cdot 10^{-8}$	28	0
$0.2 \cdot 10^{-8}$	28	1
$0.9 \cdot 10^{-9}$	28	2
$0.8 \cdot 10^{-9}$	28	3
	...	

Table A.3: Predicted lifetimes of HD^- (given in [64]=.

τ_{theo} (s)	J	v
$1 \cdot 10^{-11}$	38	1 (dissociation)
	...	
$0.7 \cdot 10^{-5}$	36	0
$1 \cdot 10^{-6}$	36	1
$0.8 \cdot 10^{-6}$	36	2
$0.6 \cdot 10^{-6}$	35	0
$0.8 \cdot 10^{-7}$	35	1
$0.3 \cdot 10^{-7}$	35	2
$0.2 \cdot 10^{-7}$	35	3
	...	

A.2 Prediction of kinetic energy release for photofragmentation measurements

As a consequence of the Franck-Condon principle (see discussion in Sec. 3), the kinetic energy release distributions

$$P(E_{\text{kin}})^n_{J,v} dE_{\text{kin}} = \left| \int_0^{\text{inf}} \Psi^*_{J,v}(R) \mu^n_J(R) \Psi^n_J(R, E_{\text{kin}}) dR \right|^2 dE_{\text{kin}} \tag{A.1}$$

within the dipole approximation. Here, $\mu^n_J(R)$ is the electronic transition-matrix element for absorbing a 532 nm photon, n is the final electronic state ($b^3\Sigma^+_u$ or $X^1\Sigma^+_g$), $\Psi_{J,v}(R)$ is the eigenstate of the D^-_2 anion, $\Psi^n_J(R, E_{\text{kin}})$ is the continuum state of the fragmented system, R is the internuclear distance and E_{kin} is the kinetic energy. $\Psi^n_J(R, E_{\text{kin}})$ is the solution of the one-dimensional Schrödinger equation with the potential $V_{J,n}(R) = V_n(R) + V_J(R)$ being the sum of the electronic (n=$X^1\Sigma^+_g$ or $b^3\Sigma^+_u$) and the rotational potential.

To determine $P(E_{\text{kin}})^n_{J,v}$, we calculated $\Psi^n_J(R, E_{\text{kin}})$ numerically via the Numerov method [65, 66]. $\Psi_{J,v}(R)$ is given by calculations of Čížek et *al.* [64]. We used the potential curves given in [121] and we assumed the electronic transition dipole moment $\mu^n_J(R)$ to

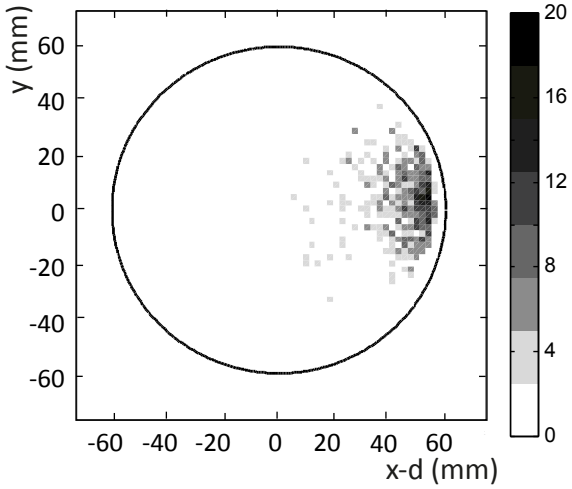

Figure A.1: Mimicked O^3+-distribution. To mimic the O^3+-distribution, the C^{2+}-distribution was copied so its center coincides with the calculated center of the O^3+-distribution. Only events that actually hit the detector were used in the further analysis.

be constant and therefore independent of R, which was also assumed by Lammich et *al.* [5]. The $P(E_{\mathrm{kin}})_{J,v}$ distributions were folded with the energy resolution of the experiment and normalized.

A.3 Contribution of O^{3+}-fragments

The fragment distribution on the rectangular detector, shown in Fig. 5.12, shows contributions of O^{3+}-ions. In this section, we estimate this contribution by investigating the separated C^{2+}-distribution on the round detector, shown in Fig. 5.11, which shows the same contributions of O^{3+} ions since the C^{2+}-distribution was not fully separated from the O^{3+}-distribution and therefore at large x-values O^{3+} ions are observed.

During the measurements, no isolated O^{3+}-distribution was recorded. As a first step, we mimicked the O^{3+}-distribution. Therefore, we re-calibrated Eqn. 5.6, using the C^{2+}-distribution centers at $x_0(C^{2+}) = 328$ mm (see Fig. 5.11(c)), and determined the O^{3+}-distribution to be centered at $x_0(O^{3+}) = 386$ mm. (To isolate the C^{2+}-distribution on the round detector we only increased the magnetic separation field and we did not change the

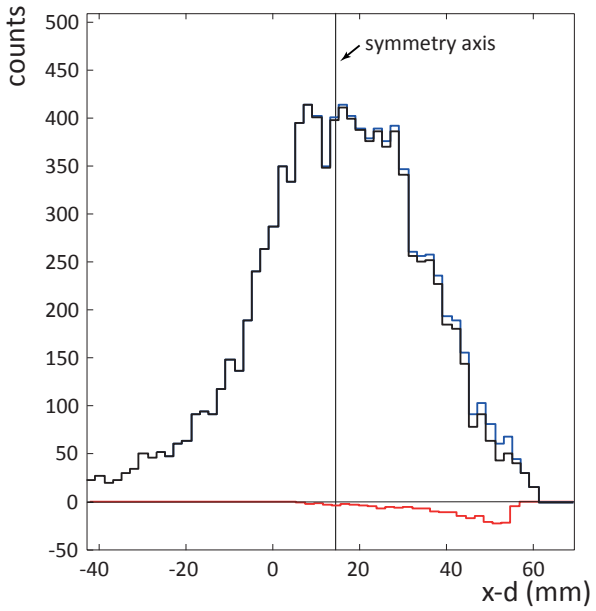

Figure A.2: Symmetric fragment distribution on the round detector projected on the x-axis. The C^{2+}-distribution was projected on the x-axis (blue). The right flank of the C^{2+}-distribution shows contributions of O^{3+} ions. To determine the relative contribution of the O^{3+}-distribution to the C^{2+}-distribution, a fit was performed that scaled and subtracted the O^{3+}-distribution of the C^{2+}-distribution so that both flanks of the calculated distribution (black) are symmetric. We determined a relative intensity of 11% of the O^{3+}-distribution to the C^{2+}-distribution.

chamber adjustment.) Next, we copied the C^{2+}-distribution and centered it at the calculated O^{3+}-distribution center. In the following, we treat the copied C^{2+}-distribution as O^{3+}-distribution. This is a reasonable assumption since the distributions of all recorded charge states agree very well (compare Fig. 5.11). The detector geometry was considered for the O^{3+}-distribution by accepting only events that actually hit the detector (see Fig A.1).

To determine the O^{3+} contribution, both distributions were projected on the x-axis (see Fig. A.2). Due to the contributions of O^{3+}-ions, the right flank of the projected C^{2+}-distribution is deformed when compared to the left flank, which has a negligible contributions of O^{3+} ions. We performed a fit that scales and subtracts the O^{3+}-distribution of the C^{2+}-distribution and converges as soon as the right flank and the left flank of the subtracted distribution agree best, as it is expected of a distribution solely given by C^{2+}

ions. We therefore minimized

$$\chi^2 = \sum_{i=0}^{22} \left[\left(C^{2+}(328+2i) - s_{O^{3+}} O^{3+}(328+2i) \right) \ ... \right. \\ \left. ... - \left(C^{2+}(328-2i) - s_{O^{3+}} O^{3+}(328-2i) \right) \right]^2 , \tag{A.2}$$

with $C^{2+}(x)$ and $O^{3+}(x)$ being the number of events of the corresponding C^{2+}- and O^{3+}-distribution at position x and $s_{O^{3}+}$ being the fitting parameter. Each bin was 2 mm broad in x.

The result of the fit is shown in Fig. A.2. The fit converged for a relative intensity of $s_{O^{3}+} = 11\%$ of the O^{3+}-distribution to the C^{2+}-distribution. Due to the low statistics, we consider this value as an upper limit. The upper limit of 12% given in [22] was determined using an alternative method.

B Lists

B.1 List of Figures

B.2 List of Tables

C References

[1] W. Demtröder. *Laser Spectroscopy: Vol. 1: Basic Principles.* Springer, 2008.

[2] T. Graber, E. P. Kanter, Z. Vager, and D. Zajfman. CH_2^+ is bent. *J. Chem. Phys.*, 98:7725, 1993.

[3] J. M. Cowley. *Diffraction Physics.* Elsevier Science, 1995.

[4] H. Fang, L. C. Giancarlo, and G. W. Flynn. Direct Determination of the Chirality of Organic Molecules by Scanning Tunneling Microscopy. *J. Phys. Chem. B*, 102:731, 1998.

[5] L. Lammich, L. H. Andersen, G. Aravind, and H. B. Pedersen. Experimental characterization of the metastable D_2^- ion by photofragment imaging. *Phys. Rev. A*, 80:023413, 2009.

[6] M. Pitzer, M. Kunitski, A. S. Johnson, T. Jahnke, H. Sann, F. Sturm, L. Schmidt, H. Schmidt-Böcking, R. Dörner, J. Stohner, J. Kiedrowski, M. Reggelin, S. Marquardt, A. Schiesser, R. Berger, and M. Schöffler. Direct Determination of Absolute Molecular Stereochemistry in Gas Phase by Coulomb Explosion Imaging. *Science*, 341:1096, 2013.

[7] T. Kitamura, T. Nishide, H. Shiromaru, Y. Achiba, and N. Kobayashi. Direct observation of "dynamic" chirality by Coulomb explosion imaging. *J. Chem. Phys.*, 115:5, 2001.

[8] Z. Vager, R. Naaman, and E. P. Kanter. Coulomb explosion imaging of small molecules. *Science*, 244:426, 1989.

[9] F. Légaré, K. F. Lee, I. V. Litvinyuk, P. W. Dooley, S. S. Wesolowski, P. R. Bunker, P. Dombi, F. Krausz, A. D. Bandrauk, D. M. Villeneuve, and P. B. Corkum. Laser Coulomb-explosion imaging of small molecules. *Phys. Rev. A*, 71:013415, 2005.

[10] A. Hishikawa, A. Iwamae, and K. Yamanouchi. Ultrafast Deformation of the Geometrical Structure of CO_2 Induced in Intense Laser Fields. *Phys. Rev. Lett.*, 83:1127, 1999.

[11] E. P. Kanter, P. J. Cooney, D. S. Gemmell, K. O. Groeneveld, W. J. Pietsch, A. J. Ratkowski, Z. Vager, and B. J. Zabransky. Role of excited electronic states in the interactions of fast (MeV) molecular ions with solids and gases. *Phys. Rev. A*, 20:834, 1979.

[12] D. Zajfman, G. Both, E. P. Kanter, and Z. Vager. Multiple scattering of MeV atomic and molecular ions traversing ultrathin films. *Phys. Rev. A*, 41:2482, 1990.

[13] D. Zajfman, T. Graber, E. P. Kanter, and Z. Vager. Influence of multiple scattering on the Coulomb-explosion imaging of fast molecules. *Phys. Rev. A*, 46:194, 1992.

[14] P. Herwig, D. Schwalm, M. Čížek, R. Golser, M. Grieser, O. Heber, R. Repnow, A. Wolf, and H. Kreckel. Metastable states of D_2^- observed by foil-induced Coulomb explosion imaging. *Phys. Rev. A*, 87:062513, 2013.

[15] G. Schulz. Resonances in Electron Impact on Diatomic Molecules. *Rev. Mod. Phys.*, 45:423, 1973.

[16] S. Lepp, P. C. Stancil, and A. Dalgarno. Atomic and molecular processes in the early Universe. *J. Phys. B At. Mol. Opt. Phys.*, 35:R57, 2002.

[17] R. Golser, H. Gnaser, W. Kutschera, A. Priller, P. Steier, A. Wallner, M. Čížek, J. Horáček, and W. Domcke. Experimental and theoretical evidence for long-lived molecular hydrogen anions H_2^- and D_2^-. *Phys. Rev. Lett.*, 94:223003, 2005.

[18] B. Jordon-Thaden, H. Kreckel, R. Golser, D. Schwalm, M. H. Berg, H. Buhr, H. Gnaser, M. Grieser, O. Heber, M. Lange, O. Novotný, S. Novotny, H. B. Pedersen, A. Petrignani, R. Repnow, H. Rubinstein, D. Shafir, A. Wolf, and D. Zajfman. Structure and Stability of the Negative Hydrogen Molecular Ion. *Phys. Rev. Lett.*, 107:193003, 2011.

[19] E. Fischer. Einfluss der Configuration auf die Wirkung der Enzyme. *Eur. J. Inorg. Chem.*, 27:2985, 1894.

[20] W. Klyne and J. Buckingham. *Atlas of Stereochemistry—Absolute Configurations of Organic Molecules*. Chapman & Hall, 1978.

[21] P. Herwig, K. Zawatzky, M. Grieser, O. Heber, B. Jordon-Thaden, C. Krantz, O. Novotný, R. Repnow, V. Schurig, D. Schwalm, Z. Vager, A. Wolf, O. Trapp, and H. Kreckel. Imaging the Absolute Configuration of a Chiral Epoxide in the Gas Phase. *Science*, 342:1084, 2013.

[22] P. Herwig, K. Zawatzky, D. Schwalm, M. Grieser, O. Heber, B. Jordon-Thaden, C. Krantz, O. Novotný, Roland Repnow, V. Schurig, Z. Vager, A. Wolf, O. Trapp, and H. Kreckel. Absolute configuration assignment of a chiral molecule in the gas phase using foil-induced coulomb explosion imaging. *Phys. Rev. A*, 90:052503, 2014.

[23] K. Zawatzky, P. Herwig, M. Grieser, O. Heber, B. Jordon-Thaden, C. Krantz, O. Novotný, R. Repnow, V. Schurig, D. Schwalm, Z. Vager, A. Wolf, H. Kreckel, and O. Trapp. Coulomb Explosion Imaged Cryptochiral (R,R)-2,3-Dideuterooxirane: Unambiguous Access to the Absolute Configuration of (+)-Glyceraldehyde. *Chem. Eur. J.*, 20:5555, 2014.

[24] D. S. Gemmel. Collisional effects in the passage of fast molecular ions through thin foils. *Nucl. Instrum. Methods*, 194:255, 1982.

[25] E. P. Kanter. Interaction of Fast MeV Molecular Ions with Matter. *Comm. At. Mol. Phys.*, 11:63, 1981.

[26] I. Plesser. The interpretation of molecular ion dissociation experiments. *Nucl. Instrum. Methods*, 194:269, 1982.

[27] T. Fliessbach. *Mechanik*. Spektrum - Akademischer Verlag, 2003.

[28] R. H. Dalitz. On the analysis of τ-meson data and the nature of the τ-meson. *Philos. Mag.*, 44:1068, 1953.

[29] R. Wester. *Spatial structure of stored molecular ions by Coulomb explosion imaging*. PhD thesis, Ruprecht-Karls-Universität Heidelberg (Max-Planck Institut für Kernphysik), 1999.

[30] H.-D. Betz. Charge States and Charge-Changing Cross Sections of Fast Heavy Ions Penetrating Through Gaseous and Solid Media. *Rev. Mod. Phys.*, 44:465, 1972.

[31] V. S. Nikolaev. Electron capture and loss by fast ions in atomic collisions. *Sov. Phys. Usp.*, 8:269, 1965.

[32] N. Bohr. The penetration of atomic particles through matter. *Det Kgl. Danske Videnskabernes Selskab.*, 18:105, 1948.

[33] Y. Nakai and T. Shirai. Cross sections for charge transfer of hydrogen atoms and ions colliding with gaseous atoms and molecules. *At. Data Nucl. Data Tables*, 37:69, 1987.

[34] P. Sigmund. Scaling laws govering the multiple scattering of diatomic molecules under Coulomb explosion. *Phys. Rev. A*, 46:2596, 1992.

[35] Z. Vager and D. S. Gemmel. Polarization induced in a solid by the passage of fast charged particles. *Phys. Rev. Lett.*, 37:1352, 1976.

[36] P. M. Echenique, F. Flores, and R. H. Ritchie. *Dynamic Screening of Ions in Condensed Matter.* Academic Press, 1990.

[37] L. Knoll. *Dissociation dynamics in Coulomb explosion imaging of diatomic molecules.* PhD thesis, Ruprecht-Karls-Universität Heidelberg (Max-Planck Institut für Kernphysik), 2000.

[38] L. Lammich, H. Buhr, H. Kreckel, S. Krohn, M. Lange, D. Schwalm, R. Wester, A. Wolf, D. Strasser, D. Zajfman, Z. Vager, I. Abril, S. Heredia-Avalos, and R. Garcia-Molina. Coulomb-explosion imaging of CH_2^+: Target-polarization effects and bond-angle distribution. *Phys. Rev. A*, 69:062904, 2004.

[39] H. Shull and G. Hall. Atomic Units. *Nature*, 184:1559, 1959.

[40] R. Wester, U. Hechtfischer, L. Knoll, M. Lange, J. Levin, M. Scheffel, D. Schwalm, A. Wolf, A. Baer, Z. Vager, D. Zajfman, M. Mladenović, and S. Schmatz. Relaxation dynamics of deuterated formyl and isoformyl cations. *J. Chem. Phys.*, 116:7000, 2002.

[41] R. Wester, F. Albrecht, M. Grieser, L. Knoll, R. Repnow, D. Schwalm, A. Wolf, A. Baer, J. Levin, Z. Vager, and D. Zajfman. Coulomb explosion imaging at the heavy ion storage ring TSR. *Nucl. Instr. and Meth. in Phys. Res. A*, 413:379, 1998.

[42] J. Levin, L. Knoll, M. Scheffel, D. Schwalm, R. Wester, A. Wolf, A. Baer, Z. Vager, D. Zajfman, and V.Kh. Liechtenstein. Application of ultrathin diamond-like-carbon targets to coulomb explosion imaging. *Nuclear Instruments and Methods in Physics Research Section B: Beam Interactions with Materials and Atoms*, 168:268, 2000.

[43] D. S. Gemmel, J. Remillieux, J. C. Poizat, M. J. Gaillard, R. E. Holland, and Z. Vager. Evidence for an alignment effect in the motion of swift ion clusters through solids. *Phys. Rev. Lett.*, 34:1420, 1975.

[44] Z. Vager, D. S. Gemmel, and B. J. Zabransky. Dissociation of fast HeH^+ ions traversing thin foils. *Phys. Rev. A.*, 14:638, 1976.

[45] D. Zajfman, Z. Vager, R. Naaman, R. E. Mitchell, E. P. Kanter, T. Graber, and A. Belkacem. The structures of C_2H^+ and $C_2H_2^+$ as measured by Coulomb explosion imaging. *J. Chem. Phys.*, 94:6377, 1991.

[46] L. Knoll. Direkte Abbildung und Berechnung räumlicher Molekül Strukturen. Diplomarbeit, Ruprecht-Karls-Universität Heidelberg (Max-Planck Institut für Kernphysik), 1997.

[47] R. Wester. Erste Untersuchungen zur Coulomb-Explosion molekularer Ionen am Schwerionenspeichering TSR. Diplomarbeit, Ruprecht-Karls-Universität Heidelberg (Max-Planck Institut für Kernphysik), 1997.

[48] Z. Amitay, A. Baer, M. Dahan, J. Levin, Z. Vager, D. Zajfman, L. Knoll, M. Lange, D. Schwalm, R. Wester, A. Wolf, I. F. Schneider, and A. Suzor-Weiner. Dissociative recombination of vibrationally excited HD^+: State-selective experimental investigation. *Phys. Rev. A*, 60:3769, 1999.

[49] H. Kreckel. *Internal Excitations of Stored Triatomic Hydrogen Molecular Ions*. PhD thesis, Ruprecht-Karls-Universität Heidelberg (Max-Planck Institut für Kernphysik), 2003.

[50] H. Kreckel, S. Krohn, L. Lammich, M. Lange, J. Levin, M. Scheffel, D. Schwalm, J. Tennyson, Z. Vager, R. Wester, A. Wolf, and D. Zajfman. Vibrational and rotational cooling of H_3^+. *Phys. Rev. A*, 66:052509, 2002.

[51] D. Strasser, L. Lammich, S. Krohn, M. Lange, H. Kreckel, J. Levin, D. Schwalm, Z. Vager, R. Wester, A. Wolf, and D. Zajfman. Two- and Three-Body Kinematical Correlation in the Dissociative Recombination of H_3^+. *Phys. Rev. Lett.*, 86:779, Jan 2001.

[52] D. Strasser, L. Lammich, H. Kreckel, S. Krohn, M. Lange, A. Naaman, D. Schwalm, A. Wolf, and D. Zajfman. Breakup dynamics and the isotope effect in H_3^+ and D_3^+ dissociative recombination. *Phys. Rev. A*, 66:032719, 2002.

[53] E. Herbst and W. Klemperer. The Formation and Depletion of Molecules in Dense Interstellar Clouds. *Astrophys. J.*, 185:505, 1973.

[54] W. D. Watson. The Rate of Formation of Interstellar Molecules by Ion-Molecule Reactions. *Astrophys. J.*, 183:L17, 1973.

[55] B. J. McCall and T. Oka. H_3^+–an Ion with Many Talents. *Science*, 287:1941, 2000.

[56] R. Wester, U. Hechtfischer, L. Knoll, M. Lange, J. Levin, M. Scheffel, D. Schwalm, A. Wolf, A. Baer, Z. Vager, D. Zajfman, M. Mladenović, and S. Schmatz. Relaxation dynamics of deuterated formyl and isoformyl cations. *J. Chem. Phys.*, 116:7000, 2002.

[57] R. Lucas and H. Liszt. Interstellar isotope ratios from mm-wave molecular absorption spectra. *Astron. Astrophys.*, 337:246, 1998.

[58] E. A. Gislason. Series expansions for Franck Condon factors. *J. Chem. Phys.*, 58:3702, 1973.

[59] C. Boisseau, E. Audouard, J. Vigué, and P. S. Julienne. Reflection approximation in photoassociation spectroscopy. *Phys. Rev. A*, 62:052705, 2000.

[60] G. Herzberg. *The Spectra and Structures of Simple Free Radicals: An Introduction to Molecular Spectroscopy.* Dover Publications, 1971.

[61] W. Demtröder. *Molekülphysik.* Oldenbourg Wissenschaftsverlag GmbH, 2003.

[62] L.D. Landau and E. M. Lifshitz. *Quantum Mechnics - Non-relativistic theory.* Pergamon Press, 1959.

[63] A. Messiah. *Quantenmechanik 1.* de Gruyter, 1991.

[64] M. Čížek, J. Horácek, and W. Domcke. Long-lived anionic states of H_2, HD, D_2, and T_2. *Phys. Rev. A*, 75:012507, 2007.

[65] B. Numerov. A method of extrapolation of pertubations. *Mon. Not. R. Astron. S.*, 84:592, 1924.

[66] B. Numerov. Note on the numerical integration of d2x/dt2 = f(x, t). *Astron. Nach.*, 230(19):359, 1927.

[67] V. I. Khvostenko and V. M. Dukel'Skii. The negative ion H_2^-. *Sov. Phys. JETP*, 7:709, 1958.

[68] R. Hurley. Low-energy duopigatron source with an auxilliary gas feed. *Nucl. Instr. and Meth.*, 118:307, 1974.

[69] W. Aberth, R. Schnitzer, and M. Anbar. Observations of diatomic and triatomic hydrogen negative ions. *Phys. Rev. Lett.*, 34:1600, 1975.

[70] H. Eyring, J. O. Hirschfelder, and H. S. Taylor. The Radiochemical Synthesis and Decomposition of Hydrogen Bromide. *J. Chem. Phys.*, 4:570, 1936.

[71] H. S. Taylor and F. E. Harris. Potential curve for the $^2\Sigma_u^+$ state of H_2^-. *J. Chem. Phys.*, 39:1012, 1963.

[72] J. N. Bardsley, A. Herzenberg, and F. Mandl. Electron resonances of the H_2^- ion. *Proc. Phys. Soc.*, 89:305, 1966.

[73] Y. K. Bae, M. J. Coggiola, and J. R. Peterson. Search for H_2^-, H_3^-, and other metastable negative ions. *Phys. Rev. A*, page 2888, 1984.

[74] H. Gnaser and R. Golser. Verification of long-lived molecular hydrogen anions (H_n^-, D_n^-, $n = 2, 3$) by secondary-ion mass spectrometry. *Phys. Rev. A*, 73:021202, 2006.

[75] M. Čížek, J. Horácek, and W. Domcke. Nuclear dynamics of the H_2^- collision complex beyond the local approximation: associative detachment and dissociative attachment to rotationally and vibrationally excited molecules. *J. Phys. B: At. Mol. Opt. Phys.*, 31:2571, 1998.

[76] H. Kreckel, H. Bruhns, M. Čížek, S. C. O. Glover, K. A. Miller, X. Urbain, and D. W. Savin. Experimental results for H_2 formation from H^- and H and implications for first star formation. *Science*, 329:69, 2010.

[77] K. A. Miller, H. Bruhns, J. Eliášek, M. Čížek, H. Kreckel, X. Urbain, and D. W. Savin. Associative detachment of $H^- + H \rightarrow H_2 + e^-$. *Phys. Rev. A*, 84:052709, 2011.

[78] M. Bacal and G. W. Hamilton. H^- and D^- Production in Plasmas. *Phys. Rev. Lett.*, 42:1538, 1979.

[79] P. Franzen, H. D. Falter, U. Fantz, W. Kraus, M. Berger, S. Christ-Koch, M. Fröschle, R. Gutser, B. Heinemann, S. Hilbert, S. Leyer, C. Martens, P. McNeely, R. Riedl, E. Speth, and D. Wünderlich. Progress of the development of the IPP RF negative ion source for the ITER neutral beam system. *Nucl. Fusion*, 47:264, 2007.

[80] O. Vollmer, B. Heinemann, W. Kraus, P. McNeely, R. Riedl, E. Speth, R. Trainham, and R. Wilhelm. Progress in the development of a large RF negative ion source for fusion. *Fusion Eng. Des.*, 56:465, 2001.

[81] O. Heber, R. Golser, H. Gnaser, D. Berkovits, Y. Toker, M. Eritt, M. L. Rappaport, and D. Zajfman. Lifetimes of the negative molecular hydrogen ions: H_2^-, D_2^-, and HD^-. *Phys. Rev. A*, 73:060501, 2006.

[82] S. V. Khristenko, A. I. Maslov, and V. P. Shevelko. *Molecules and Their Spectroscopic Properties*. Springer, 1998.

[83] W. Demtröder. *Experimentalphysik 3 - Atome, Moleküle und Festkörper*. Springer, 2005.

[84] W. Demtröder. *Experimentalphysik 4 - Kern-, Teilchen- und Astrophysik*. Springer, 2005.

[85] L. D. Barron. Chirality and life. *Space Sci. Rev.*, 135:187, 2008.

[86] M. Quack. How Important is Parity Violation for Molecular and Biomolecular Chirality? *Angew. Chem.*, 41:4618, 2002.

[87] F. Hund. Symmetriecharaktere von Termen bei Systemen mit gleichen Partikeln in der Quantenmechanik. *Zeitschrift für Physik*, 43:788, 1927.

[88] F. Hund. Zur Deutung der Molekülspektren. III. *Z. Phys.*, 43:805, 1927.

[89] T. D. Lee and C. N. Yang. Question of Parity Conservation in Weak Interactions. *Phys. Rev.*, 104:254, 1956.

[90] C. S. Wu, E. Ambler, R. W. Hayward, D. D. Hoppes, and R. P. Hudson. Experimental Test of Parity Conservation in Beta Decay. *Phys. Rev.*, 105:1413, 1957.

[91] Y. Yamagata. A hypothesis for the asymmetric appearance of biomolecules on earth. *J. theor. biol.*, 11:495, 1966.

[92] L. Bergmann, C. Schaefer, and H. Niedrig. *Lehrbuch der Experimentalphysik - Optik*. de Gruyter, 2004.

[93] R. M. Flügel. *Chirality and Life*. Springer, 2011.

[94] L. Pasteur Vallery-Radot. *Oeuvres de Pasteur*. Masson, 1922.

[95] G. L. Geison. *The Private Science of Louis Pasteur*. Princeton University Press, 1996.

[96] J. M. Bijvoet, A. F. Peerdeman, and A. J. van Bommel. Determination of the Absolute Configuration of Optically Active Compounds by Means of X-Rays. *Nature*, 168:271, 1951.

[97] N. Harada. Determination of absolute configurations by X-ray crystallography and ^{1}H NMR anisotropy. *Chirality*, 20:691, 2008.

[98] Jack D. Dunitz. *X-ray analysis and the structure of organic molecules*. Cornell University Press, 1979.

[99] H. D. Flack, G. Bernardinelli, D. A. Clemente, A. Linden, and A. L. Spek. Centrosymmetric and pseudo-centrosymmetric structures refined as non-centrosymmetric. *Acta Crystallogr. Sect. B-Struct. Sci.*, 62:695, 2006.

[100] H. D. Flack and G. Bernardinelli. The use of x-ray crystallography to determine absolute configuration. *Chirality*, 20:681, 2008.

[101] R. W. W. Hooft, L. H. Straver, and A. L. Spek. Determination of absolute structure using Bayesian statistics on Bijvoet differences. *J. Appl. Crystallogr.*, 41:96, 2008.

[102] H. D. Flack, M. Sadki, A. L. Thompson, and D. J. Watkin. Practical applications of averages and differences of Friedel opposites. *Acta Crystallogr. Sect. A*, 67:21, 2011.

[103] S. Parsons, P. Pattison, and H. D. Flack. Analysing Friedel averages and differences. *Acta Crystallogr. Sect. A*, 68:736, 2012.

[104] P. J. Stephens. Theory of vibrational circular dichroism. *J. Phys. Chem.*, 89:748, 1985.

[105] T. B. Freedman, X. Cao, R. K. Dukor, and L. A. Nafie. Absolute configuration determination of chiral molecules in the solution state using vibrational circular dichroism. *Chirality*, 15:743, 2003.

[106] P. J. Stephens, F. J. Devlin, and J. Pan. The determination of the absolute configurations of chiral molecules using vibrational circular dichroism (VCD) spectroscopy. *Chirality*, 20:643, 2008.

[107] L. D. Barron, M. P. Bogaard, and A. D. Buckingham. Raman scattering of circularly polarized light by optically active molecules. *J. Am. Chem. Soc.*, 95:603, 1973.

[108] J. Haesler, I. Schindelholz, and E. Riguet. Absolute configuration of chirally deuterated neopentane. *Nature*, 446:526, 2007.

[109] P. L. Polavarapu. Molecular Structure Determination Using Chiroptical Spectroscopy: Where We May Go Wrong? *Chirality*, 24:909, 2012.

[110] L. Addadi, Z. Berkovitch-Yellin, N. Domb, E. Gati, M. Lahav, and L. Leiserowitz. Resolution of conglomerates by stereoselective habit modifications. *Nature*, 296:12, 1982.

[111] Z. Berkovitch-Yellin, L. Addadi, M. Idelson, L. Leiserowitz, and M. Lahav. Absolute configuration of chiral polar crystals. *Nature*, 296:27, 1982.

[112] G. P. Moss. Basic terminology of stereochemistry (IUPAC Recommendations 1996). *Pure Appl. Chem.*, 68:2193, 1996.

[113] R. S. Cahn, C. Ingold, and V. Prelog. Specification of Molecular Chirality. *Angew. Chem. Int. Ed. Engl.*, 5:385, 1966.

[114] V. Prelog and G. Helmchen. Basic Principles of the CIP-System and Proposals for a Revision. *Angew. Chem. Int. Ed. Engl.*, 21:567, 1982.

[115] H. P. Latscha and A. Klein. *Organische Chemie - Basiswissen II, 4th Ed.* Springer, 1997.

[116] K.-H. Hellwich. *Stereochemie Grundbegriffe.* Springer, 2002.

[117] F. E. Jr. Bailey. *Poly (Ethylene Oxide).* Academic Press, Inc., 1976.

[118] G. C. C. Mendes, T. R. S. Brandão, and C. L. M. Silva. Ethylene oxide sterilization of medical devices: A review. *American Journal of Infection Control*, 35:574, 2007.

[119] M.L. Abell, J.P. Braselton, and J.A. Rafter. *Statistics with Mathematica.* Academic Press, 1999.

[120] Tsutomu Katsuki and K. Barry Sharpless. The first practical method for asymmetric epoxidation. *Journal of the American Chemical Society*, 102:5974, 1980.

[121] W. Kolos and L. Wolniewicz. Potential-energy curves for the $x^1\Sigma_g^+$, $b^3\Sigma_u^+$ and c^1II_u states of the hydrogen molecule. *J. Chem. Phys.*, 43:2429, 1965.

Danksagung

Als erstes möchte ich Prof. Andreas Wolf danken, dass er mir die Möglichkeit gegeben hat am MPIK zu promovieren. Die Arbeit war sehr abwechslungsreich, lehrreich und spannend!

Bei Prof. Andreas Wolf, Dr. Holger Kreckel und Prof. Dirk Schwalm und möchte ich mich für die exzellente Betreuung bedanken bei der keine Frage lange unbeantwortet blieb. Ich habe mich immer sehr unterstützt gefühlt. Die ganzen Messungen und die Analyse wären ohne Sie nicht möglich gewesen.

Für das Korrekturlesen dieser Arbeit bedanke ich mich bei Prof. Andreas Wolf, Dr. Holger Kreckel, Prof. Dirk Schwalm, Kerstin Zawatzki, Dr. Aodh o'Conner und Florian Grussie.

Ein großer Dank geht auch an Prof. Oliver Trapp und Kerstin Zawatzki für das Synthetisieren und Korrelieren des Oxirans, wodurch die Chiralitätsmessungen mit dieser fundamentalen Fragestellung erst ermöglicht wurden.

Dr. Manfred Griesser, Dr. Roland Repnow und allen Technikern möchte ich für das Bereitstellen eines nahezu immer perfekten Ionenstrahls danken.

Dirk Kaiser und Stephen Vogel danke ich für ihre Unterstützung bei meinem langwierigen Zusammenbau der Deflektoren und NEG-Pumpen für den CSR. Noch viele Andere haben mich dabei unterstützt und sind mir zu Hand gegangen. Danke dafür!

Dem Konstruktionsbüro am MPIK danke ich für die unkomplizierte Zusammenarbeit bei der Entwicklung der NEG-Terminals.

Weiterhin danke ich allen Mitgliedern der Gruppe und allen anderen Leuten auf die ich während meiner Areit am MPIK gestoßen bin für die tolle Zeit. Die Arbeitsatmosphäre am MPIK habe ich sehr genossen.

Meiner Frau Meike danke ich für ihre Geduld mit mir, die sie gerade in der Endephase aufbringen musste. Meiner Tochter Paula möchte ich danken, dass sie immer vorzüglich versteht mich auf andere Gedanken zu bringen. Zuletzt danke ich noch meiner Mutter,

die viele Male auf Paula aufgepasst hat und mir damit den Rücken freigehalten hat, und meinem Vater.